



**AIAA 2000-2215**

**High Speed Vortex Flows**

Richard M. Wood, Floyd J. Wilcox, Jr.,  
Steven X. S. Bauer, and Jerry M. Allen  
NASA Langley Research Center  
Hampton, Virginia

**Fluids 2000**

**19-22 June 2000 / Denver, CO**



# HIGH SPEED VORTEX FLOWS

Richard M. Wood\*, Floyd J. Wilcox†,  
Steven X. S. Bauer††, and Jerry M. Allen†††  
NASA Langley Research Center  
Hampton, Virginia

## 1.0 ABSTRACT

A review of the research conducted at the National Aeronautics and Space Administration (NASA), Langley Research Center (LaRC) into high-speed vortex flows during the 1970s, 1980s, and 1990s is presented. The data reviewed is for flat plates, cavities, bodies, missiles, wings, and aircraft. These data are presented and discussed relative to the design of future vehicles. Also presented is a brief historical review of the extensive body of high-speed vortex flow research from the 1940s to the present in order to provide perspective of the NASA LaRC's high-speed research results. Data are presented which show the types of vortex structures which occur at supersonic speeds and the impact of these flow structures to vehicle performance and control is discussed. The data presented shows the presence of both small- and large-scale vortex structures for a variety of vehicles, from missiles to transports. For cavities, the data show very complex multiple vortex structures exist at all combinations of cavity depth to length ratios and Mach number. The data for missiles show the existence of very strong interference effects between body and/or fin vortices and the downstream fins. It was shown that these vortex flow interference effects could be both positive and negative. Data are shown which highlights the effect that leading-edge sweep, leading-edge bluntness, wing thickness, location of maximum thickness, and camber has on the aerodynamics of and flow over delta wings. The observed flow fields for delta wings (i.e. separation bubble, classical vortex, vortex with shock, etc.) are discussed in the context of aircraft design. And data have been shown that

indicate that aerodynamic performance improvements are available by considering vortex flows as a primary design feature. Finally a discussion of a design approach for wings which utilize vortex flows for improved aerodynamic performance at supersonic speeds is presented.

## 2.0 INTRODUCTION

Even after a half of a century of high-speed vortex flow research there still exist a need for a thorough understanding as well as an efficient prediction capability of three-dimensional separated flows (vortex) at high-speed (supersonic and hypersonic). The extensive amount of previous research has contributed greatly to understanding these complex flow structures, however, in order to support the design of future aerospace vehicles, which is the primary aim of aerodynamics, Kucheman 1978<sup>1</sup>, robust understanding and efficient design guidelines and tools must be available.

It is interesting to note that the recent research remains focused on the same three vehicle types as that which guided the previous efforts in the 1960s and 1970s. These vehicles are; supersonic cruise aircraft<sup>2</sup>, missiles<sup>3</sup> and reentry/blunt bodies<sup>3</sup>. In addition to the similarity in vehicle focus, there is also great similarity in the design approach used for each of these vehicle types. In fact many of the present designs are derivatives of the preferred shapes from 1960s and 1970s. Also note, that despite the significant focus by the research community on the vortex flow for these vehicles the design approach has remains focused on maximizing attached flow at all flight conditions. The design philosophy continues to only grudgingly accept separated flows (vortex), with the assumed penalty, at off-design conditions. It is clear from the recent design efforts that we have yet to step out of the design assumptions and constraints of the 1960s in order to explore new design concepts that attempt to exploit vortex flows for improved aerodynamics.

---

\* Aerospace Engineer, Member AIAA

† Aerospace Engineer

†† Aerospace Engineer, Senior Member AIAA

††† Aerospace Engineer, Associate Fellow AIAA

---

Copyright © 1998 by the American Institute of Aeronautics and Astronautics, Inc. No copyright is asserted in the United States under Title 17, U. S. Code. The U. S. Government has a royalty-free license to exercise all rights under the copyright claimed herein for government purposes. All other rights are reserved by the copyright owner.

Research into vortex flows at supersonic speeds began in the 1940s with the initial research effort being directed toward simple bodies and wings<sup>4-29</sup>. This work was in an effort to support the exploration of supersonic flight for rockets, missiles, and aircraft, such as the X-15<sup>30</sup>. In the late 1950s and early 1960s the study of hypersonic reentry vehicles<sup>31</sup> began to contribute to the body of knowledge in high-speed vortex flows and as a result, the envelope of research was extended well into the hypersonic regime. By the 1970s, there was a significant research effort within the United States aerospace community focused toward aerothermodynamic issues, such as those related to the lee-side vortex flows on the Space Shuttle<sup>30,31</sup>. Also, in the 1960s and the 1970s, there was a renewed focus on leading-edge vortex shedding on slender vehicles configured for supersonic cruise flight. This research was conducted at a similar level of urgency in both the United States and Europe due to the desire to develop the first commercially viable supersonic civil transport aircraft<sup>30</sup>. The 1980s brought a re-focus on the aerothermodynamics of hypersonic flight with the National Aero-Space Plane (NASP) program<sup>30</sup>. The late 1980s and the 1990s again brought a focus on supersonic flight with the High Speed Research (HSR) program<sup>2</sup>. In the 1990s, there was also a renewed interest in hypersonic lifting-bodies as evident by the new series of X planes<sup>31</sup>. In addition to the above listed research activities there has also been a significant effort directed towards supersonic military aircraft and missiles. Examples of these vehicles include the century series fighters, SR-71, as well as all present day fighters and missiles<sup>30</sup>.

This paper will focus on vortex structures as they relate to aerospace vehicle design. Specifically, this paper will review the research conducted at the National Aeronautics and Space Administration (NASA), Langley Research Center (LaRC) into high-speed vortex flows during the 1970s, 1980s, and 1990s. During this time period, there was a significant effort by the research community at NASA LaRC to explore the off-body flowfield of aerospace vehicles in an effort to improve the aerodynamics and aero-thermodynamics of a variety of vehicles. These investigations made extensive use of on-body and off-body flow visualization test techniques and as a result the majority of the data to be presented in the paper will be primarily comprised of qualitative visualization information. This paper will show experimental data for flat plates, cavities, bodies, missiles, wings, and aircraft. However, in order to place NASA LaRC's recent high-speed research into perspective, the first section of the paper will provide a historical review of the extensive body of high-speed vortex flow research from the 1940s to the present. Also presented in this initial section will

be a brief review of the low-speed vortex flow research at NASA LaRC in the 1960s and 1970s<sup>32</sup>.

### **3.0 SYMBOLS and NOMENCLATURE**

#### **3.1 Symbols**

A.....	wing aspect ratio
b.....	wing span, in.
$C_D$ .....	drag coefficient
$C_l$ .....	rolling moment coefficient
$C_L$ .....	lift coefficient
$C_{L,\alpha}$ .....	lift-curve-slope at $0^\circ$ angle of attack
$C_m$ .....	pitching moment coefficient
$C_N$ .....	normal force coefficient
$C_{Nf}$ .....	missile fin normal force coefficient
$C_p$ .....	surface static pressure coefficient
h.....	cavity reference height, in.
$l, L$ .....	reference length or cavity length, in.
$L/D$ .....	lift-drag ratio
$M$ .....	Mach number
$M_N$ .....	component of Mach number normal to wing leading edge, $M \cos \Lambda_{LE} (1 + \sin^2 \alpha \tan^2 \Lambda_{LE})^{1/2}$
$R$ .....	Reynolds number
w.....	cavity width, in.
x.....	axial distance, in.
$y_v$ .....	spanwise position of vortex core, in.
$\alpha$ .....	angle-of-attack, deg.
$\alpha_N$ .....	angle-of-attack normal to wing leading edge, $\tan^{-1} (\tan \alpha / \cos \Lambda_{LE})$
$\beta$ .....	Mach number parameter, $(M^2 - 1)^{1/2}$
$\delta$ .....	fin deflection angle, positive leading edge up, deg.
$\delta_f$ .....	wing leading edge flap deflection, positive leading edge down, deg.
$\delta_{ROLL}$ .....	differential canard deflection angle, ( $\delta$ for port canard) - ( $\delta$ for starboard canard)
$\eta_v$ .....	vortex action line, $y_v / (b/2)$
$\Lambda_{LE}$ .....	wing leading edge sweep angle, deg.
$\phi$ .....	roll angle, deg.

### **3.2 Nomenclature**

DVT.....	Design Vortex Structure
HSR.....	High Speed Research.
LaRC.....	Langley Research Center
LE.....	LeadingEdge
LEX.....	Leading-edge extension
NASA.....	National Aeronautics and Space Administration
NASP.....	National Aerospace Plane
NFW.....	Natural Flow Wing
psfa.....	pounds per square foot, absolute
RVT.....	Resultant Vortex Structure
RPM.....	Revolution per Minute
UPWT.....	Untiatry Plan Wind Tunnel
°F.....	degree Faranheit

### **4.0 BACKGROUND and HISTORY**

Within nature there exist many mechanisms which ensure that our environment consists of smooth and continuous fields of fluid and energy. It can be easily imagined that without the inherent continuity of nature, chaos would result. These naturally occurring flow control mechanisms are seen to exist at all scales and in all fluid and energy media. An example of these mechanisms would be an expansion fan in a high-speed fluid flow. This fluid mechanism is analogous to the diffraction of energy, at a physical discontinuity, for an electromagnetic energy wave. For fluids, one of the most dramatic and powerful mechanisms is the vortex. The vortex is also one of the most consistently occurring fluid flow features in nature.

A vortex is created whenever a moving fluid encounters an abrupt discontinuity or whenever a stationary fluid is abruptly impacted by a moving boundary. This discontinuity or boundary may take the form of a physical surface, interacting fluids, or an abrupt gradient (temperature, velocity, pressure, density, or other flow parameter) in the parent fluid. Whatever the cause, the resulting flow feature is a coherent, viscous structure within the parent body of fluid in which the fluid elements have angular velocities with orientations that vary over 360°. Though simple in definition, the vortex can be a contradiction in its existence. When a vortex is formed, it can be powerful, benign, stable, unstable, as well as, forgiving. All vortex structures have the unique capability to add energy to the local flow, they can also serve as a

dividing boundary between two regions of dissimilar structured flow. The vortex may be thought of as Nature's flow-control device.

Vortices may be both naturally occurring or man-made. Naturally occurring vortex structures are observed within the universe in the form of a Spiral Galaxy (see figure 1), on other planets as evident by Jupiter's Red Spot (see figure 2), and in a variety of very large-scale atmospheric structures on earth such as hurricanes and tornadoes (see figure 3). Naturally forming vortex structures also exist as small-scale fluid structures such as an eddy which may occur near a rock in a brook or in the wake of an oar. Large eddies or whirlpools are seen in a fast moving river rapid and as the famous "Maelstrom Whirlpool" off Loften Island, Norway. Nature has also managed to integrate vortex flows into the life of various living things. These vortex structures enhance the flight performance of birds and insects and the swimming performance of fish and mammals. However, the one common characteristics of each of these natural vortex structures is that they are all low speed flows (i.e., velocities below the speed of sound).

Man-made vortex structures can exist as both low-speed and high-speed phenomena, where high-speed is defined as velocities greater than the speed of sound. Man-made vortex structures may also be divided into two categories: (1) those resulting from man's interaction with the environment, we shall refer to these as a Resultant Vortex Structure (RVS), and (2) those that are designed to perform a prescribed function by man, we shall refer to these as a Designed Vortex Structure (DVS). Common RVSs are the whirlpool in your sink and the tip vortex from a wing of an aircraft, see figure 4<sup>33</sup>. These two RVSs can be contrasted with common DVSs such as the whirlpool in your toilet bowl and the new generation of "Cyclone" vacuum cleaners on the market today. Engineers have routinely used DVSs to perform a variety of functions from particle separation<sup>34</sup> to enhanced aerodynamic performance of military fighter aircraft at low-speed and high angles-of-attack<sup>32,35,36</sup>.

It is interesting to note the diversity in use of vortex structures by man as well as by nature. One of the most diverse occurrences of vortex structures is within the aerospace community. On a single aerospace vehicle, there may exist low-speed, high-speed, resultant, and design vortex structures. The remainder of this paper will concentrate on man-made vortex structures occurring about aircraft at high-speed (supersonic).

#### 4.1 High-Speed Wing and Wing/Body Vortex Flows

High-speed vortex flows about simple aircraft shapes have been studied for over half a century by many recognizable aerodynamicists including: Jones 1947<sup>4</sup>, 1947<sup>5</sup>; Stanbrook 1959<sup>37</sup>; Stanbrook and Squire 1960<sup>38</sup>, 1964<sup>39</sup>; Kucheman 1962<sup>40</sup>, 1965<sup>1</sup>, 1971<sup>41</sup>, 1975<sup>42</sup>; von Karman 1962<sup>43</sup>; Squire 1963<sup>44</sup>, 1964<sup>45</sup>, 1967<sup>46</sup>, 1976<sup>47</sup>; Peake and Tobak 1980<sup>48</sup>, 1982<sup>49</sup>; Tobak and Peake 1982<sup>50</sup>. While most of the early investigations<sup>51-97</sup> were motivated by the design of efficient high-speed vehicles, it is interesting to note, that with the exception of Maskell<sup>25</sup> and Kucheman<sup>1</sup>, vortex flows were not viewed as desirable flow types but a resultant phenomena that must be managed at off-design conditions. Both Kucheman and Maskell recognized that the separated vortex flow about a slender aircraft satisfies all of the necessary requirements and criteria for efficient aircraft design<sup>1</sup>.

The historical body of data for wings and bodies is immense and covers a broad range of geometries and flow conditions. Summary discussions of most of these data are presented in references 35, 48, 49, 98-101. A review of these data show that all of the man made vortex structures related to aircraft fall into two broad classes as discussed by Smith in 1975<sup>102</sup>. The first class is sharp-edge separations, such as that from a sharp forebody chine or sharp leading-edge of a swept wing, see figure 5. The second general class is associated with smooth-wall vortex structure, such as that from an axisymmetric body at high angle-of-attack, see figure 6. The smooth-wall type also includes the vortex structures emanating from wing/body junctures and other smooth wall protuberances. Note, the separation patterns presented in figures 5 and 6 reflect the conical nature of vortex separation at supersonic speeds.

The sketch shown in figure 5 is for a thin, sharp-edged delta wing at angle of attack. A review of the sharp-edge separation sketch shows that the secondary vortex structures are smooth-wall separation types. As noted in the figure, the primary separation line is at the sharp leading edge of the wing with a primary reattachment line located along a straight line that emanates from the apex and lies inboard of the wing leading edge. Inboard of the primary reattachment line the flow direction on the surface is streamwise and outboard of the primary reattachment line the flow is spanwise. The spanwise flow is accelerated under the primary vortex and then undergoes an abrupt recompression and eventual smooth-wall type separation and forms the secondary vortex. As shown in the figure this smooth-wall separation point is labeled the secondary separation line. Outboard of the smooth-wall vortex is a secondary reattachment line. This pattern of smooth-

wall vortex and flow reattachment has been observed to repeat itself outboard of the secondary vortex and result in a tertiary smooth-wall vortex.

The sketch of figure 6 is for a slender cone at angle of attack. For high-speed flows, the smooth-wall vortex results from shock/boundary layer interaction. The sketch of figure 6 show that all higher-order separations for a smooth wall primary separation are of the smooth-wall type. For the situation depicted in figure 6 the smooth-wall vortex results from the flow on the windward side of the body expanding around the sides to the leeward side of the body and eventually recompressing and turning streamwise. As the angle-of-attack is increased the recompression becomes more abrupt, a shock is formed and the flow separates and forms a vortex. This is the primary separation line. Inboard of the primary separation line is the primary reattachment line. The resultant surface flow directions and secondary separation characteristics are similar to the sharp-edge separation discussed previously. Additional detailed discussions and explanation of these two flow separation types are found in numerous reports, see references 49 and 50.

##### 4.1.1 Flow Classification

An area of particular interest that has received much focus over the past 30 years has been in the classification of vortex flows on the lee-side of delta wings. Several of the first efforts were by Lee in 1955<sup>8</sup>, Stanbrook and Squire<sup>38</sup>, Sutton<sup>103</sup>, and Hall and Rogers<sup>20</sup> in 1960. The work of Stanbrook and Squire, in 1960<sup>38</sup>, is very noteworthy in that they were able to define the boundary between attached and separated flow, as a function of Mach number and angle-of-attack (see figure 7). Additional classification work has been reported by Squire, Jones, and Stanbrook in 1963<sup>47</sup>; Squire in 1976<sup>45</sup>, Szodruch in 1978<sup>104</sup>; and Szodruch and Peake in 1980<sup>105</sup>. With each subsequent effort, there were additional flow types defined as shown in figure 8. In the 1980s, the work of Miller in 1984<sup>106</sup> and Wood in 1985<sup>107-109</sup> and 1987<sup>110</sup>, as depicted in figure 9, connected and refined the various boundaries. In 1987, Ganzer<sup>111</sup> and in 1989, Covell<sup>112</sup> further refined the flow classification on the lee-side of delta wings. Additional discussion of the flow classification efforts at NASA LaRC will be presented in more detail later in this paper.

## **4.2 High Speed Missile Vortex Flows**

The high-speed vortex flow research related to missiles has been focused at developing an understanding of the interference effects between body and fins. This focus was driven by the need to eliminate uncertainty in the control laws and flight characteristics. The early missile research focused primarily on isolated axisymmetric bodies in which there were one or two pairs of vortex structures (Allen in 1951<sup>21</sup> and Rogers in 1952<sup>27</sup>). In the 1960s and 1970s, non-axisymmetric bodies with a limited number of fins were investigated (Rainbird 68<sup>113,114</sup>, Graves 79<sup>115</sup>). These concepts would have 3 or 4 pairs of vortex structures. By the 1980s, vortex flow research for missiles investigated both axisymmetric and non-axisymmetric bodies with 5 to 6 pairs of vortex structures. Examples of these studies are the work of Allen in 1979<sup>116</sup> and 1983<sup>117</sup>.

## **4.3 Other High Speed Vortex Flows**

As mentioned previously, vortex structures exist in all flow fields. This is especially true for aircraft at high speeds. A brief review of the literature show that in addition to the investigation of large scale vortex structures there has also been a wide variety of research into much smaller scale structures. An example of these efforts includes research of boundary layer instabilities (Chapman 1958<sup>18</sup>), vortex generators (Gartling 1970<sup>118</sup>, Hazelwood 1996<sup>119</sup>, Samimy 1991<sup>120</sup>), and wing/body juncture flows (Stanbrook 1959<sup>37</sup>, Greene 1988<sup>121</sup>). Research has also been conducted on vortex breakdown (Kandil 1993<sup>122</sup>), vortex flow asymmetry (Sicari 1990<sup>123</sup>), and vortex /shock interaction (Metwally 1989<sup>124</sup>, Settles 1993<sup>125</sup>) at supersonic speeds.

## **4.4 Low-Speed Vortex Flows**

Over the same time period as the high-speed research, there were an equal number of investigations into low-speed vortex flows. The main difference between the two research efforts is that a primary focus of the low-speed research has been in the use of vortex flows to improve aerodynamic performance (Lamar 1983<sup>32</sup>). The low-speed community focused on the use of vortex flow to improve the low-speed aerodynamic efficiency of slender aircraft and lifting-body vehicles as well as to improved the maneuverability of fighters at high angles-of-attack<sup>35</sup>. There have been a number of documents summarizing the low-speed vortex flow and separated flow research efforts from the 1950s to 1980s, see references 51, 53, 126-128.

## **5.0 RECENT HIGH SPEED VORTEX RESEARCH AT NASA LANGLEY**

From 1970 to 1990 researchers at the NASA Langley Research Center were actively involved in the experimental study of vortex structures at supersonic speeds as a means to improve vehicle performance and maneuverability. This section of the paper will summarize the body of work at the NASA Langley Research Center with a view toward vehicle design and flow control. A review of the types of resultant and designed vortex structures at supersonic speeds will be presented as well as a discussion of the benefits of these flow structures to vehicle performance. The information presented will cover small- and large-scale structures for a variety of vehicles from missiles to transports. The paper will present an extensive amount of flow visualization data with some supporting pressure data and force and moment results. The majority of the data to be presented has been obtained in the Langley Unitary Plan Wind Tunnel, which is a continuous flow, variable pressure supersonic wind tunnel with a Mach number range from 1.5 to 4.6. The test section is approximately 4 ft square and 7 ft long.

### **5.1 Resultant Vortex Structures**

The research emphasis at NASA LaRC during this time period has been on developing a thorough understanding of not only the aerodynamics of high-speed vehicles but of also developing a thorough understanding of the associated flow features and mechanisms which produce the resultant aerodynamics<sup>129-138</sup>. In the 1970s and 1980s, the only tool available for these studies was the wind tunnel. Through the use of various test techniques, the aerodynamicist could explore the aerodynamics and fluid dynamics of aerodynamic concepts and components. In the 1990s, computational methods have become contributors<sup>58,64,72,76,77,95,109,122,123</sup> to the investigation of these flow fields, however, the wind tunnel remains the primary exploratory tool. The efforts to understand the fluid dynamics as well as the aerodynamics have not only been driven by the need for additional types of data to support the development of advanced computational tools but have at times driven the development of advanced computational tools in order to support specific design and analysis needs.

As mentioned previously, the flow about any vehicle will usually contain one or more resultant vortex structures that may or may not contribute to the resultant aerodynamics. However, through the routine use of various flow visualization techniques to explore the flow fields, an improved understanding of vortex

flow physics and interfering flow fields has been developed. As a result, the aerodynamic community is better equipped to routinely account for the effects of vortex flows in the analysis of aerodynamic data as well as to include vortex flow effects in the design process.

To provide insight into the diversity of vortex structures which are present at high-speed a review of typical resultant vortex structures about flat plates and cavities, bodies and missiles, and wings and aircraft will be presented in the following sections. Flow visualization data will be the primary format, but where appropriate, pressure and force data will be shown to reflect the impact of the vortex structure on the aerodynamic behavior of the vehicle.

### **5.1.1 Flat Plates and Cavities**

Around 1980, the NASA Langley Research Center began studying problems related to the carriage and release of weapons from aircraft at supersonic speeds. These studies were in support of the development of a supersonic cruise fighter aircraft. One of the early studies<sup>139</sup> showed that the separation characteristics of a store exiting a cavity was primarily a result of the cavity flow field. Because of the significant influence of the cavity flow field on the store separation characteristics, a series of studies were initiated to document the flow field inside cavities in order to better understand store separation characteristics. The results of these studies showed that even simple rectangular box cavities located in a flat plate have complicated three dimensional flow fields which contain multiple vortices. The remainder of this section will describe some of the studies conducted at LaRC to understand cavity flow fields at supersonic speeds.

#### **5.1.1.1 General Description of Cavity Flow Fields**

Before describing the nature of vortex flows in cavities, it is sometimes helpful to describe the general nature of cavity flow fields. Numerous studies have been performed and reported in the literature that define the basic differences between the flow fields of shallow and deep cavities at supersonic speeds.<sup>140-147</sup> These flow fields have been termed closed and open cavity flow and correspond to flows in shallow and deep cavities, respectively. The type of flow field that exists has been shown to depend primarily on the cavity length-to-height ratio ( $L/h$ ). The flow field of cavities with  $L/h \geq 13$  is generally referred to as closed cavity flow and is characterized by a flow that separates and expands over the cavity leading edge, impinges and attaches to the

cavity floor, then separates and exits at the rear of the cavity (see Fig. 10). The corresponding pressure distribution shows a decrease in pressure at the forward section of the cavity as the flow separates and expands into the cavity, an increase in pressure as the flow impinges on the cavity floor, a pressure plateau as the flow passes along the cavity floor, and an increase in pressure as the flow exits ahead of the rear face. For cavities with  $L/h \leq 10$ , the flow field is generally referred to as open cavity flow and is characterized by a flow that passes over the cavity without any appreciable expansion into the cavity (see Fig. 10). Typical pressure distributions show a slight positive pressure coefficient over most of the cavity floor with a slight increase in pressure at the rear of the cavity caused by flow impingement at the top of the cavity rear face. Cavities with open flow typically have flow-induced pressure oscillations. This aeroacoustic effect can produce tones severe enough to cause damage to the aircraft structure, store structure, or electronic equipment.

Cavity flows that exist in the region between open- and closed- cavity flow ( $10 \leq L/h \leq 13$ ) are generally referred to as transitional cavity flows. Transitional cavity flow can be divided into two separate types of flow: transitional-closed and transitional-open. If the  $L/h$  of a cavity with closed flow is decreased, eventually the impingement shock and exit shock will collapse and form a single shock wave. The corresponding pressure distribution shows a low-pressure region at the forward section of the cavity as the flow separates and expands into the cavity with a steady increase in pressure toward the rear of the cavity. This type of flow field is referred to as transitional-closed flow (see Fig. 10). As the  $L/h$  of the cavity is reduced still further, the high-pressure region at the rear of the cavity vents to the low-pressure region at the forward section of the cavity abruptly switching the flow field so that the single shock wave that was present for transitional-closed flow vanishes indicating that the flow does not impinge on the cavity floor. For this case, the flow is turned through a series of expansion and compression waves and the flow field is referred to as transitional-open cavity flow (see Fig. 10). The pressure distribution generally shows a slight negative pressure coefficient at the forward section of the cavity indicating that the flow is partially expanding into the cavity; the pressure then increases steadily toward the rear of the cavity but does not reach as high a peak at the rear of the cavity as the transitional-closed flow case. It should be emphasized that the  $L/h$  values used above to describe the various flow fields are only general guidelines for estimating the type of flow field that exists for a given cavity. Because pressure distributions in the cavity are used to define the cavity

flow fields, they are one of the best methods for determining the type of flow field that exists in a given cavity.

### 5.1.1.2 Flow Visualization of Cavity Flow Fields

Various types of flow visualization have been used to document the surface flow and off-surface flow fields of cavities. These techniques include schlieren, vapor screen, oil flow, and colored water flow.

The results describing the surface flow fields of cavities using a colored-water technique and those describing the off-surface flow fields using a vapor screen technique will be discussed in this section.

#### 5.1.1.2.1 Surface Flows on Cavity Floor

During one cavity flow field test, water was injected through pressure measurement orifices located on the model surface in an attempt to visualize vortices that typically form above certain cavity configurations. Because of the low static pressure in the tunnel, it was anticipated that the water would vaporize as it exited the orifice and the resulting vapor would be entrained into the vortices and render them visible. This technique did not work, and the water instead flowed along the model surface. Although the water was difficult to discern against the model surface, it was obvious that the water was being entrained by the model surface flows and had a fast response to the cavity flow unsteadiness. This impetus led to the development of a technique that uses colored water as a medium to visualize surface flows over wind-tunnel models.<sup>148</sup>

The colored-water surface-flow visualization technique basically involves injecting colored water through the pressure measurement orifice tubes installed in a wind-tunnel model. The colored water exits the orifices and flows along the model surface to form streaklines. The resulting flow patterns are then photographed. For the test data presented colored water was injected through pressures orifices located along the floor of the cavity and on the flat plate surface ahead of the cavity.

The wind-tunnel model (fig. 11) used in this investigation consisted of a rectangular box cavity mounted in a flat plate. The rear face of the cavity was attached to a remotely controlled electrical drive mechanism that allowed the rear face to move and thus, vary the length of the cavity while the tunnel was in operation. The cavity height ( $h$ ) and width ( $w$ ) were 0.5 in. and 2.5 in., respectively, and were held constant throughout the entire test, while the cavity length ( $L$ )

was varied from 12 in. to approximately 0.5 in. The cavity leading edge was 10.4 in. aft of the flat plate leading edge. The boundary layer on the plate was turbulent, having been tripped at the plate leading edge with sand grit. All of the tests were conducted with the cavity at an angle of attack and side slip of  $0^\circ$ .

The tests results presented in this section of the paper were conducted at the conditions shown in table 1 in the low Mach number test section of the Langley Unitary Plan Wind Tunnel<sup>149</sup>. The model was vertically mounted in the wind tunnel to allow video and still photographic data to be obtained through the test section windows. The model was painted white for good contrast with the colored water and was illuminated with three flood lamps.

Table 1. Colored water flow test conditions.

Mach number	Reynolds number, 1/ft	Total pressure, psfa	Total temperature, °F
1.50	$2.0 \times 10^6$	1051	125
2.16	$2.0 \times 10^6$	1349	125

Shown in figure 12 are a series of photographs that were acquired as the cavity length was decreased at a Mach number of 1.50. Also included in figure 12 are sketches of the streaklines indicating the direction of flow. The free-stream flow is from left to right and the scale located on the flat plate above the cavity indicates the cavity length in inches. Colored water was injected from two orifices located on the flat plate ahead of the cavity and from three orifices located on the cavity floor approximately 3 in. aft of the forward face. For the cavity with  $L/h = 24$  (closed flow), the streaklines on the flat plate surface curve into the forward section of the cavity and indicate that the flow is expanding into the low pressure region. At the rear of the cavity, these streaklines curve away from the cavity as the flow exits from the high pressure region. On the cavity floor, two vortices have formed ahead of the rear face as indicated by a merging of the center cavity floor streaklines with each of the two side cavity streaklines. Note, the water color for these streaklines (yellow — middle orifice, blue — outside orifices) was chosen so that as the streaklines merged to form vortices, a new color (green) was formed. The formation of new colors from the merging of flows greatly enhances the data analysis. The upper vortex has a counterclockwise rotation and the lower vortex has a clockwise rotation. As the cavity length is reduced from  $L/h = 24$  to  $L/h = 13$ , these vortices maintain the same rotation direction. At an  $L/h = 13$ , the vortices start to dissipate and begin

to form in the opposite direction as indicated by the small amount of green water moving up the center of the cavity. The flow pattern on the floor of the cavity represents the starting point of these vortex structures. These vortex structures emanate from the cavity floor and extend upward and downstream. As the cavity length is reduced still further but before the vortices can completely form in the opposite direction, the flow field rapidly switches from transitional-closed to open flow ( $L/h = 12$ ); the streaklines on the cavity floor flow upstream and the streaklines on the flat plate surface do not curve into the cavity.

Shown in figure 13 are a set of photographs illustrating cavity surface flows at a Mach number of 2.16. The primary difference between the results at Mach 1.50 and 2.16 are the details of the formation of the vortices at the rear of the cavity. For  $L/h = 24$  (closed flow), the two vortices ahead of the rear face have the same rotation direction as the Mach 1.50 case. However, in contrast to the  $M=1.50$  case, some of the blue/green water has broken away from the vortices and entered the yellow colored water at the rear of the cavity indicating that the vortices are starting to form in the opposite direction. As the cavity  $L/h$  is decreased to approximately 17, the two vortices at the rear of the cavity have dissipated and two new vortices, that together span the entire cavity width, have formed. These two new vortices have rotation in the opposite direction to the original vortices. At an  $L/h$  of approximately 14, these two vortices cover nearly one half of the entire cavity floor. Decreasing the cavity length still further to an  $L/h$  of approximately 13, the flow rapidly switches from transitional-closed to open flow and the blue and yellow water streaklines flow upstream. The flow reversal indicates that a large recirculation region exists inside the cavity for open flow.

Figure 14 shows a close up of the rear portion of the cavity at for  $L/h = 24$  at both  $M=1.50$  and 2.16. These photographs illustrate the significant effect of Mach number on the cavity flow field. Yellow tinted water is being injected from an orifice located on the cavity floor 3.25 in. downstream of the cavity forward face and blue tinted water is being injected 0.50 in. forward of the rear cavity face. At both Mach numbers, the blue tinted water from the rear most orifice flows upstream and merges with the yellow tinted centerline water flow before being entrained into the vortices at the edges of the cavity. The flow fields at these two conditions are very similar, the primary difference is the spreading of the centerline flow field at a cavity length between 9.5 and 10.0 in. At  $M=2.16$ , the mixing of the yellow and blue water to form green occurs in a blunt curved area near the  $L = 9.75$  in. point. In contrast, at  $M=1.50$ , the

mixing of the yellow and blue water occurs at a sharp point near  $L = 10.00$  inches. The spreading of the flow at  $M=2.16$  is the start of the vortices that eventually form in the opposite direction to the edge vortices as the cavity length is decreased.

Vortices can also form at the forward section of the cavity. Figure 14 shows colored water surface flows at the forward section of the cavity at  $M=1.50$  for two different  $L/h$  values that are in the open cavity flow region. For the  $L/h = 5$  case, blue tinted water was injected from an orifice on the cavity floor 1.75 in. aft of the forward face. The water flows upstream and forms two counter rotating vortices in the corners behind the cavity forward face. As the cavity length was decreased further to an  $L/h$  of approximately 1.1, the two counter rotating vortices have each split into two counter rotating vortices each for a total of four vortices that span the cavity width. The blue tinted water for this case was injected two inches ahead of the cavity on the flat plate surface.

Figures 12-15 have illustrated some of the complex vortical surface flows in cavities at supersonic speeds. Eventhough the exact cause or causes of these vortices are basically unknown, it is clear that their impact on cavity aerodynamics and store separation from the cavities can be significant. Also note that despite the observed global flow structures about cavities is steady and stable.

#### **5.1.1.2.2 Off-Surface Cavity Flow Fields**

The vapor screen technique has been used to visualize off-surface flows in cavities. This technique consists of injecting water into the tunnel circuit until a fog is formed in the test section. The fog is a result of the water vapor condensing as the static temperature of the air decreases in the expanding flow of the tunnel nozzle. A thin light sheet is passed across the test section illuminating the fog. Figure 16 shows a schematic of the vapor screen technique as applied in the NASA LaRC UPWT. Typically, the light sheet remains stationary while the model is traversed longitudinally through the light sheet. In recent years, a laser-based system generated the light sheet instead of a mercury vapor lamp which was used routinely in years past. Photographs of the fog and light sheet are recorded with a still camera located inside the test section or mounted on the tunnel access doors. A complete description of the vapor screen technique used in the NASA LaRC UPWT is presented in reference 150.

Two types of flow phenomena that can be visualized with the vapor screen technique are shock waves and boundary-layer separation regions such as vortices. Shock waves are revealed by the variation of the illuminated light sheet intensity. Vortices are revealed by dark areas where no particulates exist to reflect light from the light sheet.

Shown in figure 17 are vapor screen photographs illustrating both open and closed cavity flow<sup>146</sup>. The model used for these tests was a flat plate with a cavity mounted in the center of the plate similar to the plate used in the colored water flow photographs shown in the previous section. The cavity was 12 in. long, 2.5 in. wide, and the height was 1.88 in. and 0.50 in. for the open and closed cavity flow cases, respectively. The photographs view the cavity from downstream of the model looking upstream. Four photographs are presented for each case at four longitudinal locations along the cavity length. For the open cavity flow case ( $L/h=6.4$ ), no vortices or shock waves are visible along the entire length of the cavity. In contrast, at  $x=6.0$  in. for the closed cavity flow case ( $L/h = 24.00$ ), two well formed vortices have developed along the cavity edges. These vortices are a result of the flow expanding into the cavity at the cavity sharp leading edge and along the cavity sharp side edges just downstream of the forward cavity face. The colored water flow photograph in figure 14 for  $L/h=24.00$  shows the red tinted water that was injected on the flat plate surface ahead of the cavity curving into the cavity thus, illustrating how the sharp edge vortices actually develop. In addition to the edge vortices at  $x=6.0$  in., the impingement shock that forms as the flow impinges on the cavity floor can also be seen. At  $x=12$  in. which is at the cavity rear face, the two edge vortices are still present and both the impingement and exit shocks can be seen. Downstream of the cavity on the flat plate surface at  $x=14$  in., the edge vortices can still be seen although they are starting to dissipate. These vapor screen photographs illustrate the complex three-dimensional flow field of cavities.

The vortices which form along the cavity sharp edges for closed flow, as shown in the vapor screen photographs, can effect the pressure distributions on the cavity rear face. Shown in figure 18 are lateral pressure distributions across the rear face of a cavity at four  $L/h$  values<sup>140</sup>. These data were obtained on the same flat plate used in the colored water flow photographs. To vary the cavity  $L/h$ , the cavity length was varied while the cavity height remained constant. At an  $L/h$  of 24 and 16, the cavity flow field would have closed flow. The data for these two cases show significant lateral pressure gradients across the rear face. These pressure gradients are generally symmetrical about the cavity centerline with the peak pressures occurring off the

cavity center line. Reference 140 attributes these gradients to the impingement of the cavity edge vortices on the rear face. In contrast, the data for  $L/h = 4$  shows a much reduced pressure level and smaller gradients than for the closed flow cases. At  $L/h=1$ , the lateral pressure gradients have essentially disappeared.

Vapor screen photographs have also been obtained in a cavity with a generic ogive cylinder inside the cavity<sup>151</sup>. The purpose of this test was to provide a data base on a generic store separating from a generic weapons bay. Figure 19 shows a schematic of the model mounted in the UPWT test section. The cavity was located in a flat plate that was vertically mounted and spanned the entire test section from floor to ceiling. The cavity was 5.768 in. wide, 29.362 in. long, and 2.432 in. high. The store was mounted on the tunnel model support system which has the capability to traverse the test section from side to side thereby moving the model into and out of the cavity. The store was 24.028 in. long and 1.20 in. in diameter with an ogive nose of radius of 11.51 in. Figure 20 shows vapor screen photographs of the cavity with and without doors at  $M = 2.65$  with  $L/h=12.07$ . For the case without doors, two well formed sharp-edge vortices can be seen at the cavity side edge. In addition, one of two smooth-wall vortices on the store can be seen. The vortices on the store are caused by the flow expanding into the cavity which places the store in a localized upwash region. In other words, the store appears to be at an angle of attack. The second vapor screen photograph shows the cavity with doors. The doors are opened parallel to the cavity sidewalls and are one half of the cavity width tall so that if they were closed the cavity would be covered. The results for this case are similar to the doors off case except that the cavity side edge vortices have been replaced by vortices emanating from the outer edges of the cavity door. The smooth-wall vortices on the store are also better defined than the no doors case.

### **5.1.2 Bodies and Missiles**

In this section of the paper, vortex patterns and their measured effects on the aerodynamics of bodies and missiles are examined. The vortex images shown here are from vapor screen images taken at supersonic speeds from tests in the NASA LaRC Unitary Plan Wind Tunnel (UPWT). The material presented will start with simple shapes and effects and transition to more complex geometries and flow fields. All flow visualization data presented in this section has been obtained with the vapor-screen flow-visualization technique discussed previously.

### 5.1.2.1 Axisymmetric Body

The vortex structures observed on bodies and missiles include both smooth-wall and sharp-edge separation on the bodies and sharp-edge separation on the missile fins. For the present discussion forward-body fins will be labeled canards, mid-body fins will be labeled wings, and aft-body fins will be labeled tails.

Figure 21 shows a simple axisymmetric body with cruciform wings mounted in the UPWT high speed test section. The flowfield images on this model were obtained in support of the study documented in Reference 152. The model has been painted black to prevent reflection from the laser light sheet that was used to make the vortex images visible. Also shown in this figure are a ceiling-mounted still camera and a strut-mounted video camera that were used to record the vapor-screen images.

Tests on this model were performed with and without the wings attached. Figure 22 shows a composite of three vapor-screen images at different longitudinal stations on the body without wings. These data are for a Mach 2.5 and  $14^\circ$  angle of attack. Two symmetric body (smooth-wall) vortices can be seen that originate on the nose and continue to grow down the length of the body. The feeding sheet, which permits these vortices to continue to grow, can also be seen.

Figure 23 shows this configuration with the wings attached at a roll angle of  $0^\circ$  (tails in + orientation) for the same test conditions as those of Figure 22. Note that the horizontal wings break up the feeding sheet for the body vortices, which no longer continue to grow over the rest of the body. The horizontal wings themselves develop a vortex along the leading edge (sharp-edge separation) that becomes detached downstream of the wing trailing edge. Note that only the flow structures on the left-hand-side of the model are visible because the vertical wings block the laser from illuminating the right hand side of the model. The top and bottom (vertical) wings produce no vortices since they are not at incidence to the oncoming flow at this roll angle. The last image ( $x/L = 0.96$ ) shows that at the base of the body there are two body vortices that appear smaller than those on the body alone. The reduced size of the body vortices is a result of their feeding sheet being cut by the wing. This image also shows two stronger sharp-edge vortices that originate from the horizontal wings.

Figure 24 shows data from a similar tail-body configuration as those shown in figure 23. The data illustrates the effects that the body vortices can have on the tail loads<sup>153</sup>. This figure shows the measured

normal force coefficient on a single tail as it is rolled from windward to leeward at three angles of attack. The Mach number is 2.0 and there are no tail deflections. The dotted circle highlights the region of force reversal due to these interfering vortex flows. Note that when the tail orientation approaches a roll angle of  $180^\circ$  at  $\alpha = 20^\circ$ , the normal force on the tail becomes negative; that is, in the downward direction even though the configuration angle of attack is  $20^\circ$ . This force reversal effect occurs when the tail is rotated to a location that positions body vortices on the lower surface of the tail. This effect is not present in the  $\alpha = 5^\circ$  data because the body vortices are too weak at this angle of attack. Also, the effect is greatly reduced at  $\alpha = 35^\circ$  because the vortices have moved far enough away from the body that they have a smaller effect on the tails. These data emphasize the importance of designing the body and tails to maximize positive vortex -interference effects.

Figure 25 shows a photograph of the variant of the sidewinder missile mounted in the UPWT low speed test section. Data from this model will be used to illustrate canard-tail vortex interference effects that can occur even at low angles of attack. Figure 26 shows the rolling moment on this configuration for a  $-10^\circ$  canard roll deflection ( $5^\circ$  on each of the horizontal canards). Data are shown for several tail fin spans, including tail off. The Mach number is 2.5 and the configuration roll angle is  $0^\circ$ <sup>154</sup>. For the tail-off case, the canard deflections produce a rolling moment coefficient on the entire configuration of about  $-1.1$ . For the tail on case the data show that as tail span increases, the configuration rolling moment control authority decreases at low angles of attack and changes sign near  $\alpha = 0^\circ$  for the larger tails. (It should be noted that tail size C is close to the size of the current sidewinder missile tail fins.) Thus, the canards produce both a downwash and upwash as well as a vortex flow field that interacts with the tails at low angles of attack to produce a tail rolling moment opposite to that generated by the canards. For the larger tail sizes, the vortex induced rolling moment negates the rolling moment input from the canards, and near  $\alpha = 0^\circ$ , a small rolling moment in the opposite direction is produced. This data suggest that a re-orientation of the tail fins to an "x" arrangement would result in positive interference effects at all angle of attack.

The next three figures (Figures 27–29) show vapor-screen vortex images on a Sparrow missile model at Mach 2.36 with no wing or tail deflections. These images are taken from Reference 116. Figure 27 shows the longitudinal vortex development on the configuration at  $\alpha = 11.4^\circ$  and zero roll angle. This

figure shows a vortex pattern that is similar to that seen on the missile model shown in figures 22 and 23. This pattern of vortex structure remains unchanged as the vortices flow aft over the tail fins. Figure 28 shows the effects of roll angle on this configuration. Vortices that were not present on the upper and lower (vertical) wings at zero roll angle show up as roll angle increases. The vortex pattern is asymmetric for  $\phi = 22.5^\circ$  but becomes symmetric again about the vertical plane at  $\phi = 45^\circ$ . Now, however, vortices are visible from all four forward wings as well as from the body. Figure 29 shows the effects of angle of attack on the size of the vortices for this configuration at the base of the body at zero roll angle. The vortices get larger with increasing angle of attack but move further away from the body.

Figure 30 shows a cruciform canard-tail configuration somewhat similar to the sidewinder missile variant shown earlier, except that the tail section of this configuration is mounted on bearings that are free to roll in response to the aerodynamic loads<sup>155</sup>. Figure 31 shows the effects that the canard flow field has on this type of configuration. In this figure, the Mach number is 2.5, the roll angle of the fixed section of the model (ahead of the tail section) is  $0^\circ$ , and a roll deflection of  $10^\circ$  is input from the canards ( $5^\circ$  on each of the horizontal canards). Three cases are shown: (1) the tail section is fixed in place in the "+" orientation (tails aligned with the canards), (2) the tail section is fixed in place in the "x" orientation (tails  $45^\circ$  offset from the canards), and (3) the tail section is free to roll. The canard flowfield causes the free-to-roll tails to spin at about 1000 RPM at low angles of attack. This spin rate stays fairly constant with angle of attack until about  $\alpha = 6^\circ$ , when it begins to decrease and stops at about  $\alpha = 12^\circ$ . Note that for small angles-of-attack the configuration rolling moment for either of the fixed-tail configurations is very small, as was seen in the sidewinder variant model shown earlier. For the free-to-roll tail configuration, however, the canard roll deflection remains effective and fairly constant with angle of attack. Note, moreover, that the rolling tail has very little effect on the configuration pitching moment. Thus, the free-to-roll tail produces the desired configuration rolling moment without reducing the longitudinal stability of the configuration.

#### **5.1.2.2 Non-axisymmetric Body**

Figure 32 shows an elliptic body (with a major-to-minor axis ratio of 3) mounted in the UPWT high speed test section<sup>117</sup>. The data of figure 33 shows vapor-screen vortex patterns obtained on this body along with sketches of the observed smooth-wall vortex structures

at Mach 2.5,  $\alpha = 20^\circ$ , and roll angles of  $0^\circ$  and  $45^\circ$ . At  $\phi = 0^\circ$ , the body vortices are symmetric and the feeding sheet forms at the side edge of the body. As shown on the right side of this figure, at  $\phi = 45^\circ$ , the size of both vortices decrease with roll angle and the more windward feeding sheet moves close to the body surface. The more leeward vortex moves far away from the body. A review of the force data of reference 117 shows that these vortices increase the lifting efficiency of this elliptic body.

The elliptical configuration shown in figure 32 had a companion configuration with the same elliptical mid-body but transitioned from a blunt hemispherical nose and then into a circular base. Vapor-screen images of the vortex structures for this configuration are shown in figure 34. For zero roll angle, the smooth-wall vortices emanating from the side of the body are similar to those seen on the completely elliptical body with sharp nose. However, the data of figure 34 show the addition of a thin vertical smooth-wall separation (vortex) originating on the blunt nose and continuing down the leeward centerline of the body. At  $\phi = 45^\circ$ , the side vortices have shifted in a similar way that was seen on the completely elliptical body but the thin vortex from the blunt nose remains perpendicular to the plane of the body. At the aft end of the body the thin nose vortex actually attaches itself to the leeward side vortex feeding sheet.

Figure 35 show vapor screen photographs depicting vortex patterns on a chined forebody model at Mach 2.0 and  $16^\circ$  angle of attack. Also shown in the figure is a photograph of the model mounted in the UPWT low speed test section (reference 138). A review of the model photograph shows the existence of a metric break running circumferentially around the model at a  $x/L$  of 0.60. The portion of the model aft of the metric break was used to minimize base effects on the forebody flow-field and forebody aerodynamics. The vortex structure shown in the figure is a result of a sharp-edge separation occurring at the chine. Note that the feeding sheet of the body vortices is seen to emanate from the chine edge of the body. It appears that the metric break disrupts the body vortex feeding sheet and a second smaller vortex begins to grow along the chine side edge downstream of the metric break.

#### **5.1.3 Wings and Aircraft**

A review of existing experimental data for wings and wing/body geometries, references 156-169, reveals that a wide array of vortex flow structures are present at both low- and high-lift conditions. It is also interesting to note that changes in Mach number and geometry do

not always result in a significant change in the occurrence of these structures. In an effort to highlight the various types of vortex structures present on wings and wing/body geometries as well as the effect of flow conditions, various data are presented in figures 36 through 45.

With the exception of the data of figure 39, all of the data presented in figures 36 through 45 have been obtained in the LaRC UPWT over a Mach number range of 1.6 to 3.5. The observed structures are a combination of both sharp-edge flow separation type and smooth-wall flow separation type, see figures 5 and 6, respectively. The sharp-edge vortex types shown in the following figures include: leading-edge vortex formation from a sharp edge wing, LEX, or strake, tip vortex formation from a wing or canard, and the vortex from a sharp wing/body juncture discontinuity. The various types of smooth wall (shock induced) separations, such as from the side of a slender body, on the lee-side of a wing, and at a blended wing/body juncture region contrast the sharp edge separations.

### **5.1.3.1 Sharp Leading Edge Wings**

Presented in figures 36 and 37 are data obtained for variable leading-edge sweep (ogee) wings with sharp leading edges, references 158 and 166, respectively. Both of the concepts shown in figures 36 and 37 have been designed for efficient supersonic cruise and improved performance at increased lift coefficients. The data presented in figure 36 is for a highly cambered wing at  $5^\circ$  angle-of-attack and a Mach number of 2.4 and the data presented in figure 37 is for a mildly cambered wing with canard at  $12^\circ$  angle-of-attack and a Mach number of 1.8.

As discussed in reference 158, the design objective for the wing shown in figure 36 was to employ camber to eliminate or delay wing leading-edge vortex formation to high-lift coefficients in order to improve high-lift performance. Vapor screen photographs of figure 36 show the simultaneous existence of both a smooth-wall vortex emanating from the very low sweep nose region of the highly cambered ogee wing and a sharp-edge leading-edge vortex. This sharp edged vortex resides on the surface of the geometry and is also referred to as a leading-edge bubble. It may appear counter intuitive that a wing with a sharp leading-edge geometry will have a smooth-wall separation, however, the combination of very low sweep at the nose and a very high Mach number creates a flow condition very similar to that which occurs for a blunt body. The flow at the apex remains attached as it expands around the sharp leading edge but then undergoes a rapid recompression that separates the flow.

A review of additional data from reference 158 shows similar vortex flow features for a reference uncambered wing. However, the uncambered wing that has the same vortex flow structure as the cambered wing, has a 16% loss in aerodynamic performance ( $L/D$ ) compared to the cambered wing. The data of reference 158 also show that these vortex structures are non-interfering phenomena that occur over a wide range of flow conditions and for a variety of other camber shapes. The similarity in vortex flow characteristics for the cambered and uncambered wings support the argument that the existence of vortex flow does not always degrade aerodynamic performance at supersonic speeds.

The design objective for the ogee wing shown in figure 37 was to employ the downwash from a canard to eliminate or delay wing leading-edge vortex formation in order to improve performance at cruise ( $C_L = 0.1$ ). Similar to the observations from figure 36, the vapor screen photographs of figure 37 also show the existence of two non-interfering vortex structures on the lee-side of the wing. However, unlike the data of figure 36, these structures are both sharp-edge vortex structures that emanate from the canard tip and the wing leading edge. Despite the existence of these two vortex structures, the data of reference 166 show that the wing with canard has improved drag-due-to-lift characteristics at all lift conditions, compared to the wing without canard.

Shown in figure 38 are the lee-side vortex flow characteristics of another design study for a wing with canard<sup>167</sup>. This study also attempted to use canard downwash to suppress vortex formation on the main wing in an effort to improve cruise performance ( $C_L = 0.1$ ). The design study of reference 167 was performed on a  $70^\circ/20^\circ$  sweep cranked arrow with a  $55^\circ$  swept canard for a Mach number of 1.8. Both the canard and wing had sharp leading edges. Similar to that observed in figure 37, the photographs of figure 38 show the existence of two non-interfering vortex structures on the lee-side of the wing. These structures are both sharp-edge vortex structures that emanate from the canard tip and the wing leading edge. Additional data of reference 167 show similar wing flow features were present on the wing without canard configuration. Despite the existence of these two vortex structures the data of reference 167 show that the wing with canard has improved drag-due-to-lift characteristics at all lift conditions, compared to the wing without canard.

#### **5.1.3.1.1 Interfering Vortex Structures**

Presented in figures 39<sup>160</sup> and 40<sup>161</sup> are interfering lee-side vortex flow structures for strake/LEX and wing geometries at Mach numbers of 1.6 and 3.5, respectively. The images presented in figures 39 were obtained on a 65°-swept delta wing with a 65°/90° swept strake at an angle-of-attack of 24° and a Mach number of 1.6. The data of figure 39 show the development of a sharp-edge leading-edge-extension (LEX) vortex structure that interacts with the sharp-edge wing vortex structure. These data also show the existence of various shock structures located above the combined strake/wing vortex structure and between the two primary strake/wing interacting vortex structures. A review of the wing surface pressure data and force data for the 65°-delta wing with and without strake<sup>160</sup> show that despite the strong interaction of the vortex structures there is a negligible impact of this interaction on the surface loading and resultant aerodynamic performance.

Presented in figure 40 are data for a 70°-swept delta wing with an 82.6° strake at an angle-of-attack of 10° and a Mach number of 3.5<sup>161</sup>. These data show the development of a smooth-wall vortex structure emanating from the forebody and a sharp-edge strake vortex structure. The data show the strake vortex structure completely enveloping the weaker forebody vortex prior to the start of the wing leading-edge. Unlike the strong strake/wing vortex interaction of figure 39 the smooth-wall forebody vortex structure of figure 40 is relatively weak and thus, it is easily dominated and consumed by the strake vortex structure.

#### **5.1.3.2 Blunt Leading Edge Wings**

Compared to the previously discussed vortex structures the next three figures show relatively weak vortex structures that may exist on blunt leading-edge wings and wing/body geometries. The vortex structures presented in figures 41, 42, and 43 are primarily smooth-wall vortex flows resulting from wing lee-side shock-induced separation and wing/body juncture flows.

Depicted in figure 41 is a vapor screen photograph for a cambered, blunt leading-edge 70°/66° cranked-arrow wing/body at an angle-of-attack of 10° and a Mach number of 1.80<sup>168</sup>. Also shown on the figure are the trimmed drag characteristics at Mach 1.8 for the cambered and a reference flat wing. The vapor screen image, for the cambered wing, show the presence of a shock induced (smooth-wall) vortex structure residing at 50% of the local semispan. A review of drag data of

figure 41 show that at this condition the cambered wing has improved performance, compared to the uncambered wing. A review of additional aerodynamic and flow visualization data from reference 168 indicates that the separated vortex flow structure on the wing does not degrade the aerodynamic performance.

Similar observations and conclusions can be drawn from the information presented in figures 42 and 43 as well as the supporting data contained in references 157 and 162, respectively. Figure 42 shows results for a 55° swept delta wing/body with an uncambered blunt leading edge wing at various lift coefficients and a Mach number of 2.16. At the higher lift coefficients, the data show the existence of a shock-induced vortex structure as well as a wing/body juncture vortex. The data of figure 43 also show that a shock-induced vortex structure is present for the 50°-swept delta wing/body with an uncambered blunt leading-edge wing at 12° angle-of-attack at a Mach number of 1.6. Note, the wing/body juncture vortex structure observed in figure 42 is not present in figure 43 due to a combination of the lower Mach number and improved blending of the wing/body juncture. A review of the aerodynamic data and additional flow visualization data of references 157 and 162 show that despite the existence of smooth-wall vortex structures both wings provide excellent aerodynamic performance.

#### **5.1.3.3 Multi-Body Aircraft**

The final two figures to be discussed in this section of the paper contain data taken from reference 163. These data are for a multi-body concept employing a sharp leading edge 65°-delta wing outboard panel (figure 44) and a multi-body concept employing a 20°-trapezoidal (trap) wing outboard panel with a sharp leading-edge (figure 45). A pair of axisymmetric bodies separates the outboard wing panels, for the two multi-body concepts, from a common 60° swept inboard wing panel with a sharp leading-edge. The data of figure 44 and 45 are for an angle-of-attack of 16° at a Mach number of 2.16. The data presented in both figures show the existence of a very complex combination of shocks and flow separation. The flow separation structures of figures 44 and 45 consist of sharp-edge and smooth-wall vortex structures as well as non-vortex flow separation caused by shock/boundary layer interactions. The data of figure 44 show sharp-edge wing leading-edge vortex structures from both the inboard and outboard wing panels, a shock-induced vortex structure (which has merged with the inboard wing vortex), and a smooth-wall vortex structure emanating from each of the forebodies. The observed flow features for the 20°-trap multi-body concept (see

figure 45) are very similar to those observed for the 65°-delta multi-body concept (see figure 44) with the exception of the outboard wing panel vortex structure. The data of figure 45 show the existence of a smooth-wall shock-induced vortex structure for the 20°-swept wing. The data of figures 44 and 45 and additional results from reference 163 show that despite the numerous vortex structures that exist for these concepts, they have very good aerodynamic performance compared to existing single-body aircraft.

The data presented in figures 36 through 45 show that a wide variety of resultant vortex flow structures exist on all vehicles at high speed. These data in combination with additional results from references 156, 159, 164, 165 have shown that despite the existence of these vortex structures excellent aerodynamic performance is realized. It is important to note that the vortex structures observed on all of these geometries are steady and stable.

## **5.2 Designed Vortex Structures**

The design of efficient supersonic and hypersonic aircraft have historically focused on maintaining attached flow over the full vehicle, under the assumption that attached flow<sup>170-180</sup> would produce optimum performance. The attached flow design approach assumes that the flow will only separate at the trailing edge of the wing. However, it is well known that for a vehicle in flight, independent of flight speed, there are numerous vortex structures that will be present. Examples of these structures are vortices, which emanate from the wing tips, wing/body juncture, shocks/boundary layer interaction, and vehicle base (rearward facing step). Each of the above listed vortex structures is of the resultant type.

In the early 1980s, it was postulated that for slender geometries improved aerodynamic performance could be achieved at cruise through the use of a leading-edge vortex structure<sup>177,180-182</sup>. It was further argued that the resulting geometry would be lighter and less complex than a highly twisted and cambered design. In an effort to address this goal, a parametric study was conducted on a family of delta wing models at Mach numbers from 1.6 to 4.6. The delta wing planform was selected because of the extensive historical data available for analysis and the ease in which simple and robust geometric and flow parameters can be used to extend these results to other geometries.

In this section of the paper, the effect that leading-edge sweep, leading-edge bluntness, wing thickness, location of maximum thickness, and camber has on the

aerodynamics of and flow over delta wings will be discussed and the methods for visualizing these flowfields will be examined. The following discussion will first review and characterize the aerodynamics<sup>182</sup> and then the flow fields for delta wings (i.e. separation bubble, classical vortex, vortex with shock, etc.)<sup>106-112</sup>. This will be followed by a wing design discussion in which the understanding of the character of the flow over such wings will be highlighted.

### **5.2.1 Fundamental Aerodynamic Characteristics of Delta Wings**

At supersonic speeds, the aerodynamics of delta wings has historically been correlated with parameters relating to the leading-edge flow condition and wing leading-edge sweep. These correlation parameters have typically been derived from linear theory and have not been based upon experimental observations.

To establish a point of reference for the following discussion a brief review of several correlation parameters will follow. Figure 46<sup>182</sup> graphically depicts the range of several of these parameters for the Mach number and wing leading edge sweep to be discussed in this section. Figure 46a shows the variation in aspect ratio ( $A$ ) of delta wings with the leading-sweep angle ( $\Lambda$ ) and figure 46b illustrates the relationship between Mach number ( $M$ ) and the leading-edge sweep parameter ( $\beta \cot \Lambda$ ). Note that  $\beta$  is the supersonic Mach parameter,  $(M^2 - 1)^{1/2}$ . A leading-edge sweep parameter value of 1.0 corresponds to a sonic leading-edge condition. Thus, a Subsonic LE condition occurs for  $\beta \cot \Lambda$  values  $< 1.0$  and a Supersonic LE condition for values  $> 1.0$ . A supersonic wing leading-edge condition indicates that the flow normal to the wing leading edge is supersonic and based upon a 2-D airfoil analysis a large wave drag penalty would result. However, it is well known that this wave drag penalty is never manifested on representative swept wings. This is because the notion of a subsonic and supersonic leading edge condition is not a description of the governing physics but a description of the relationship of the Mach angle to the wing leading edge sweep angle. Despite the limitations and inherent restrictions of linear theory to model the aerodynamics of wings dominated by vortex flows, the parameters discussed above are still useful for the correlation of aerodynamic and flow-field observations at low angles of attack.

Presented in figure 47<sup>182</sup> is the variation in lift curve slope with  $\beta \cot \Lambda$  for thin, thick, sharp, and blunt delta wings. The data of figure 47 are for flow fields that vary from attached flow to sharp-edge vortex

separation. Note, at supersonic speeds the zero-lift lift-curve-slope is typically maintained to lift coefficients greater than 0.30. This behavior of the wing supersonic lifting characteristics allows for an efficient assessment of the aerodynamics over a broad Mach and angle of attack range. Also note that the drag of a thin, swept wing is inversely proportional to the lifting characteristics. Thus, the lift-curve slope is a direct indicator of the drag due to lift of these slender wings.

Figure also shows the linear theory estimates, which is independent of thickness and bluntness. It is interesting to note that the data for all wings collapses to a narrow band at low values of  $\beta \cot \Lambda$ . At these small values of  $\beta \cot \Lambda$  (i.e. small disturbances) linear theory does an acceptable job of matching the experimental data. However, at higher values of  $\beta \cot \Lambda$  linear theory over predicts the lift curve slope of thin, sharp leading edge delta wings but more closely matches the trends for blunt leading-edge and thick delta wings. These data suggest that the aerodynamic performance of thin, slender wings at supersonic speeds and low  $\beta \cot \Lambda$  is a function of Mach number and angle of attack but less sensitive to wing geometry and flow field.

### **5.2.2 Vortex Flow Characteristics of Delta Wings**

As discussed previously, the supersonic flow over delta wings at angle of attack is dominated by nonlinear separated vortex flows. A review of existing data show that the experimental studies of lee-side flow field characteristics of delta wings have used the Mach number and angle-of-attack normal to the wing leading edge<sup>38</sup> as the primary correlation parameter. Unlike the  $\beta \cot \Lambda$  parameter discussed above, the  $M_N$  and  $\alpha_N$  parameters account for angle of attack as well as geometry in defining the flow conditions at the wing leading edge.

The next three sections will discuss the flow over delta wings in supersonic flowfields. The first section will describe the flow over zero-thickness wings. The following three sections will discuss the effect of thickness and camber on the flow structures over delta wings and how these can be utilized to design wings.

#### **5.2.2.1 Zero-Thick Wings**

The flow over flat, zero-thickness wings can be characterized as attached (both upper and lower surfaces) for zero angle of attack. At angles of attack greater than  $0^\circ$ , these wings follow the classification pattern defined for lee-side flows in figure 48, as a

function of the normal Mach number and normal angle-of-attack<sup>106</sup>. The flow structures represented in figure 48 are a combination of sharp-edge and smooth-wall vortex structures.

The right side of the figure show results for  $M_N$  greater than 1.0. For high values of  $M_N$  and low-lift (near zero angle-of-attack) conditions, the value of the cross-flow velocity is low, thus subcritical with the primary flow in the streamwise direction. As lift increases, the flow turning angle about the leading edge increases resulting in an increase in the magnitude of the inboard flow component. This inboard flow will eventually recompress and turn streamwise. As lift increases further, the cross-flow velocity will increase to the point that a "cross-flow" shock will occur that will turn the flow streamwise. The occurrence of a cross-flow shock is an indication of the existence of nonlinear supercritical-type cross flow. Further increases in lift result in shock-induced separation of the boundary layer and the formation of a smooth-wall separation (bubble or vortex). Further increases in angle of attack will show the shock-induced bubble/vortex migrating to the leading edge. With further increases in angle-of-attack this smooth-wall bubble/vortex structure will transform into a sharp-edge vortex as the feed sheet emanates from the sharp leading edge. This structure will eventually lift off the surface and cross-flow shocks will form. These shocks may be located on the vortex upper surface, underneath the vortex, and horizontally between the two counter-rotating pair of vortex structures. The vortex structure, which lies underneath the primary vortex structure, will interact with the boundary layer and result in a smooth-wall vortex (secondary) structure.

The left side of figure 48 show results for  $M_N$  less than 1.0. For low values of  $M_N$  and low-lift (small angle-of-attack) conditions the flow that occurs on the lee side of a wing is a leading-edge separation characterized by a viscous, rotational mass of air that resides inboard of the wing leading edge. At low-lift conditions, a leading-edge bubble will develop. This bubble will lift off the wing surface and become a vortex with increasing angle of attack. As angle of attack is increased further, a secondary vortex and then a vortex with a shock will occur. The vortex body is connected to the wing surface via the feed sheet that is a viscous flow region that emanates from the wing boundary layer near the wing leading edge. The shape and position of the viscous vortex system are dependent upon the flowfield external to the vortex that interacts with the vortex system until an equilibrium condition is established. The vortex system acts as a physical boundary to the external flowfield. The free-stream flow expands around the wing leading edge and follows

the contour of the vortex system undergoing an expansion followed by a compression as the flow turns about the vortex. This "induced flowfield", that is influenced by the viscous vortex system, and is characterized by a stagnation point or reattachment line on the wing upper surface inboard of the vortex body. Inboard of this induced flowfield is the potential flowfield, where the flow is attached in the streamwise direction.

Example vapor screen photographs for several of the types of complex vortex flow structures depicted in figure 48 will be discussed next. The specific  $M_N$  and  $\alpha_N$  conditions for these data points are graphically depicted in figure 49 and the associated data for each of the conditions will be presented in figures 50 and 51. Figure 50 contains a series of vapor screen photographs on the zero-thickness, 75°-delta wing model in the NASA LaRC UPWT<sup>112</sup>. The images in this figure represent conditions that are above and below  $M_N = 1.0$ , as depicted in figure 49. Three angles of attack are shown for Mach numbers 2.4, 3.4, and 4.6, see figures 50a, 50b, and 50c respectively. A review of the data of figure 50 show: a primary vortex only for the Mach 2.4,  $\alpha = 8^\circ$  and Mach 3.4,  $\alpha = 8^\circ$  conditions. At Mach 4.6 and  $\alpha = 8^\circ$  the data show the existence of a separation bubble with shock. The existence of primary vortex with shock, secondary vortex, and tertiary vortex structures are observed for Mach 2.4 and 3.4 at  $\alpha = 16^\circ$  and  $24^\circ$ . At Mach 4.6 and  $\alpha = 16^\circ$  and  $24^\circ$  separation bubbles with shock that extend to the centerline of the model are observed. Note that with the exception of Mach 2.4,  $\alpha = 8^\circ$  and Mach 3.4,  $\alpha = 8^\circ$  each of these images contain at least one cross-flow shock and for most of the images several cross flow shock structures are present.

Figure 51 presents a series of vapor screen photographs for a zero-thickness, 52.5°-delta wing model in the NASA LaRC UPWT<sup>112</sup>. The images in this figure represent conditions that are above  $M_N = 1.0$ , as depicted in figure 49. Three angles of attack are shown for Mach numbers 2.4, 3.4, and 4.6, see figures 51a, 51b, and 51c respectively. The vapor screen photographs of figure 51 show the existence of both smooth-wall separations (i.e. shock/boundary-layer interaction) and sharp-edge separations. With the exception of the image for Mach 2.4 and  $\alpha = 8^\circ$  the data show the existence of leading-edge separation bubbles and/or vortices. These vortex structures are seen to increase in size and spanwise extent toward the centerline of the model, with increases in angle-of-attack and Mach number. Note that each of the flow fields shown contain at least one cross-flow shock structure and for most of the images several cross flow shock structures are present.

### 5.2.2.2 Thick Wings

The effect of wing thickness on the wing leading-edge vortex position is shown in figure 52<sup>182</sup>. The vortex action line shown in figure 52 is represented as a fraction of the local wing semispan. The vortex action line is the position at which the vortex-induced normal-force vector should be placed to give the same wing bending moment as that produced by the vortex pressure loading on the wing upper surface. The data clearly show an outboard movement of the vortex with increasing the wing local surface slope at the leading-edge. The thick-wing surface pressure data of figure 53<sup>182</sup> also indicates that the wing leading-edge surface slope acts to delay the onset of flow separation to a higher angle of attack. At a constant angle of attack of  $8^\circ$ , the data of figure 52 and 53 show that increasing leading-edge surface slope results in a weaker vortex that is located further outboard as compared to a lower leading-edge surface slope. The data indicate that wing leading-edge surface slope and not thickness is the dominant mechanism that controls vortex formation, strength, and position. Despite the noticeable effects on the lee-side flow characteristics between the three wings, a review of additional data contained in reference 182 show that there were no noticeable changes on the total wing lifting characteristics.

A review of thick-delta-wing lifting characteristics of figure 47, show that for values of  $\beta \cot \Lambda$  below 0.5, the lift-curve-slope data show insensitivity to thickness. The figure also shows that for values of  $\beta \cot \Lambda$  above 0.5 there is an increase in the lift-curve-slope over the flat, zero-thick delta data but only a minor variation due to large changes in thickness. The data of figure 47 also indicate that the leading-edge radius affects the flow and resultant vortex formation the same as the leading-edge angle or thickness.

Figure 54<sup>138</sup> show oilflow photographs on the lee side of three 60°-delta wing models. The first is flat-topped (zero-thick) wing, the second has a circular arc airfoil, and the third has a diamond airfoil. At  $0^\circ$  angle of attack, all three wings have attached flow. At  $8^\circ$  angle of attack the circular arc and diamond airfoils have attached flow on the upper surface and the flat wing has a sharp-edge vortex separation. For the thick wings there is a cross-flow component that flows inboard and normal to the leading-edge sweep. Inboard of the leading edge the cross-flow is recompressed and turns streamwise. At  $16^\circ$ , all three wings have leading-edge separation (sharp-edge vortex). The location of the vortex action line for the flat wing occurs further inboard than for the two thick wings, as was observed previously in figure 51.

Figure 55<sup>138</sup> illustrates the effect leading-edge sweep and airfoil shape has on the lee-side flow characteristics on delta wings at  $M = 1.70$  and  $8^\circ$  angle-of-attack. The six images on this figure include three  $52.5^\circ$  delta wing models and three  $75^\circ$  delta wing models, top and bottom rows, respectively. The figure also has three columns comparing a flat, a circular arc, and a diamond airfoil model (as was done in figure 54). Once again, it is clearly evident that the flat wings have their vortex action lines occurring further inboard than the "thicker" circular arc and diamond airfoil wings.

Finally, even at  $0^\circ$  angle of attack, a thick wing can have vortex flow. For example, figure 56 is an oil flow photograph of a  $75^\circ$ -delta with a diamond airfoil. The oil flow shows that the leading edge is attached, however, the flow downstream of the maximum thickness line has separated and has an oil flow pattern that is similar to the oil flow photos seen for flat wings at angle of attack. Upon an initial review it is unclear if this separation is of the sharp-edge or smooth-wall type. However a review of the predicted surface pressure coefficient plots shown at three  $x/l$  locations (.6, .8, and .95) indicate that the flow expands over the ridge, then recompresses through a cross flow shock. These pressure data clearly indicate that the separation mechanism is a smooth-wall type. The flow direction inboard of the shock is streamwise. This effect will also be seen in the next section when investigating the effects of camber.

### 5.2.2.3 Cambered Wings

After wing planform selection the geometric parameter that is usually optimized, during design of a supersonic aircraft, is the camber and twist distribution. The next series of figures will illustrate the effect of a camber (leading-edge flap deflection) on the flow characteristics on the upper surface of a highly-swept, sharp leading edge delta wing at supersonic speeds. All of the data presented in this section were obtained on a  $75^\circ$ -delta wing with deflectable leading-edge flaps. Photographs of the wind tunnel model installed in the NASA LaRC UPWT are shown in figure 57<sup>110</sup>. The data obtained for this model are presented in figures 58 - 60. The data of figures 58 and 59 represent the two families of flow types found in the investigation documented in reference 110. The first family of data is termed "single feature" flow type and is presented in figure 58. The second family of data is the "double feature" flow type, see figure 59.

Figure 58<sup>110</sup> shows six sets of vapor screen images, surface pressure coefficient values, and flowfield sketches of the  $75^\circ$ -swept delta wings at various Mach

numbers and angles of attack with a single flow feature. The data will be discussed from left to right and top to bottom starting with the upper left figure. The effect of camber is modeled as a leading-edge flap deflection. The first image in figure 58 is for a  $5^\circ$  leading-edge flap,  $\delta_l$ , setting at  $M = 1.7$  and  $\alpha = 0^\circ$ . The data shows attached flow (i.e., no dark regions evident in the vapor screen photograph and only a small negative pressure coefficient,  $C_p$ , located at the hinge line). The second image presented is for a change in  $\alpha$  only to  $6^\circ$ . The data shows a leading-edge bubble (i.e., a small dark region at the leading edge on the flap and a large region of negative  $C_p$  values that encompass the flap). The third image presented is for another change in  $\alpha$  only to  $12^\circ$ . This data indicates the existence of a classical vortex with a feed sheet, secondary separation (bubble) and a shock located between the wing upper surface and the leading-edge vortex. The corresponding pressure distribution show that low pressures persist well inboard of the flap hinge-line. The fourth image was taken for the same wing geometry but at a Mach number of 2.0 and an  $\alpha$  of  $16^\circ$ . This data show a leading-edge vortex, a cross-flow shock (on top of the vortex), a secondary vortex on the hinge line, and a shock underneath the primary leading edge vortex. The fifth image was obtained for a  $10^\circ$  leading edge flap deflection angle at  $M = 2.8$  and  $\alpha = 0^\circ$ . The data show the existence of a hinge-line separation bubble (i.e., a small dark region on the wing inboard of the hinge line). The final image in this figure is a hinge-line vortex and was taken at  $M = 2.4$  at an  $\alpha$  of  $6^\circ$  for a  $10^\circ$  leading edge flap deflection angle. The vapor screen photo indicates the hinge-line vortex by a circular dark region about halfway from the centerline to the hinge line. There is also evidence of a feed sheet on the photo. The surface pressures indicate suction pressures inboard of the hinge line with negligible loads on the flap.

Figure 59<sup>110</sup> show six sets of double-feature flow types observed on the same  $75^\circ$ -delta wing model. The first image is for a  $5^\circ$  leading-edge flap deflection at  $M_\infty = 1.7$  and  $\alpha = 5^\circ$  and shows two separation bubbles, one located at the leading edge on the flap and the other at the hinge line. The surface  $C_p$  values show that the bubble located on the flap produces much lower values of  $C_p$  than the one at the hinge line. By increasing the flap angle to  $10^\circ$ , the Mach number to 2.4, and the angle of attack to  $8^\circ$ , the second image indicates that the hinge-line bubble has lifted off the surface to become a vortex. The third image provides roughly the same pressure loading on the upper surface, however, there exists a separation bubble at the leading edge with a cross flow shock lying on top of it followed by a hinge-line separation bubble. This occurred at a Mach

number of 2.8, an  $\alpha$  of  $6^\circ$ , with a  $\delta_f$  of  $5^\circ$ . The fourth image has higher pressure loading due to the fact that the hinge-line separation bubble has been replaced with a vortex. In this case, the  $\delta_f$  was set at  $10^\circ$ , the angle of attack was  $10^\circ$ , and the Mach number was 2.4. The fifth and sixth images were taken at a Mach number of 2.8. The first was at  $12^\circ$   $\alpha$  with  $\delta_f = 10^\circ$ . A lambda shock is quite evident on the flap followed by a strong hinge-line vortex. The last image has a shock located on the outboard flap followed again by a strong hinge-line vortex with shock. This occurred at an  $\alpha$  of  $16^\circ$  with a  $\delta_f$  of  $15^\circ$ .

It is clear from the data, that unlike the effect of thickness or leading-edge radius, the effect of camber does not provide a uniform progression in the location of the vortex or the strength of the vortex. However, once flow separation occurs at the wing leading edge ( $\alpha > 10^\circ$ ), the flow behaves similarly to that for thin flat wings. Increasing wing camber (i.e.,  $\delta_f$  deflection) delays the formation of a wing leading-edge vortex. Figure 60 is a map of the lee-side flow type for variations in flap deflection angle and angle of attack. The data show that five distinct flow types exist on the lee side of these cambered delta wings at supersonic speeds. The data of figure 60 also show that there are both low-lift and high-lift ( $\alpha$  varies between  $0^\circ$  and  $8^\circ$ ) conditions in which a vortex resides on a deflected leading edge flap at supersonic speeds. These data clearly suggest that improved aerodynamic performance is available for wings with vortex flow.

Despite the differences in the vortex flow structure over the upper surface of flat and cambered wings, the lift-curve slopes are very similar (reference 182). This fact clearly suggests a similarity in upper surface loading. It is suggested that a designer may take the similarity in loading into account to develop a wing upper surface that will efficiently use this loading to create improved performance across the lift range.

## 6.0 WING DESIGN

In the previous sections of this paper a variety of vortex-flow structures have been shown to exist on a wide variety of vehicles and simple shapes. And in the previous section entitled "Designed Vortex Structures" data has been shown which indicate that significant aerodynamic performance improvements are available by considering vortex flows as a primary design feature. This final section of the paper will briefly discuss the idea of designing wings that utilize vortex flows for improved aerodynamic performance at supersonic speeds.

### 6.1 Design Philosophy

Until the mid 1990's most supersonic wing design activities utilized linear-theory design methods. However, it has only been in the last few years that the trend has been to use Euler and Navier Stokes methods for design. These methods are typically coupled to numerical optimization techniques and use highly constrained models to modify the geometry in the design process. Even though the design community is moving to the routine use of more advanced computational methods, the philosophy and understanding behind the design approach is primarily founded in "linear" thinking. Designs of supersonic aircraft continue to employ traditional linear-theory rules for planform, airfoil selection, camber shapes and the integration of aircraft components (i.e. wing, body, tails, and nacelles). The location of maximum airfoil thickness (typically located at 40 to 50 percent chord) and the choice of sharp leading edges (especially when the leading-edge sweep implies a supersonic leading-edge condition) continue to be zeroth- or first-order design guidelines.

It is critical that non-physical constraints or limitation of theory or tools not restrict the design of a vehicle. Aerodynamic design must be based upon physical observation and knowledge. A possible philosophy for design is that postulated by Kucheman<sup>1</sup>:

*"flow fields suitable for efficient aerodynamic design must be steady, stable and controllable, changing quantitatively with changes in attitude and Mach number while remaining qualitatively of the same type throughout the whole flight range".*

In review of this philosophy it is clear that vortex flow design easily satisfies the criteria. However the authors prefer not to be bound by a single flow type in the design process. Perhaps a natural extension to the Kucheman philosophy is;

*"the induced aerodynamics of a flow field suitable for efficient aerodynamic design must be steady, stable and controllable, changing quantitatively with changes in attitude and Mach number while remaining qualitatively of the same type throughout the whole flight range".*

It is this philosophy upon which the following discussion is based.

## 6.2 Design Observations

The supersonic aerodynamics of a sharp leading edge swept wing dominated by vortex flow is nearly identical to that for a blunt leading edge wing with fully attached flow, for the same Mach and angle of attack<sup>183</sup>. In a similar fashion, the transonic and subsonic aerodynamics of thin swept wings are also fairly insensitive to small geometric variations, such as wing leading-edge shape. These observations allow the designer to configure the geometric details of a wing based upon the loading and not the specific flow field.

To design a wing for multiple design conditions (other than zero lift), it has been found that higher performance (lower drag and higher lift) can be achieved by adding bluntness/thickness to the wing leading edge and varying the maximum airfoil thickness location between 20 and 60 percent chord (Ref. 183).

In figure 61, several useful (linear-theory based) design boundaries are outlined. The curves of interest to most designers are the linear theory 0% leading-edge thrust curve and the linear theory 100% leading-edge thrust curves. For zero-thickness, flat wings, 0% leading-edge thrust defines the linear theory predicted drag performance of a wing with attached flow conditions. However, it is well known that for a thin, sharp, leading-edge swept wing at angle of attack the flow will separate at the leading edge and form a vortex. The resulting performance level for this case is defined as 100% Vortex Lift. This curve does accurately represent the performance level that is achieved by a thin uncambered (zero-thickness, flat) wing designed to utilize the leading-edge vortex. The third linear theory based curve depicted in figure 61 is the 100% leading-edge thrust curve. This curve is the linear-theory "best" design. This curve also assumes an unachievable level of attached flow at the wing leading edge. Note, it is this curve that existing designs are measured against.

Also shown on figure 61 is a "new" boundary, defined as the Nonlinear Viscous Performance Boundary. This boundary has been defined through a review and analysis of existing experimental data<sup>182, 183</sup>. This boundary allows for the existence of leading-edge thrust and/or vortex lift on the wing to achieve improved performance at all design points. A more detailed discussion of this curve is provided in reference 183 in which the Natural Flow Wing design philosophy is presented. This design concept utilizes the naturally occurring flow over a wing and shapes the underlying surface contours to take advantage of the surface pressures generated by those flow structures.

## 6.3 Design Approach

Figure 62 illustrates how the NFW approach can be applied to delta wings. A typical wing design will choose a maximum airfoil thickness location and apply this to the entire wing. This results in a wing that has a geometry that is conical about the wing tip (solid line on left-hand-side of figure). However, as was seen in the previous sections of this paper, the flowfield on the lee side of highly swept wings is actually conical about the apex of the wing. That is, the flow over a wing at moderate to high lift conditions may be characterized by an expansion over the leading edge that is followed by a recompression to a more positive pressure as the flow moves inboard and aft. This recompression line lies along a ray that emanates from the wing apex. The shaded regions on the figure indicate the low (expanded flow) pressure regions on the wing. If one would apply the surface pressures to the surface geometry, one can resolve a lift and drag component. Thus, four regions of Drag can be obtained. Forward of the maximum thickness line, the surface has a forward-facing slope. Near the leading edge where the flow is expanding, the pressures are low, thus, a low pressure acting on a forward-facing slope would provide a "thrust" or low drag. Therefore, region B in the figure would be a low drag region. However, Region A, where the flow has recompressed to higher pressures, would be a high drag region because high pressures acting on a forward-facing slope will generate a positive drag value. Aft of the maximum thickness line, the slope of the surface is aft-facing. Thus, near the leading edge, in the expanded flow region, the drag would again be high because low pressures acting on an aft-facing surface will produce positive drag values. And finally, in regions where the flow has recompressed and the slopes are aft-facing, one would expect to obtain low drag or thrust because a high pressure acting on an aft-facing surface would generate low positive or even negative values of drag (i.e., thrust). Thus, a goal of the designer would be to reduce the sizes of regions A and C and maximize the size of regions B and D. On the right side of figure 62 is a drawing of the Natural Flow airfoil maximum thickness line. The maximum thickness location approaches the apex and actually would fall downstream of the trailing edge at the tip (see figure 63). With this approach, one would reduce the size of region A and completely eliminate region C.

## 6.4 Design Results

This approach was applied to a 65°-swept delta wing<sup>183</sup> and the resulting geometries that were tested in the NASA LaRC UPWT are shown in figure 64. It should be noted that the Natural Flow wing is sharp and thin inboard becoming thicker with a blunt leading edge

outboard. It was noted in previous sections that a thin, sharp leading-edge moved the vortex action line more inboard compared to a wing with increased bluntness or thickness. However, the more blunt the leading edge provided for more attached flow and also leading-edge thrust. The sharp leading edge at the apex and the thin airfoil section at the centerline of the NFW design allows the vortex to set up stronger and maintaining the strength of the vortex as if it were a wing that was sharp to the tip. The added bluntness and thickness outboard provides additional surface area and improved surface slopes to reduce drag. Figure 65 shows oil flow photos of the three wings tested in the study. It should be noted that the NFW wing had an oil accumulation line that ran parallel with the leading edge. This coincides with the location of the airfoil maximum thickness location. The predicted and experimentally determined performance agreed very well and is shown in figure 66. The NFW design philosophy has recently been utilized in several advanced concepts including the now defunct national High-Speed Research (HSR) program<sup>2</sup>.

## **7.0 CONCLUDING REMARKS**

An overview of the high-speed vortex flow experimental research conducted at the National Aeronautics and Space Administration (NASA), Langley Research Center (LaRC) during the 1970s, 1980s, and 1990s has been presented. Data has been shown for flat plates, cavities, bodies, missiles, wings, and aircraft for a Mach number range of 1.3 to 4.6. These data are presented and discussed in the context of the design of future vehicles. In order to provide perspective of these research results a brief historical review of the extensive body of high-speed vortex flow research from the 1940s has also been presented.

Data presented show that a wide variety of sharp-edge and smooth-wall resultant vortex structures occur on all vehicles at supersonic speeds. The data also show the presence of both small- and large-scale vortex structures for a variety of vehicles from missiles to transports. These vortex structures have historically been viewed as unfavorable flow features. In an effort to evaluate this viewpoint the subject data has been analyzed to determine the impact of these various flow structures to vehicle performance and control. The preliminary analysis of these data indicated that these vortex structures are not detrimental and in fact have the potential to provide very significant positive-interference benefits. The data for the resultant vortex structures indicated that all of the flows are steady, stable and controllable, changing quantitatively with changes in attitude and Mach number while remaining qualitatively of the same type.

For cavities, the data show complex multiple-vortex structures at all combinations of cavity depth-to-length ratios and Mach number. The data showed that the cavity flow-fields, vortex structures and resultant aerodynamics are steady, stable and remained qualitatively similar with changes in Mach number for both open and closed cavity flow.

The data presented have shown that missiles at high angles of attack can have multiple sets of counter rotating vortex structures which flow aft over the vehicle and interact with the down-stream control surfaces. For missiles in roll the complexity of the vortex dominated flow fields and resulting interference patterns increases dramatically. Data has been shown that demonstrates the capability of these interference effects to influence vehicle flight performance. Analysis presented indicates that significant improvements in the flight characteristics can be achieved through the management of these interference effects. The data also showed that these vortex dominated flow-fields are controllable.

For wings and aircraft, data are shown which highlight the effect that leading-edge sweep, leading-edge bluntness, wing thickness, location of maximum thickness, and camber has on vortex formation and the resultant aerodynamics. The data presented for the lee-side flow fields for delta wings showed that the vortex flow structures develop in a logical and continuous fashion with changes in wing geometry Mach number and angle of attack. Wing and wing/body aerodynamic data and flow field have been shown that indicate that aerodynamic performance improvements are available by considering vortex flows as a primary design feature.

Finally a design approach for wings/aircraft, which utilize vortex flows, for improved aerodynamic performance at supersonic speeds was presented and discussed. The subject design approach uses the observation that the loading on thin, swept wings at supersonic speeds is minimally affected by the lee-side flow field characteristics. Data is presented that show the performance of a wing, with a lee-side vortex, produced with this design approach exceeds that which may be achieved by traditional design methods.

This paper has provided a brief overview of the high-speed vortex flow research at NASA LaRC in the hope of stimulating the aerodynamic community to investigate the potential of vortex flows to improve the aerodynamic performance and control of future aircraft.

## **8.0 ACKNOWLEDGEMENT**

The authors would like to thank Mr. Peter Covell and Dr. James Campbell of NASA LaRC for their contributions of photographic material used in this paper. Their assistance is greatly appreciated and is respectfully acknowledged.

The authors would also like to thank the research and technical staff assigned to and those who supported the research conducted at the NASA LaRC UPWT from 1970 to 1990. Their professionalism and support is greatly appreciated and is respectfully acknowledged.

## **9.0 REFERENCES**

1. Kucheman, D.: The Aerodynamic Design of Aircraft. Pergamon Press. 1978.
2. First NASA / Industry High-Speed Research Configuration Aerodynamics Workshop. R. M. Wood ed. NASA / CP-1999-209690/PT1. Dec 1999.
3. Barret, C.: Lifting Body Stability and Control. NASA TM-1999-209255. March 1999.
4. Jones, R. T.: Estimated Lift-Drag Ratios at Supersonic Speed. NACA TN 1350. July 1947.
5. Jones, R. T.: Effects of Sweep-Back on Boundary Layer and Separation. NACA Report No. 884. 1947.
6. Riebe, J. M. and Fikes, J. E.: Preliminary Aerodynamic Investigation of the Effect of Camber on a 60° Delta Wing with Round and Beveled Leading Edges. NACA RM L9F10. Aug. 1949.
7. Vincenti, W. G.: Comparison Between Theory and Experiment for Wings at Supersonic Speeds. NACA Report 1033. 1949.
8. Lee, G. H.: Note on the Flow Around Delta Wings with Sharp Leading Edges. A.R.C. R&M No. 3070, 1955.
9. Love, E. S.: Investigations at Supersonic Speeds of 22 Triangular Wings Representing Two Airfoil Sections for Each of 11 Apex Angles. NACA Report 1238. 1955.
10. Michael, W. H. Jr.: Flow Studies on Drooped-Leading-Edge Delta Wings at Supersonic Speed. NACA TN 3614. Jan. 1956.
11. Michael, W. H. Jr.: Flow Studies on Flat Plate Delta Wings at Supersonic Speed. NACA TN 3472. July 1955.
12. Brown, C. E. and Michael, W. H. Jr.: On Slender Delta Wings with Leading Edge Separation. NACA TN 3430. April 1955.
13. Boatright, W. B.: Experimental Study and Analysis of Loading and Pressure Distributions on Delta Wings Due to Thickness and to Angle of Attack at Supersonic Speeds. NACA RM L56I14. Dec. 1956.
14. Sacks, A. H.: Vortex Interference Effects on the Aerodynamics of Slender Airplanes and Missiles. Jour. Of Aero. Sci. Vol. 24, No. 6. June 1957.
15. Smith, F. M.: Experimental and Theoretical Aerodynamic Characteristics of Two Low-Aspect-Ratio Delta Wings at Angles of Attack to 50° at a Mach Number of 4.07. NACA RM L57E02. July 1957.
16. Nielsen, J. N.: The Effects of Body Vortices and the Wing Shock-Expansion Field on the Pitch-Up Characteristics of Supersonic Airplanes. NACA RM A57L23. March 1958.
17. Boatright, W. B.: An Analysis of Pressure Studies and Experimental and Theoretical Downwash and Sidewash Behind Five Pointed-Tip Wings at Supersonic Speeds. NACA Report 1380. 1958.
18. Chapman, D. R., Kuehn, D. M., and Larson, H. K.: Investigation of Separated Flows in Supersonic and Subsonic Streams with Emphasis on the Effect of Transition. NACA Report 1356. 1958.
19. Mueller, J. N. and Grimaud, J. E.: Effects of Twist and Camber and Thickness on the Aerodynamic Characteristics of a 75° Swept Arrow Wing at a Mach Number of 2.91. NACA TM X-138. Dec. 1959.
20. Hall, I. M. and Rogers, E. W. W.: The Flow Patterns on a Tapered Sweptback Wing at Mach Numbers Between 0.6 and 1.6. ARC R&M 3271, Part 1, July 1960.
21. Allen, H. J. and Perkins, E. W.: A Study of the Effects of Viscosity on Flow Over Slender Inclined Bodies of Revolution. NACA Rep. 1048, 1951.

22. Boyd, V. W. and Phelps, E. R.: A Comparison of Experimental and Theoretical Loading Over Triangular Wings at Supersonic Speeds. NACA TIB 2591. Jan. 1951.
23. Hatch, V. E. and Hargrave, L. E.: Effects of Reynolds Number on the Aerodynamic Characteristics of a Delta Wing at Mach Number 2.41. NACA TIB 2919. Oct. 1951.
24. Maskell, E. C.: Flow Separation in Three - Dimensions. RAE Aero Report 1565. Nov. 1955.
25. Maskell, E. C. and Kucheman, D.: Controlled Separation in Aerodynamic Design. RAE TM 463. Mar. 1956.
26. Maskell, E. C. and Weber, J.: On the Aerodynamic Design of Swept Wings. Jour. of Royal Aero. Soc., Vol. 63, Dec. 1959, pp. 709-721.
27. Rogers, E. W. E. and Berry, C. J.: Experiments at  $M = 1.41$  on Elliptic Cones with Subsonic Leading Edges. R&M 3042. Oct. 1952.
28. Stewart, H. J.: The Lift of a Delta Wing at Supersonic Speeds.
29. Stollery, J. and Ellis, D.: Leading Edge Vortex Flaps on Delta Wings.
30. Harris, R. V. Jr.: On the Threshold - Outlook for Supersonic and Hypersonic Aircraft. AIAA 89-2071. Aug 1989.
31. Reed, R. D.: Wingless Flight: The Lifting Body Story. NASA SP-4220. 1997.
32. Lamar, J. E. and Campbell, J. F.: Recent Studies at NASA-Langley of Vortical Flows Interacting with Neighboring Surfaces. AGARD Fluid Dyn. Panel Sym. on Vortical Type Flows in Three Dimensions. April 1983.
33. Campbell, J. F. and Chambers, J. R.: Patterns in the Sky - Natural Visualization of Aircraft Flow Fields. NASA SP-514.1994.
34. Ogawa, A.: Vortex Flow. CRC.
35. High Angle-of-Attack Aerodynamics. AGARD LS-121. March 1982.
36. Rom, J.: High Angle of Attack Aerodynamics - Subsonic, Transonic, and Supersonic Flows. 1991.
37. Stanbrook, A.: Experimental Observation of Vortices in Wing-Body Junctions. ARC TR R&M No. 3114. 1959.
38. Stanbrook, A. and Squire, L. C.: Possible Types of Flow at Swept Leading Edges. Aero. Quarterly, Vol. 15, pp. 72-82, 1960.
39. Stanbrook, A. and Squire, L. C.: Possible Types of Flow at Swept Leading Edges. Aero. Quart. Vol. XV, pt. 1, Feb 1964, pp. 72-82.
40. Kucheman, D.: Aircraft Shapes and Theoretical Aerodynamics for Flight at Supersonic Speeds. Von Karman., Adv.in Aero. Sci., Proc. of the Second Int. Congress in the Aero. Sciences, Zurich 12-16 September 1960. Volume 3. 1962. pp. 221-252.
41. Kucheman, D.: On the Possibilities of Designing Wings that Combine Vortex Flows with Classical Aerofoil Flows. RAE Tec. Memo Aero. 1363. Oct. 1971.
42. Kucheman, D. and Weber, J.: Vortex Motions. ZAMM, Vol. 7, No. 8, pp. 457-474, 1965.
43. Von Karman, T, Ballantyne, A. M., Dexter, R. R., Bock, G., Dryden, H. L., and Roy, M.: Advances in Aeronautical Sciences, Proceedings of the Second International Congress in the Aeronautical Sciences, Zurich 12-16 September 1960. Volume 3. 1962.
44. Squire, L. C.: Camber Effects on the Non-Linear Lift of Slender Wings with Sharp Leading Edges. ARC C.P. No. 924. 1967.
45. Squire, L. C. ; Flow Regimes Over Delta Wings at Supersonic and Hypersonic Speeds. Aero. Quarterly, Vol. XXVII, P. 1, Feb. 1976.
46. Squire, L. C.: Pressure Distributions and Flow Patterns on Some Conical Shapes with Sharp Edges and Symmetrical Cross- Sections at  $M = 4.0$ . ARC R&M No. 3340, 1963.
47. Squire, L. C., Jones, J. G., and Stanbrook, A.: An Experimental Investigation of the Characteristics of Some Plane and Cambered  $65^\circ$  Delta Wings at Mach Numbers from 0.7 to 2.0. ARC R&M No. 3305. 1963.
48. Peake, D. J. and Tobak, M.: Three-Dimensional Flows About Simple Components at Angle of Attack. Paper No. 2 AGARD Lecture Series No. 121 on High Angle-of -Attack Aerodynamics. March 1982.
49. Peake, D. J. and Tobak, M.: Three-Dimensional Interactions and Vortical Flows With Emphasis on High Speeds. NASA TM 81169. March 1980.

50. Tobak, M. and Peake, D. J.: Topology of Three-Dimensional Separated Flows. *Ann. Rev. Fluid. Mech.* Vol. 14, 1982, pp. 61-85.
51. Bannink, W. J. and Nebbeling, C.: Investigation of the Expansion Side of a Delta Wing at Supersonic Speeds. *AIAA Journal* Vol. 11, No. 8, August 1973.
52. Bashkin, V. A.: Experimental Study of Flow About Flat Delta Wings at  $M = 5$  and Angles of Attack from 0 to 70°. *Izvestiya Akademiiia Nauk SSSR Mekhanika Zhidkosti I Gaza*, Vol. 23, pp. 102-108, 1967.
53. Brown, C. E., McLean, F. E., and Klunker, E. B.: Theoretical and Experimental Studies of Cambered and Twisted Wings Optimized for Flight at Supersonic Speeds. *Von Karman, Adv. in Aero. Sci., Proc. of the Second Int. Congress in the Aero. Sci., Zurich 12-16 September 1960. Volume 3. 1962. pp. 415-431.*
54. Carafoli, E.: *Wing Theory in Supersonic Flow.* Pergamon Press Int. Series of Monographs in Aero. And Astro. Vol. 7. 1969.
55. Cleary, J. W.: Lee-Side Flow Phenomena on Space Shuttle Configurations at Hypersonic Speeds: Part I Flow Separation and Flow Field Viscous Phenomena of a Delta-Wing Shuttle Orbiter Configuration. *NASA TM-X-2507/L-8136-Vol. 2.* Feb. 1972.
56. Cross, E. J. and Hankey, W. L.: Investigation of the Leeward Side of a Delta Wing at Hypersonic Speeds. *Jour. Of Scrft and Rockets*, Vol. 6, No. 2, pp. 185-190, Feb. 1969.
57. Danavant, J. C., Narayan, K. Y., and Walberg, G. D.: A Survey of Leeward Flow and Heat Transfer on Delta Planform Configurations. *AIAA Paper 76-118.* 1976.
58. Degani, D. and Schiff, L. B.: Computation of Supersonic Viscous Flows Around Pointed Bodies at Large Incidence. *AIAA Paper 83-0034.* Jan. 1983.
59. Delery, J. M.: Physics of Vortical Flows. *Journal of Aircraft* Vol. 29, No. 5, Sept.-Oct. 1992.
60. Delery, J., Horowitz, E., Leuchter, O., and Solignac, J. L.: Fundamental Studies on Vortex Flows. *Rech. Aerosp.* 1984.
61. Fellows, K. A. and Carter, E. C.: Results and Analysis of Pressure Measurements on Two Isolated Slender Wings and Slender Wing-Body Combinations at Supersonic Speeds, Part 1 - Analysis. *ARC C.P. No. 1131.* 1970.
62. Fournier, R. H. and Spencer, B. Jr.: Aerodynamic Characteristics at Mach Numbers from 1.50 to 4.63 of a Variable-Geometry Lifting Reentry Concept Employing Elevator and Body Base Flaps for Control. *NASA TM X-1351.* April 1967.
63. Ganzer, U., Hoder, H., and Szodruch, J.: On the Aerodynamics of Hypersonic Cruise Vehicles at Off-Design Conditions. *ICAS Proceedings - 1978, Vol I - Fuel Conservation, Hyp. Veh., Environ. Effects, Materials and Struc., Comp. Aero., Wind Tunnels, Flight Testing, Stability and Control.* J. Singer and R. Staufenbiel, eds. 1978, pp. 152-161.
64. Goodsell, A. M. and Melton, J. E.: Transonic and Supersonic Euler Computations of Vortex Dominated Flow Fields About a Generic Fighter. *NASA TP 3156.* November 1991.
65. Gunko, I. U. P. and Mazhul, I. I.: Investigation of the Regimes of Flow Past the Upper Surface of Delta Wings with Shock Waves Separated from the Leading Edges. *Akademiia Nauk SSSR.* Feb. 1979.
66. Hefner, J. N.: Lee-Surface Heating and Flow Phenomena on Space Shuttle Orbiters at Large Angles of Attack and Hypersonic Speeds. *NASA TN D-7088.* Nov. 1972.
67. Hemsch, M. J.: Semi-Emperical Methods for Conventional and Unconventional Missiles. *AGRAD Rpt. No. 754.* 1988.
68. Larsson, P. O.: A Note on Supersonic and Transonic Flow Around Delta Wings. *CN-154394.*
69. Linde, M.: The Flow on the Lee-Side of a Delta Wing at Mach 7. *The Second Joint Europe/US Short Course in Hypersonics.* Jan. 1989.
70. McRae, D. S., Peake, D. J., and Fisher, D. F.: A Computational and Experimental Study of High Reynolds Number Viscous/Inviscid Interaction About a Cone at High Angle of Attack. *AIAA-80-1422.* July 1980.

71. Morris, O. A.: Aerodynamic Characteristics in Pitch at a Mach Number of 2.01 of Several Wing-Body Combinations with Wedge-Shaped Bodies Located Above and Below a 54.5° Swept Delta Wing. NASA TN D-1823. June 1963.
72. Murman, E. M., Powell, K. G., Miller, D. S., and Wood, R. M.: Comparison of Computations and Experimental Data for Leading-Edge Vortices - Effects of Yaw and Vortex Flaps. AIAA - 86-0439. January 1986.
73. Narayan, K. Y. and Hartman, K.: Transonic and Supersonic Flow Past a 65° Delta Wing with Round Leading Edges - Analysis of Experimental Data. DFVLR-FB 88-44. Oct. 1988.
74. Narayan, K. Y.: Lee-Side Flowfield and Heat Transfer of a Delta Wing at  $M = 10.0$ . AIAA Journal, Vol. 16, No. 2, p. 160, 1978.
75. Nastase, A.: Some Considerations on Leading-Edge Vortices on Wings in Supersonic Flow. Fluid Dynamic Research 3 (1988) 387-391. 1988.
76. Newsome, R. W. and Kandil, O. A.: Vortical Flow Aerodynamics-Physical Aspects and Numerical Simulation. AIAA Paper No. 87-0205. January 1987.
77. Newsome, R. W. and Thomas, J. L.: Computation of Leading-Edge Vortex Flows. NASA Vortex Flow Aerodynamics Conference. October 1985.
78. Oberkampf, W. L. and Bartel, T. J.: Supersonic Flow Measurements in the Body Vortex Wake of an Ogive Nose Cylinder. AIAA Paper No. 78-787. April 1978.
79. Pagan, D. and Molton, P.: Basic Experiment on a Supersonic Vortex Flow Around a Missile Body. AIAA Paper No. 91-0287. January 1991.
80. Pavinelli, L. A. and Pavinelli, F. P.: Vortex Enhancement of Jet Penetration in Supersonic Flow. AIAA Paper No. 69-664. June 1969.
81. Rao, D. M. and Whitehead, A. H.: Lee-Side Vortices on Delta Wings at Hypersonic Speeds. AIAA Jour, Vol. 10, pp. 1458-1465, Nov. 1972.
82. Reding, J. P. and Ericsson, L. E.: Effects of Delta Dynamics. Jour. Of Spacecraft and Rockets, Vol. 10, No. 7, pp. 421-428, July 1973.
83. Richards, I. C.: Supersonic Flow Past a Slender Delta Wing. An Experimental Investigation Covering the Incidence Range -  $5^\circ < \alpha < 50^\circ$ . Aero. Quarterly. March 1976.
84. Schrader, K. F., Reynolds, G. A., and Novak, C. J.: Effects of Mach Number and Reynolds Number on Leading-Edge Vortices at High Angle-of-Attack. AIAA 88-0122. Jan. 1988.
85. Smith, J. H. B.: Improved Calculations of Leading Edge Separation from Slender, Thin, Delta Wings. Proc. Roy. Soc. A. 306, 67-90. 1968.
86. Smith, L. G. and Maurice, M. S.: Laser Velocimetry Measurements of Supersonic Vortex Flows on Simple Razor-Edged Delta Wing. AIAA Paper No. 91-1684. June 1991.
87. Snyder M. H. Jr.: On the Theory of the Delta Wing. Wichita State University AR 66-4. Sept. 1966.
88. Sorrells, R. B. III and Landrum, E. J.: Theoretical and Experimental Study of Twisted and Cambered Delta Wings Designed for a Mach Number of 3.5. NASA TN D-8247. Aug. 1976.
89. Stallings, R. L. and Lamb, M.: Wing-Alone Characteristics for High Angles of Attack at Supersonic Speeds. NASA TP 1889. July 1981.
90. Stallings, R. L., Lamb, M., and Watson, C. B.: Effect of Reynolds Number on Stability Characteristics of a Cruciform Wing-Body at Supersonic Speeds. NASA TP 1683. July 1980.
91. Stallings, R. L.: Low Aspect Ratio Wings at High Angles of Attack. Tactical Missile Aerodynamics. AIAA Prog. In Astro. and Aero. Vol. 104. 1986.
92. Szodruch, J. and Ganzer, U.: On the Lee-Side Flow Over Delta Wings at High Angle of Attack.
93. Szodruch, J. and Squire, L. C.: Pressure Distribution on the Suction Surface of Some Delta Wings at  $M = 3.5$ . A.R.C. 35 008. Jan. 1974.
94. Thomann, H.: Measurement of Heat Transfer, Recovery Temperature and Pressure Distribution on Delta Wings at  $M = 3$ . FFA Report 93, Sweden, 1962.

95. Thomas, J. L. and Newsome, R. W.: Navier-Stokes Computations of Lee-Side Flows Over Delta Wings. AIAA Paper 86-1049, May 1986.
96. Xing, W. F. and Marenbach, G.: Periodic Vortex Shedding in the Supersonic Wake of a Planar Plate. NASA TM 77854. May 1985.
97. Zubin, M. A. and Osteapenko, N. A.: The Experimental Investigation of Some Characteristics of the Supersonic Flow Around Delta Wings. Akad. Nauk SSSR. July 1975.
98. Aerodynamics of Vortical Type Flows in Three Dimensions. AGARD-CP-342. April 1983.
99. Fifty Years of Aeronautical Research. NASA EP-45.
100. Introduction to Vortex Dynamics. Von Karman Institute for Fluid Dynamics, Lecture Series 1986-08, Vol. 2. May 1986.
101. Vortex Flow Aerodynamics - Vol II. NASA CP 2417. Oct. 1985.
102. Smith, J. H. B.: A Review of Separation in Steady Three-Dimensional Flow. AGARD CP-168, May 1975
103. Sutton, E. P.: Some Observations of the Flow Over a Delta Winged Model with 55-deg Leading-Edge Sweep, at Mach Numbers between 0.4 and 1.8. A.R.C. Technical Report R&M No. 3190. 1960.
104. Szodruch, J.: Reynolds Number Influence on Leaside Flowfields. AIAA Journal Vol. 16, No. 12. 1978.
105. Szodruch, J. G. and Peake, D. J.: Leeward Flow Over Delta Wings at Supersonic Speeds. NASA TM 81187. April 1980.
106. Miller, D. S. and Wood, R. M.: Leaside Flows Over Delta Wings at Supersonic Speeds. Journal of Aircraft Vol 21, No. 9. Sept. 1984.
107. Wood, R. M. and Miller, D. S.: Impact of Airfoil Profile on the Supersonic Aerodynamics of Delta Wings. AIAA 85-4073.. Oct. 1985.
108. Wood, R. M. and Miller, D. S.: Fundamental Aerodynamic Characteristics of Delta Wings with Leading Edge Vortex Flows. Jour. Of Aircraft Vol. 22 No. 6. June 1985.
109. Wood, R. M. and Miller, D. S.: Assessment of Preliminary Prediction Techniques for Wing Leading-Edge Vortex Flows at Supersonic Speeds. Jour. Of Aircraft, Vol. 22, No. 6. June 1985.
110. Wood, R. M. and Watson, C. B.: Study of Lee-Side Flows Over Conically Cambered Delta Wings at Supersonic Speeds. NASA TP 2660 Part 1 and 2. July 1987.
111. Ganzer, U. and Szodruch, J.: Vortex Formation Over Delta, Double-Delta and Wave Rider Configurations at Supersonic Speeds. AGARD, Aerodynamics of Hypersonic Lifting Vehicles. Nov. 1987.
112. Covell, P. F. and Wesselman, G.: Flow Field Characteristics and Normal-Force Correlation's for Delta Wings from Mach 2.4 to 4.6. AIAA 89-0026. Jan. 1989.
113. Rainbird, W. J.: The External Flow Field About Yawed Circular Cones. AGARD CP-30. 1968.
114. Rainbird, W. J.: Turbulent Boundary Layer Growth and Separation on a Yawed 12.5 Cone at mach Numbers 1.8 and 4.25. AIAA Journal. Vol. 6, No. 12, pp. 2410-2416. Dec. 1968.
115. Graves, E. B. and Fournier, R. H.: Effect of Nose Bluntness and Afterbody Shape on Aerodynamic Characteristics of a Monoplanar Missile Concept With Bodies of Circular and Elliptical Cross Sections at a Mach Number of 2.50. NASA TM 80055. June 1979.
116. Allen, J. M. and Dillenius, F. E.: Vortex Development on Slender Missiles at Supersonic Speeds. AIAA 79-0360. Jan. 1979.
117. Allen, J. M. and Pittman, J. L.: Analysis of Surface Pressure Distributions on Two Elliptic Missile Configurations. AIAA 83-1841. July 1983.
118. Gartling, D. K.: Tests of Vortex Generators to Prevent Separation of Supersonic Flow in a Compression Corner. ARL-TR-70-44. Dec. 1970.
119. Hazelwood, R.: An Investigation of Cavity Vortex Generators in Supersonic Flow. NASA CR 198202. February 1996.
120. Samimy, M., Reeder, M., and Zaman, K.: Supersonic Jet Mixing Enhancement by Vortex Generations. AIAA Paper No. 91-2263. June 1991.

121. Greene, G. C., Lamar, J. E., and Kubendran, L. R.: Aircraft Vortices: Juncture, Wing, and Wake. AIAA 88-3742. Jan. 1988.
122. Kandil, O. A., Kandil, H. A., and Liu, C. H.: Three-Dimensional Supersonic Vortex Breakdown. AIAA 93-0526. Jan. 1993.
123. Siclari, M. J.: Asymmetric Separated Flows at Supersonic Speeds. AIAA Paper 90-0595. Jan. 1990.
124. Metwally, O. M.: The Interaction of a Supersonic Streamwise Vortex and a Normal Shock Wave. August 1989.
125. Settles, G. S. and Cattafesta, L.: Supersonic Shock Wave/Vortex Interaction. NASA CR 192917. April 1993.
126. Campbell, J. F., Osborn, R. F., and Foughner, J. T., Jr., Vortex Flow Aerodynamics, Vol II. NASA CR 2417. October 1985.
127. Marchman, J. F., Plentovich, E. B., and Manor, D.: Performance Improvement of Delta Wings at Subsonic Speeds Due to Vortex Flaps. AIAA Paper No. 80-1802. August 1980.
128. Erickson, G. E., Schreiner, J. A., and Rogers, L. W.: Multiple Vortex and Shock Interactions at Subsonic, Transonic, and Supersonic Speeds. AIAA Paper No. 90-3023. Aug. 1990.
129. Erickson, G. E., Schreiner, J. A., and Rogers, L. W.: Canard-Wing Vortex Interactions at Subsonic Through Supersonic Speeds. AIAA Paper No. 90-2814. August 1990.
130. McGrath, B. E.: Computational Study of a Conical Wing Having Unit Aspect Ratio at Supersonic Speeds. AIAA 93-3505. Aug. 1993.
131. McMillin, S. N.: Navier Stokes Solutions for Leaside Flows Over Supersonic Delta Wings - A Validation Study. GWU Thesis. July 1989.
132. McMillin, S. N., Thomas, J. L. and Murman, E. M.: Euler and Navier-Stokes Leaside Flows Over Supersonic Delta Wings. Jour. Of Aircraft Vol.26, No. 5. May 1989.
133. Miller, D. S. and Wood, R. M.: Lee-Side Flow Over Delta Wings at Supersonic Speeds. NASA TP 2430. June 1985.
134. Powell, K. G., Murman, E. M., Wood, R. M., and Miller, D. S.: A Comparison of Experimental and Numerical Results for Delta Wings with Vortex Flaps. AIAA - 86-1840. June 1986.
135. Rose, O. J. and Pittman, J. L.: An Euler Analysis of Leading Edge Vortex Flows On a Forebody-Strake at Supersonic Speeds. AIAA 89-0343. Jan. 1989.
136. Shrout, B. L. and Robins, A. W.: Longitudinal Aerodynamic Characteristics of an Elliptical Body with a Horizontal Tail at Mach Numbers From 2.3 to 4.63. NASA TP 2024. June 1982.
137. Wood, R. M., Byrd, J. E., Krieger, W. B., and Forrest, D. K.: Experimental Investigation of the Aerodynamic Characteristics of Eight Forebody Geometries at Supersonic Speeds. NASA TM 4625. July 1997.
138. Wood, R. M., Byrd, J. E., and Wesselman, G. F.: Influence of Airfoil Geometry on Delta Wing Leading-Edge Vortices and Vortex-Induced Aerodynamics at Supersonic Speeds. NASA TP 3105. Feb. 1992.
139. Stallings, R. L., Jr., "Store Separation from Cavities at Supersonic Flight Speeds," J. Spacecraft & Rockets, vol. 20, no. 2, Mar. - Apr. 1983, pp. 129-132.
140. Stallings, R. L., Jr., and Wilcox, F. J., Jr., "Experimental Cavity Pressure Distributions at Supersonic Speeds," NASA TP-2683, 1987.
141. Charwat, A. F., Roos, J. N., Dewey, F. C., Jr., and Hitz, J. A., "An Investigation of Separated Flows," J. Aeronaut, Sci., vol. 28. "Part I: The Pressure Field," no. 6, June 1961, pp. 457-470. "Part II: Flow in the Cavity and Heat Transfer," no. 7, July 1961, pp. 513-527.
142. McDearman, R. W., "Investigation of the Flow in a Rectangular Cavity in a Flat Plate at a Mach Number of 3.55," NASA TN D-523, 1960.
143. Kaufman, L. G., II; Maciulaitis, A.; and Clark, R. L.: "Mach 0.6 to 3.0 Flows Over Rectangular Cavities," AFWAL-TR-82-3112, U. S. Air Force, May 1983.
144. McGregor, O. W., Jr., "Aerodynamic Drag of Two-Dimensional Rectangular Notches in Transonic and Supersonic Turbulent Flow (With Emphasis on the Effect of Self-Induced Pressure Oscillations)," Ph.D. Diss., Univ. of Illinois, Urbana, Illinois, Oct. 1969.

145. Nestler, D. E., "An Experimental Study of Cavity Flow on Sharp and Blunt Cones at Mach 8," AIAA Paper 81-0335, Jan. 1981.
146. Blair, A. B., Jr., and Stallings, R. L., Jr., "Supersonic Axial-Force Characteristics of a Rectangular-Box Cavity With Various Length-to-Depth Ratios in a Flat Plate," NASA TM-87659, Apr. 1986.
147. Wilcox, F. J., Jr., "Experimental Measurements of Internal Store Separation Characteristics at Supersonic Speeds," Presented at the Store Carriage, Int., and Release Conf., Spon. by the Royal Aero. Soc., Bath, United Kingdom, Apr. 4-6, 1990.
148. Wilcox, Floyd J., Jr.: Use of a Colored Water Flow Visualization Technique in a Supersonic Wind Tunnel to Investigate Cavity Flow Fields. Flow Visualization VI - Proceedings of the Sixth International Symposium on Flow Visualization, October 5-9, 1992, Yokohama, Japan; Springer-Verlag, Germany, 1992, pp. 41-45.
149. Jackson, Charlie M., Jr.; Corlett, William A.; and Monta, William J.: Description and Calibration of the Langley Unitary Plan Wind Tunnel. NASA TP-1905, 1981.
150. Morris, Odell A.; Corlett, William A.; Wassum, Donald L.; and Babb, C. Donald: Vapor-Screen Technique for Flow Visualization in the Langley Unitary Plan Wind Tunnel. NASA TM-86384, July 1985.
151. Stallings, Robert L., Jr.; Wilcox, Floyd J., Jr.; and Forrest, Dana K.: Measurements of Forces, Moments, and Pressures on a Generic Store Separating From a Box Cavity at Supersonic Speeds. NASA TP 3110, Sept. 1991.
152. Birch, T., Allen, J., and Wilcox, F.: Force, Surface Pressure and Flowfield Measurements on Slender Missile Configurations at Supersonic Speeds. AIAA Paper No. AIAA-2000-4207. August 2000.
153. Allen, J. M. and Shaw, D.S. and Sawyer, W. C.: Analysis of Selected Data From the Triservice Data Base. AIAA-89-0478. Jan. 1989.
154. Blair, A.B., Jr., Allen, J. M. and Hernandez, G.: Effect of Tail-Fin Span on Stability and Control Characteristics of a Canard-Controlled Missile at Supersonic Mach Numbers. NASA TP-2157. June 1983.
155. Blair, A.B., Jr.: Supersonic Aerodynamics Characteristics of a Maneuvering Canard-Controlled with Fixed and Free-Rolling Tail Fins. SAE TP-901993. Oct. 1990.
156. Covell, P. F., Miller, D. S., and Wood, R. M.: An Investigation of Leading-Edge Flap Performance on Delta and Double-Delta Wings at Supersonic Speeds. AIAA 86-0315. Jan. 1986.
157. Covell, P. F., Wood, R. M., and Miller, D. S.: Investigation of Leading-Edge Flap Performance on Delta and Double-Delta Wings at Supersonic Speeds. NASA TP 2656. April 1987.
158. Darden, C. M.: Effect of Leading-Edge Load Constraints on the Design and Performance of Supersonic Wings. NASA TP 2446. July 1985.
159. Darden, C. M.: Effect of Milling Machine Roughness and Wing Dihedral on the Supersonic Aerodynamic Characteristics of a Highly Swept Wing. NASA TP 2918. Aug. 1989.
160. Erickson, G. E.: Wind Tunnel Investigation of the Interaction and Breakdown Characteristics of Slender-Wing Vortices at Subsonic, Transonic, and Supersonic Speeds. NASA TP 3114, Nov. 1991.
161. Johnson, S. K: Flow Field Study at Engine inlet Stations of Two High-Speed Cruise Aircraft. NASA TP 2861. Feb. 1989.
162. Hernandez, G., Wood, R. M., and Covell, P. F.: Effect of Leading- and Trailing-Edge Flaps on Clipped Delta Wings With and Without Wing Camber at Supersonic Speeds. NASA TM 4542. May 1994.
163. McMillin, S. N., Bauer, S. X. S., and Howell, D. T.: Effect of Planform and Body on Supersonic Aerodynamics of Multibody Configurations. NASA TP 3212. Sept. 1992.
164. McMillin, S. N. and Wood, R. M.: Planform Effects on the Supersonic Aerodynamics of Multibody Configurations. NASA TP 2762. Dec. 1987.
165. Robins, A. W., Carlson, H. W., and Mack, R. J.: Supersonic Wings With Significant Leading-Edge Thrust at Cruise. NASA TP 1632. April 1980.

166. Robins, A. W., Lamb, M., and Miller, D. S.: Aerodynamic Characteristics at Mach Numbers of 1.5, 1.8, and 2.0 of a Blended Wing-Body Configuration With and Without Integral Canards. NASA TP 1427. May 1979.
167. Shrout, B. L.: Effect of a Canard and Wing Leading-Edge Flaps on the Longitudinal Aerodynamic Performance of a Cranked Wing at Supersonic Speeds. NASA TM 89126. Aug. 1987.
168. Wood, R. M., Miller, D. S., Raney, D. L., and Roesch, M. T.: A Low Lift Wing Camber Design Approach for Fighter Aircraft. NASA TP 2465. August 1985.
169. Wood, R. M., Rose, O. J., and McMillin, S. N.: Effect of Body Cross-Sectional Shape on the Supersonic Aerodynamics of Multibody Configurations. NASA TP 2587. July 1986.
170. Carlson, H. W. and Mann, M. J.: Survey and Analysis of Research on Supersonic Drag-Due-to-Lift Minimization With Recommendations for Wing Design. NASA TP 3202. Sept. 1992.
171. Johnson, M. E.: A Design and Analysis of Maneuver Wing Flaps at Supersonic Speeds With Attainable Leading-Edge Thrust Considerations. NASA CR 3939. Oct. 1985.
172. Kulfan, R. M.: Real Flow Limitations in Supersonic Airplane Design. AIAA 78-147. Jan. 1978.
173. Mason, W. H.: A Wing Concept for Supersonic Maneuvering. NASA CR 3763. Dec. 1983.
174. Mason, W. H., Siclari, M. J., Miller, D. S.: A Supersonic Maneuver Wing Designed for Nonlinear Attached Flow. AIAA 83-0425. Jan. 1983.
175. Maskell, E. C.: On the Principles of Aerodynamic Design. Progress in Aero. Sci., Vol. 1, No. 1, 1961, pp. 1-7.
176. Miller, D. S., Landrum, E. J., Townsend, J. C., and Mason, W. H.: Pressure and Force Data for a Flat Wing and a Warped Conical Wing Having a Shockless Recompression at Mach 1.62. NASA TP 1759. April 1981.
177. Miller, D. S. and Wood, R. M.: Aerodynamic Design Considerations for Efficient High-Lift Supersonic Wings. AIAA 85-4076. Oct. 1985.
178. Nelson, C. P.: Effects of Wing Planform on HSCT Off-Design Aerodynamics. AIAA 92-2629-CP. 1992.
179. Seddon, J. and Spence, A.: The Use of Known Flow Fields as an Approach to the Design of High Speed Aircraft. AGARD Fluid Dyn. Spec. Meeting May 1968.
180. Covell, R. F., Wood, R. M., and Miller, D.S.: Investigation of the Vortex Flap Concept on a 75-deg. Sweep Delta Wing at Supersonic Speeds. AIAA 87-2475. Aug. 1987.
181. Kulfan, R. M.: Wing Geometry Effects on Leading Edge Vortices. AIAA Paper No. 79-1872. August 1979.
182. Wood, R. M.: Supersonic Aerodynamics of Delta Wings. NASA TP 2771. March 1988.
183. Wood, R. M. and Bauer, S. X. S.: The Natural Flow Wing-Design Concept. NASA TP 3193, May 1992.



Figure 1. Photograph of the galaxy M100.

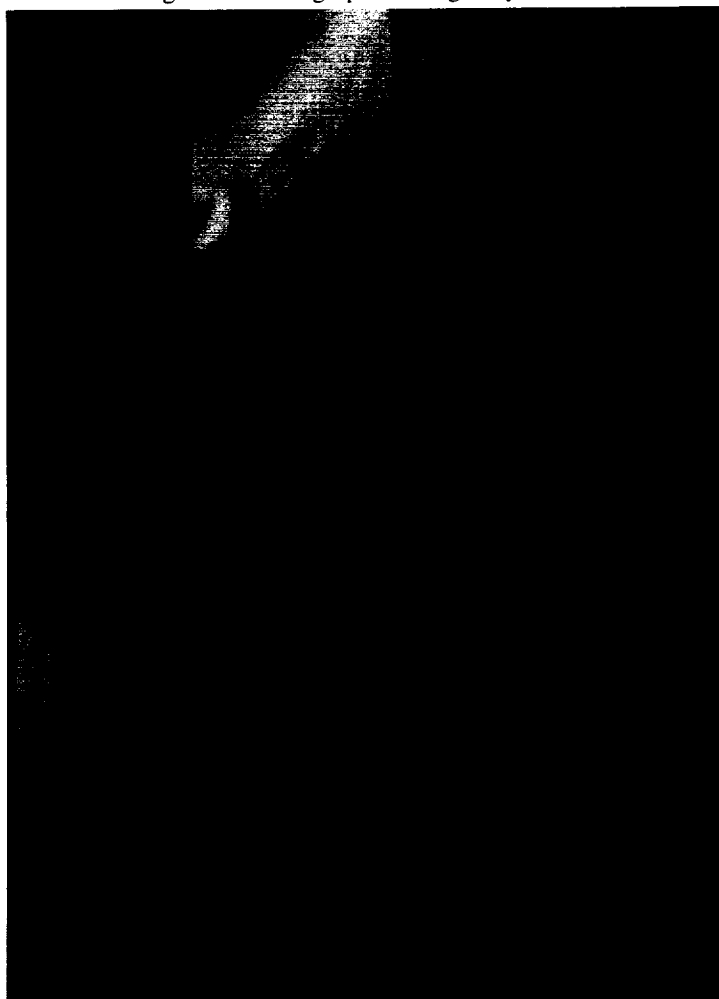


Figure 2. Photograph of the Red Spot on Jupiter.



Figure 3. Photograph of a Tornado.



Figure 4. Photograph of XB-70 in Supersonic flight.

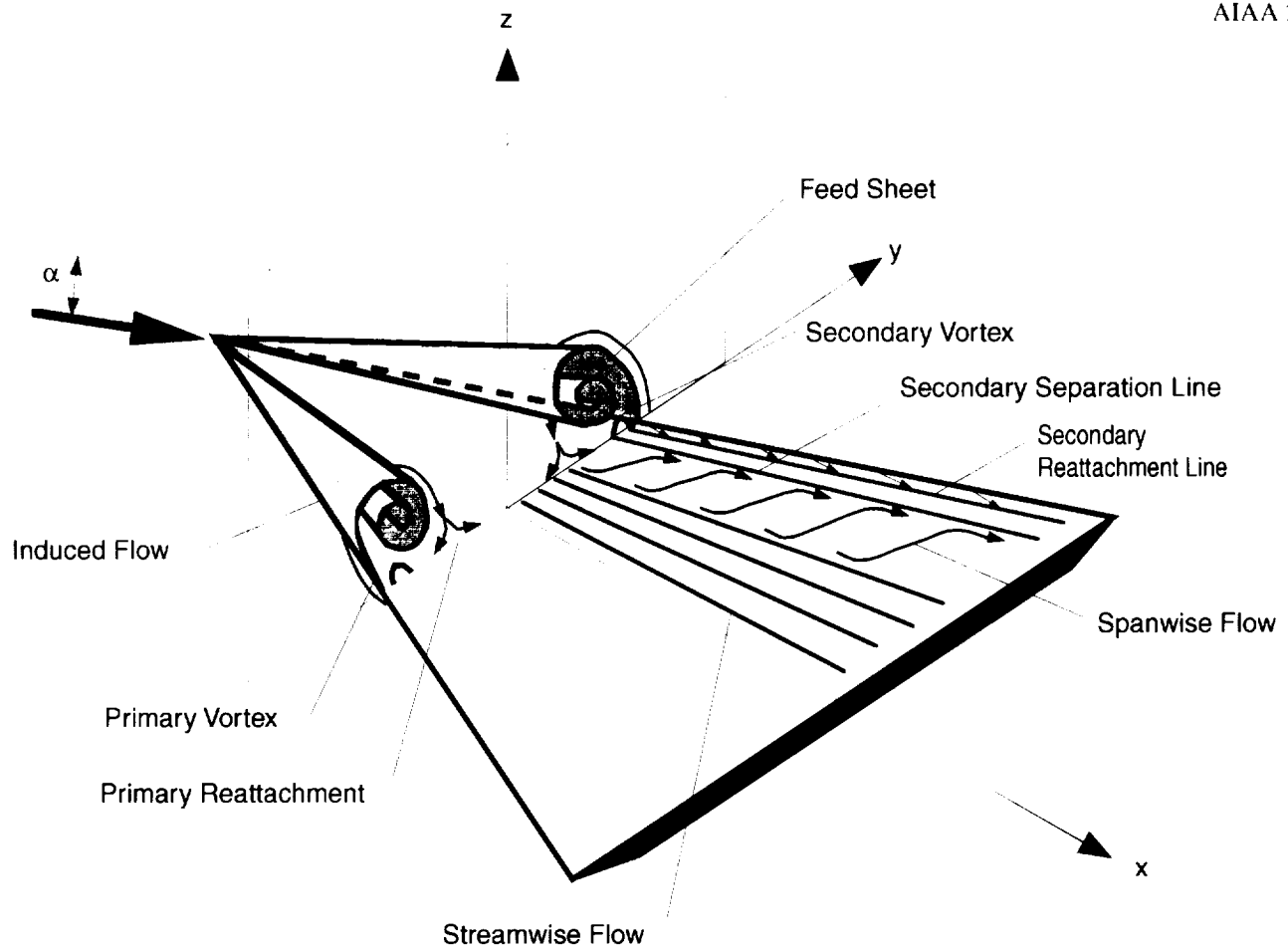


Figure 5. Sketch of sharp leading edge wing vortex flow on a delta wing at angle-of-attack.

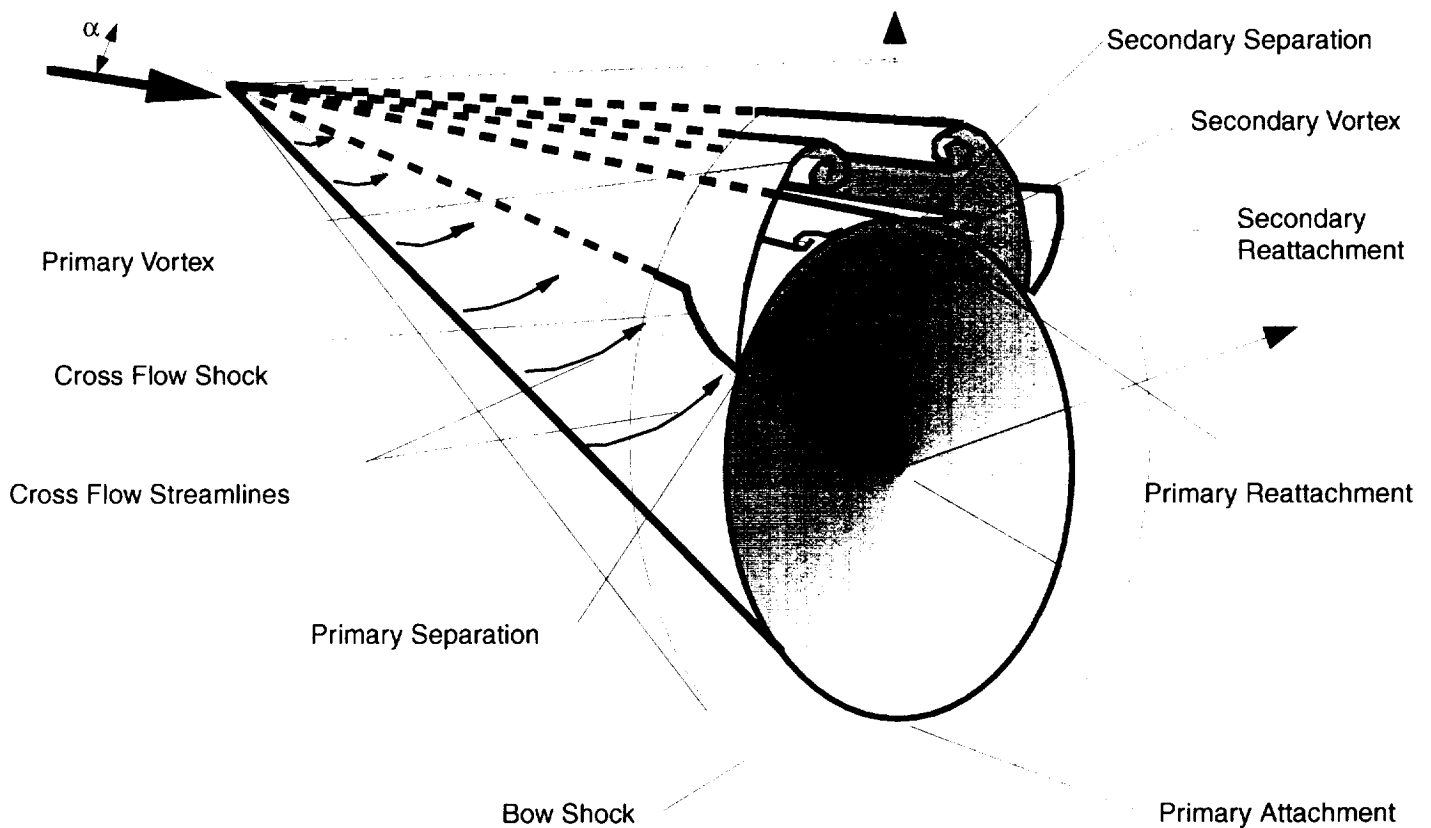


Figure 6. Sketch of smooth wall vortex flow on a conical forebody at angle-of-attack..

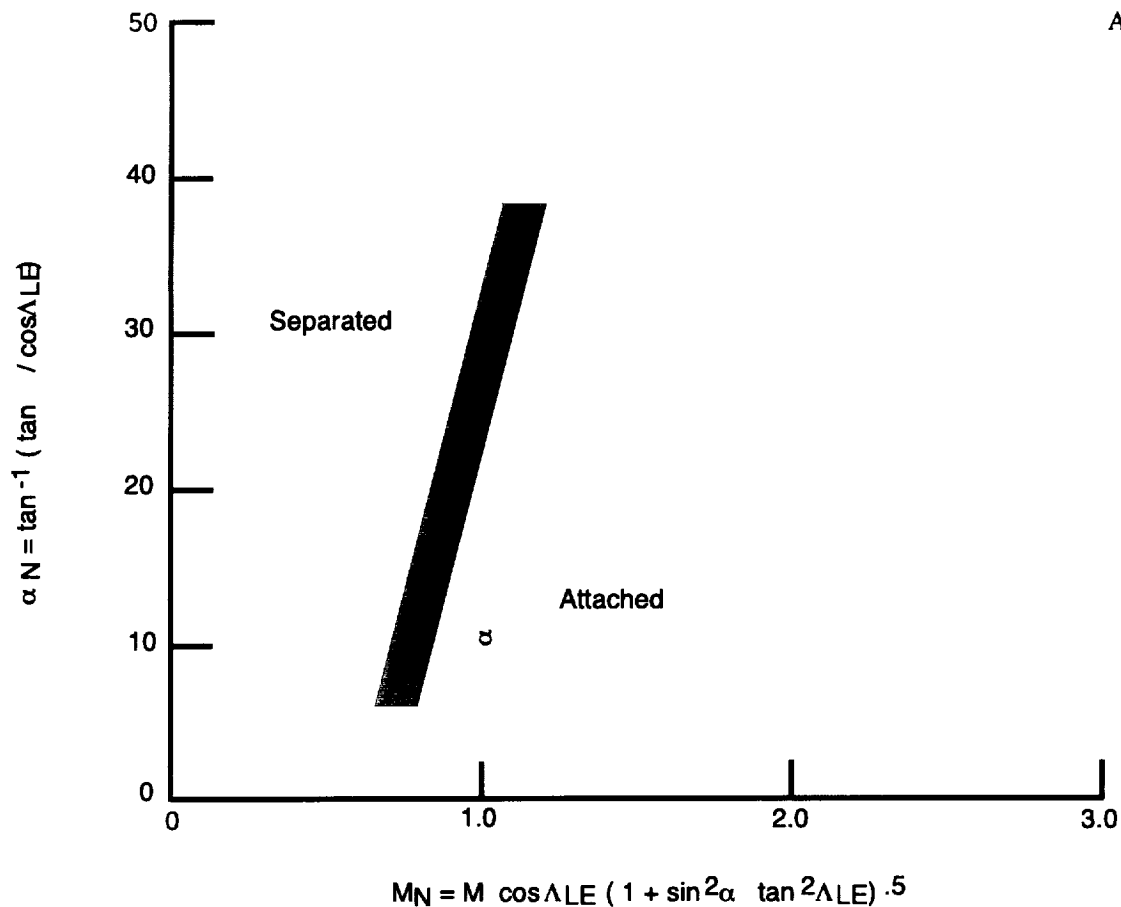


Figure 7. Stanbrood - Squire lee-side vortex flow classification for delta wings.

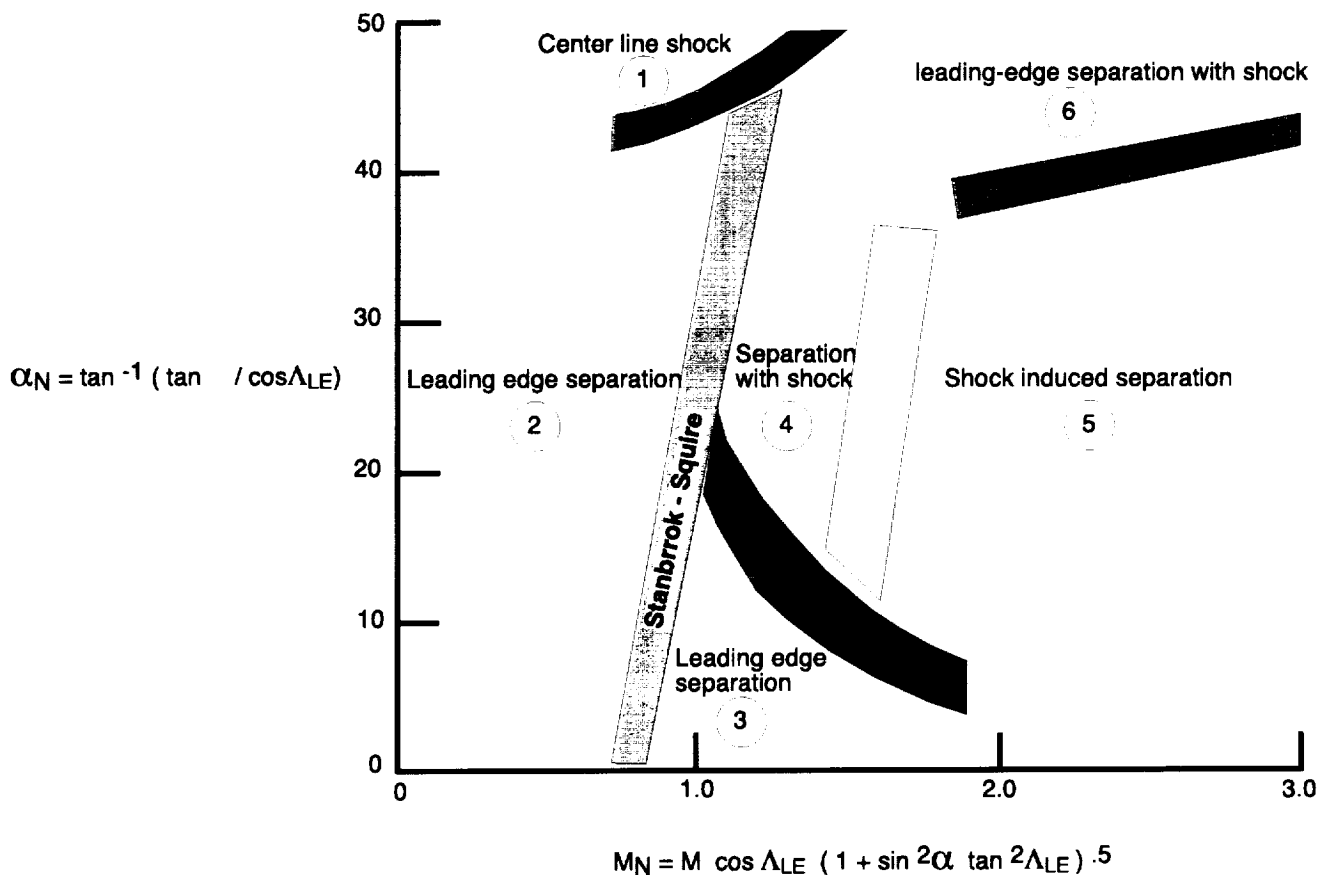


Figure 8. Szodruch - Peake lee-side vortex flow classification for delta wings.

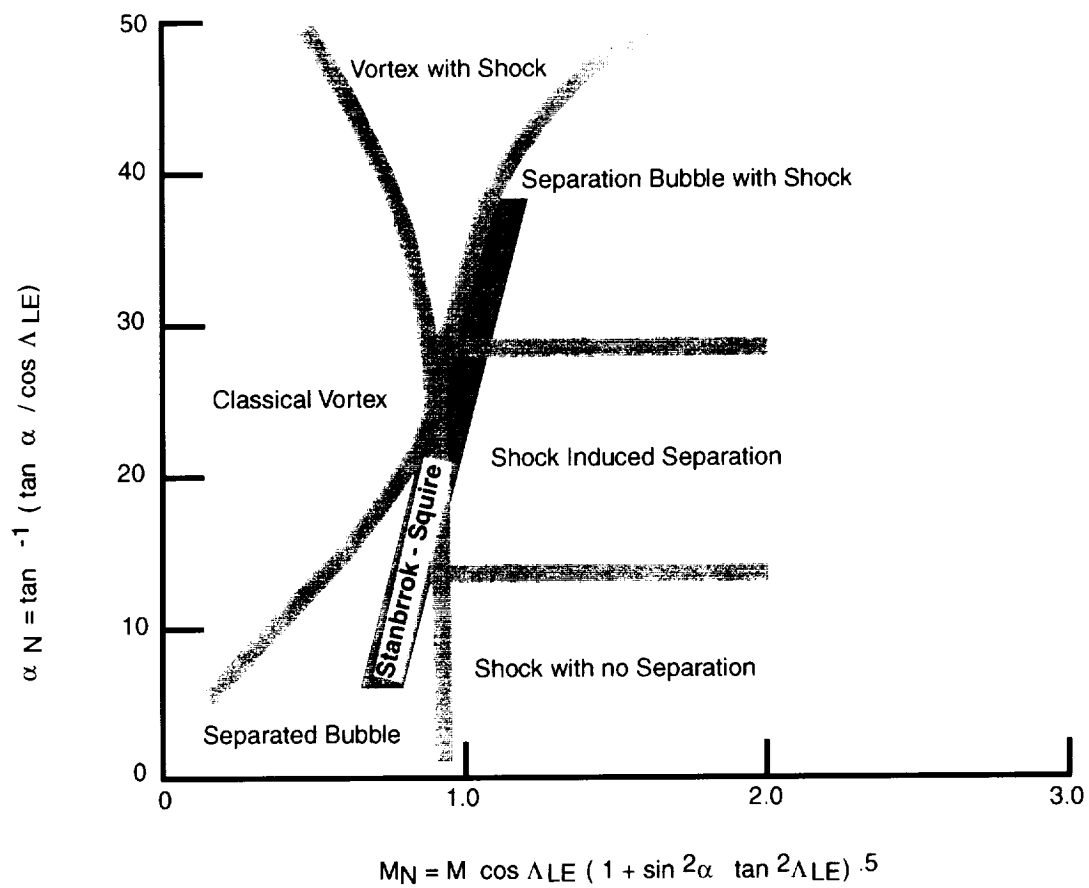


Figure 9. Miller - Wood lee-side vortex flow classification for delta wings.

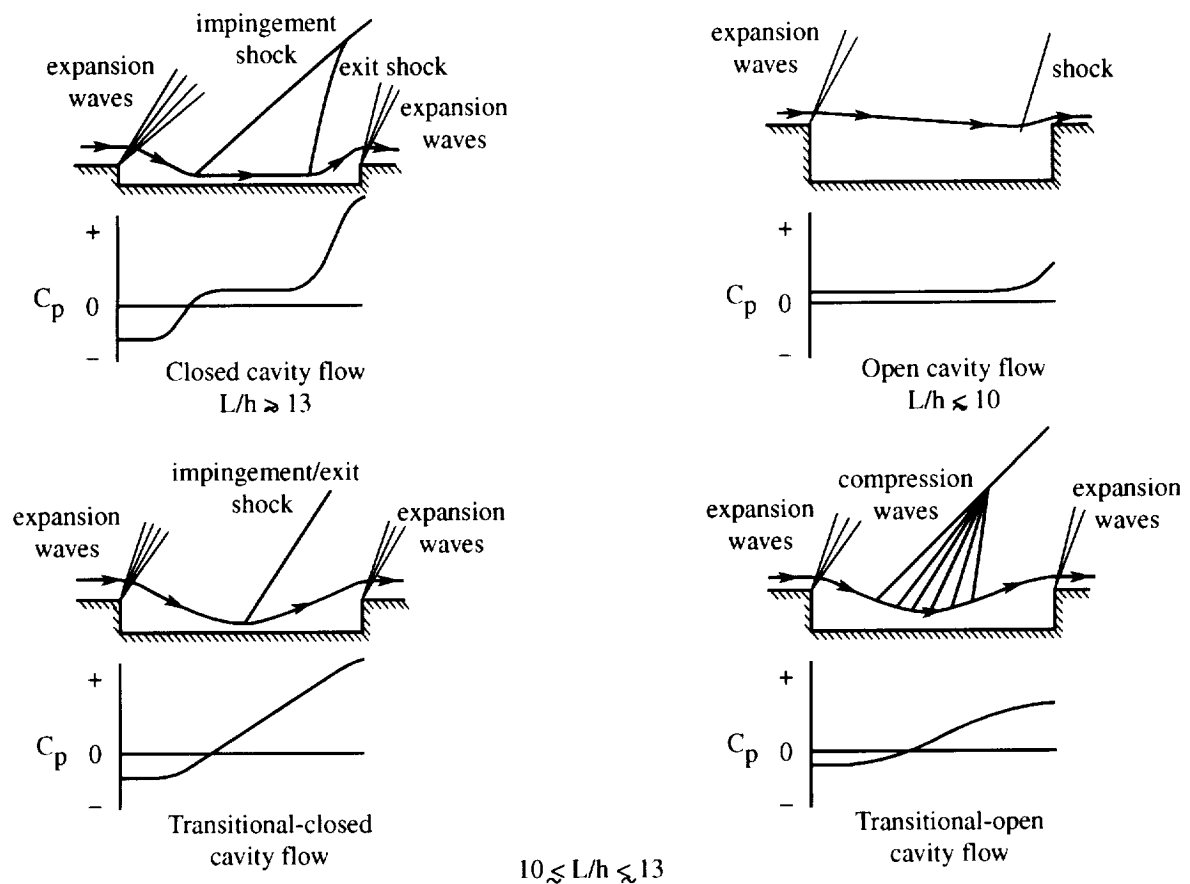
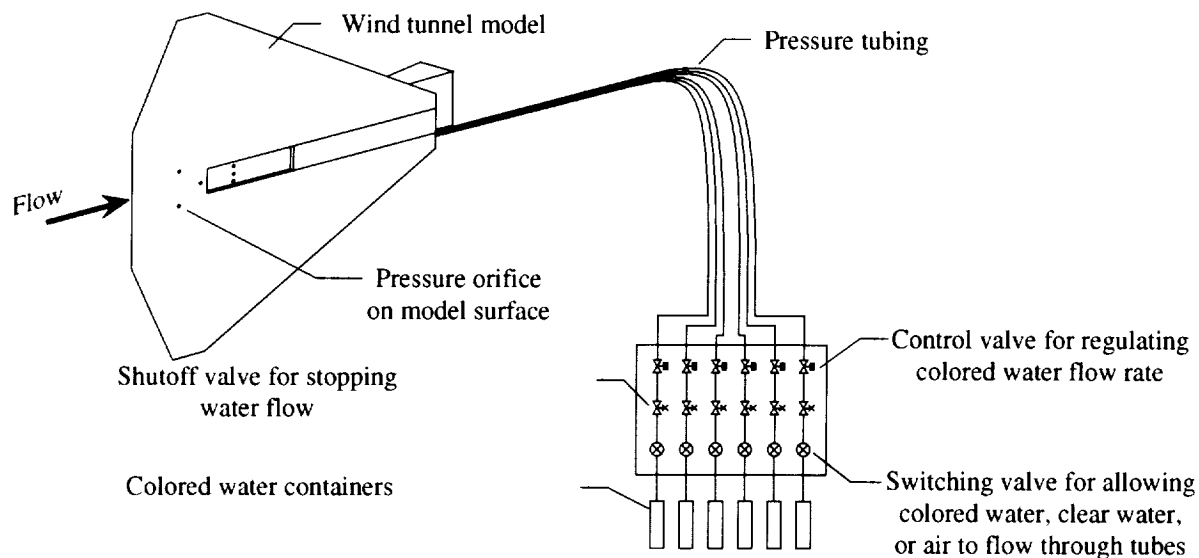
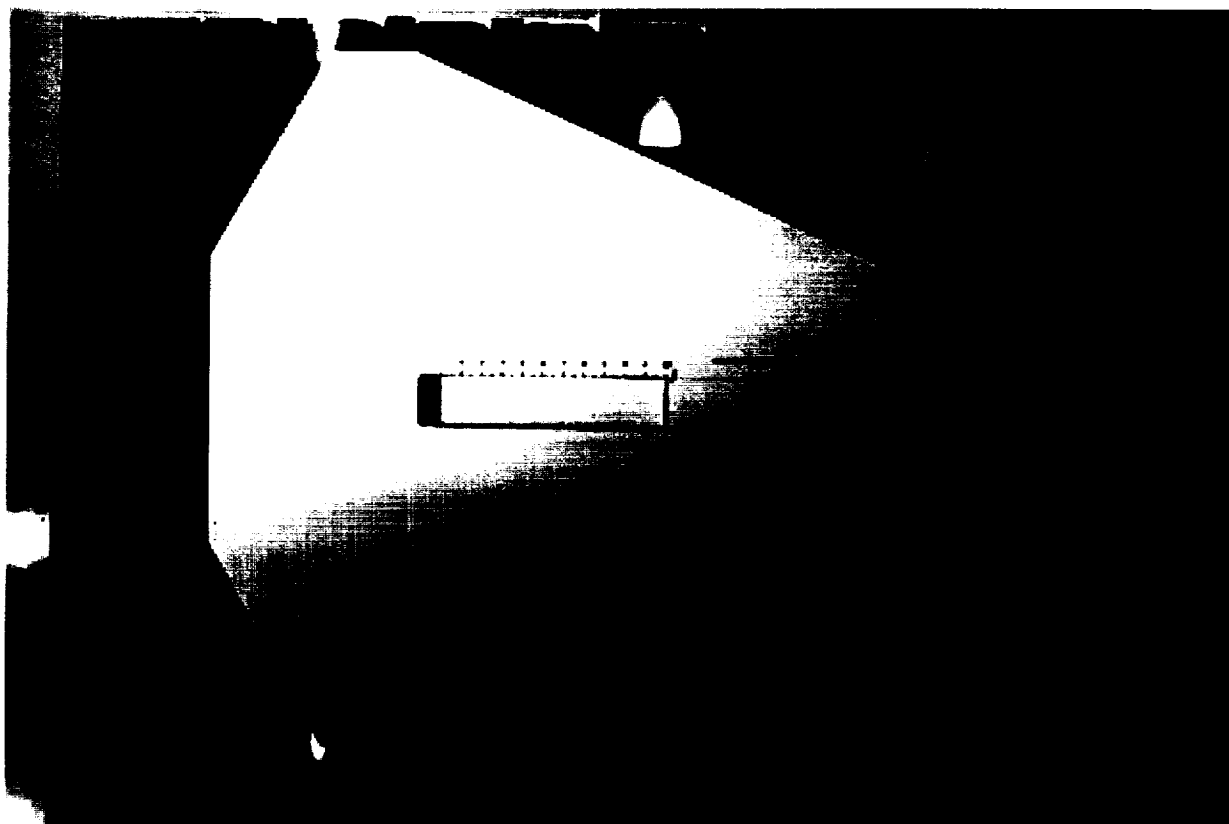


Figure 10. Flow field sketches and typical pressure distributions of rectangular box cavities at supersonic speeds (ref. 147).



(a) Schematic of colored water flow apparatus.



(b) Photograph of flat plate model mounted in wind tunnel.

Figure 11. Colored water flow experimental apparatus (ref. 148).

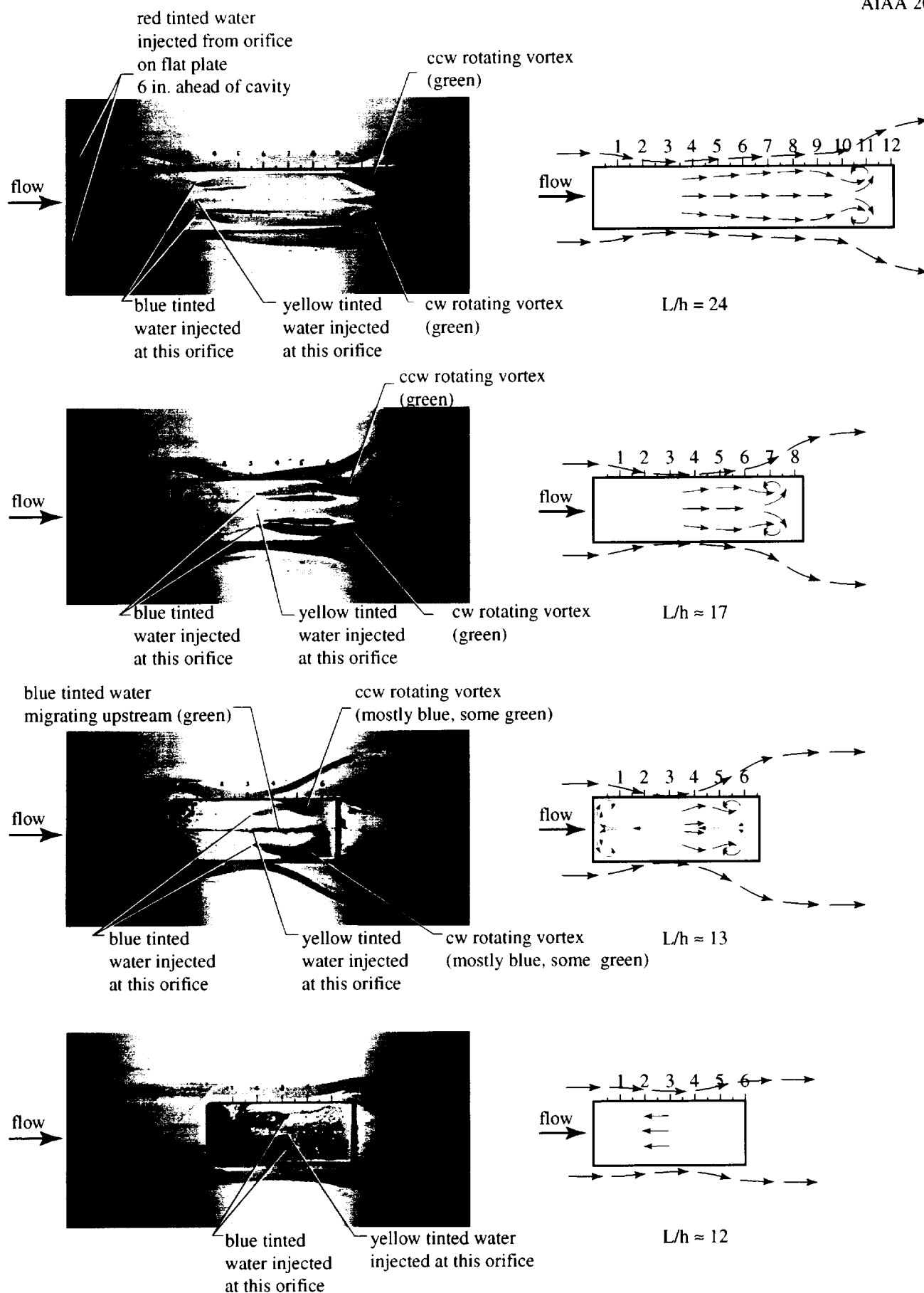


Figure 12. Visualization of surface flow fields on cavity floor at  $M = 1.50$  using colored water technique. Cavity height = 0.5 in. (ref. 148).



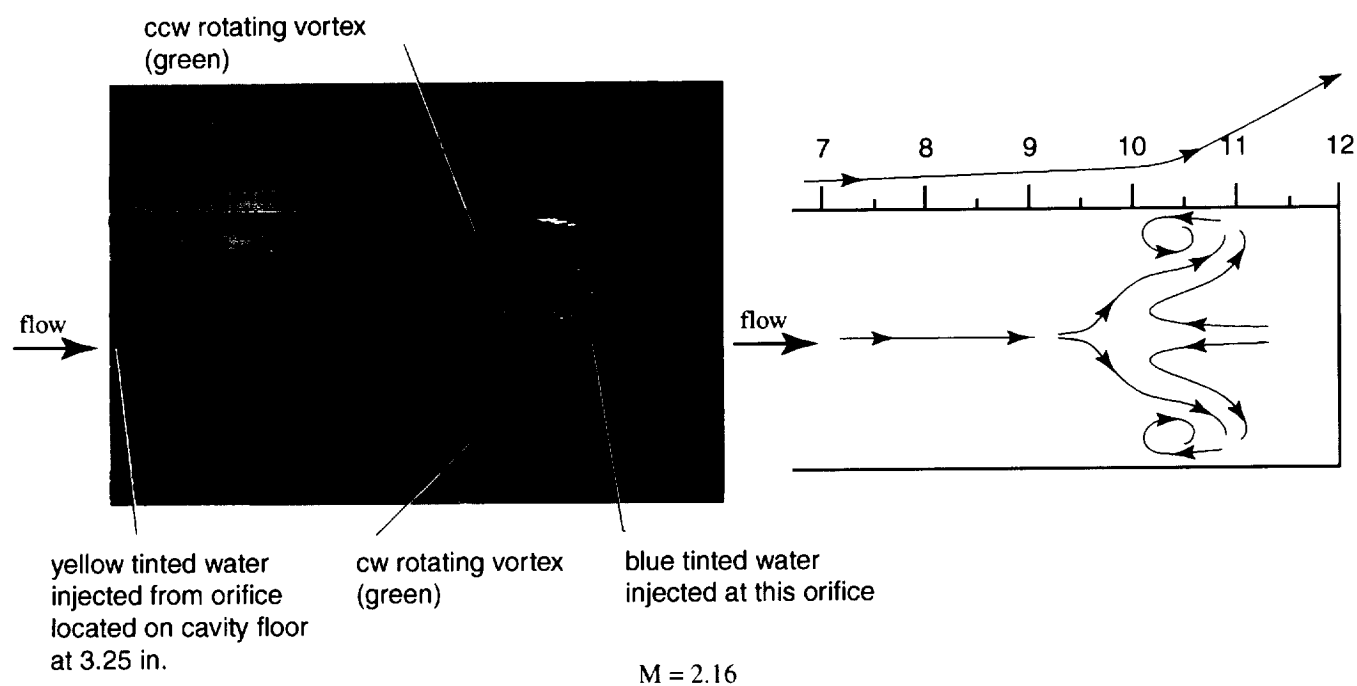
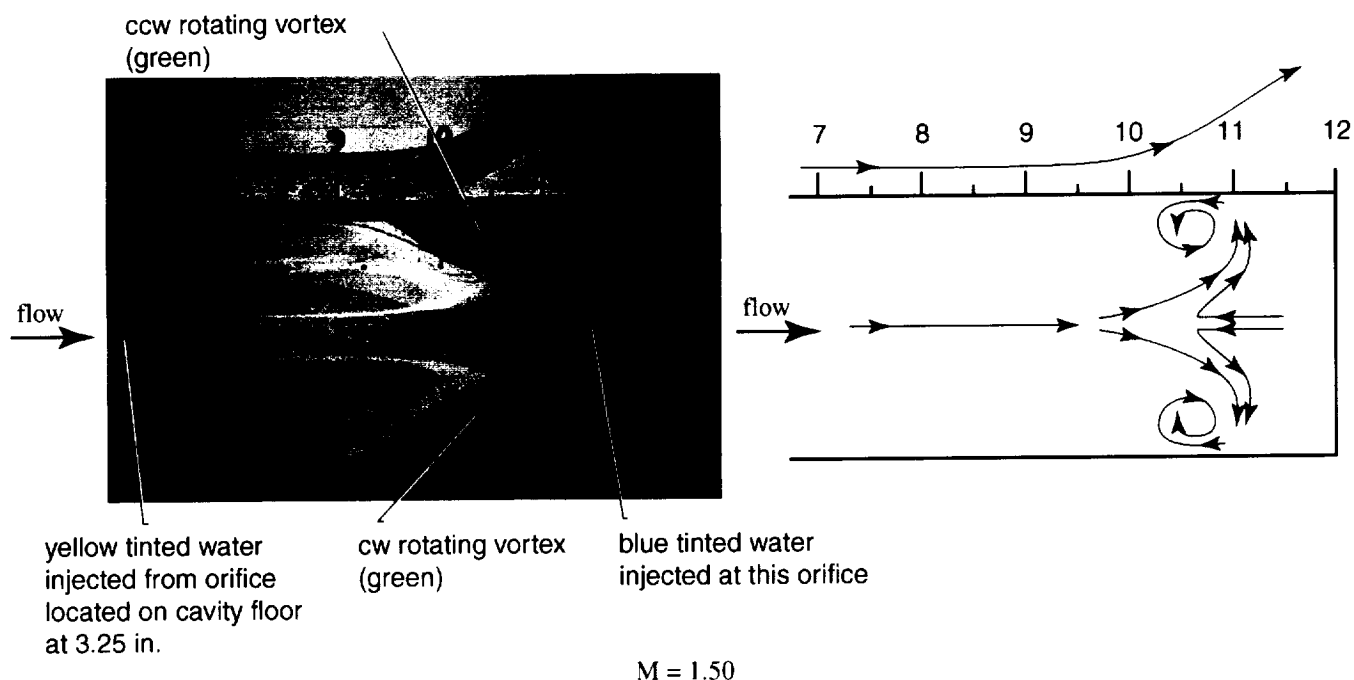


Figure 14. Visualization of cavity flow field at rear of cavity.  $L/h = 24.0$ , Cavity height = 0.5 in. (ref. 148).

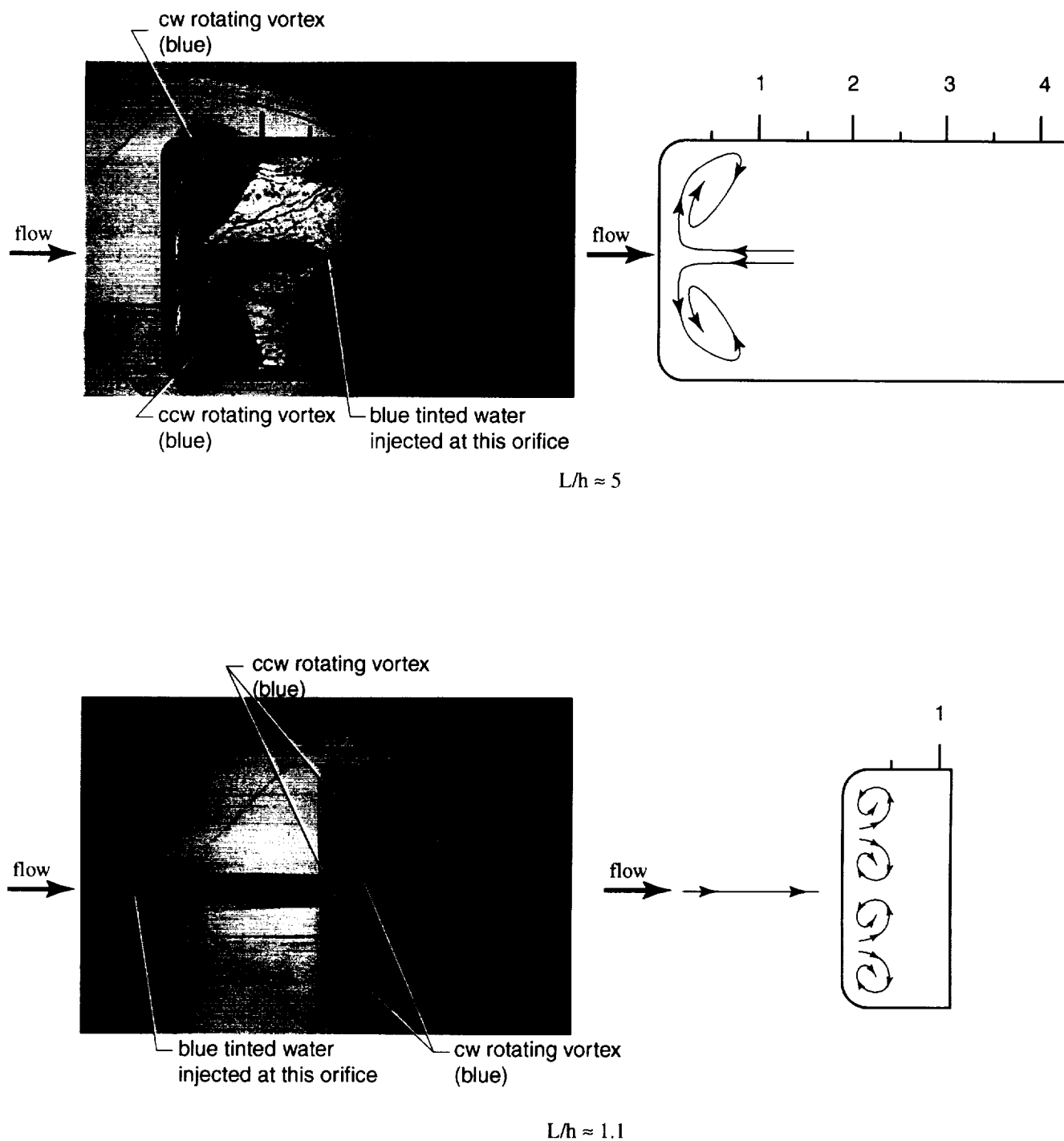


Figure 15. Visualization of cavity flow field at front of cavity.  $M = 1.50$ , Cavity height = 0.5 in. (ref. 148).

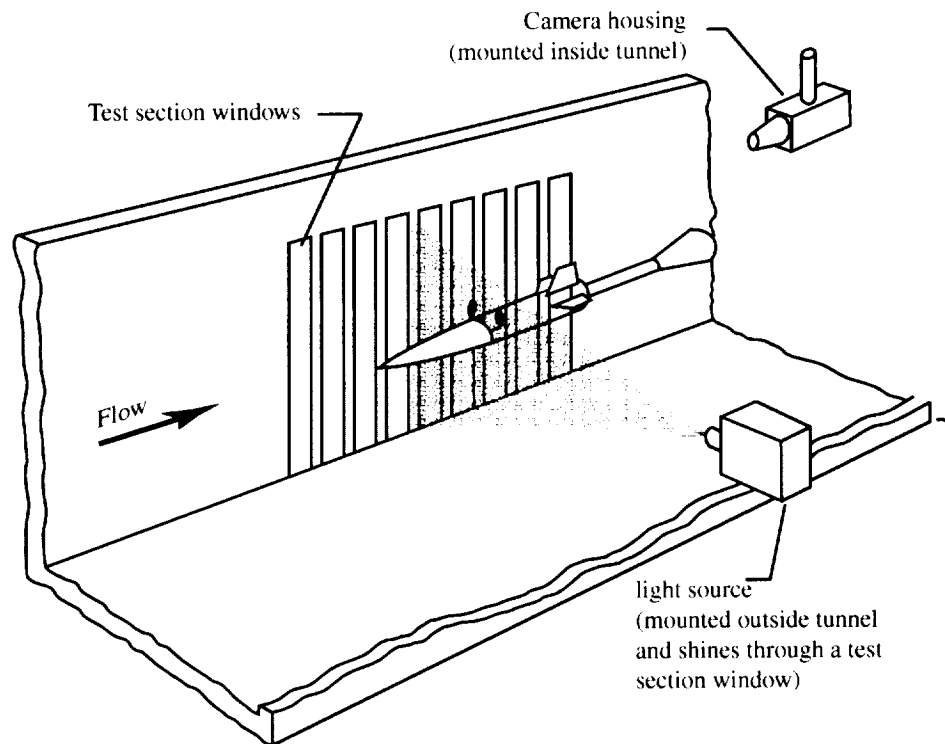


Figure 16. Vapor screen apparatus setup in Langley Unitary Plan Wind Tunnel (ref. 150).

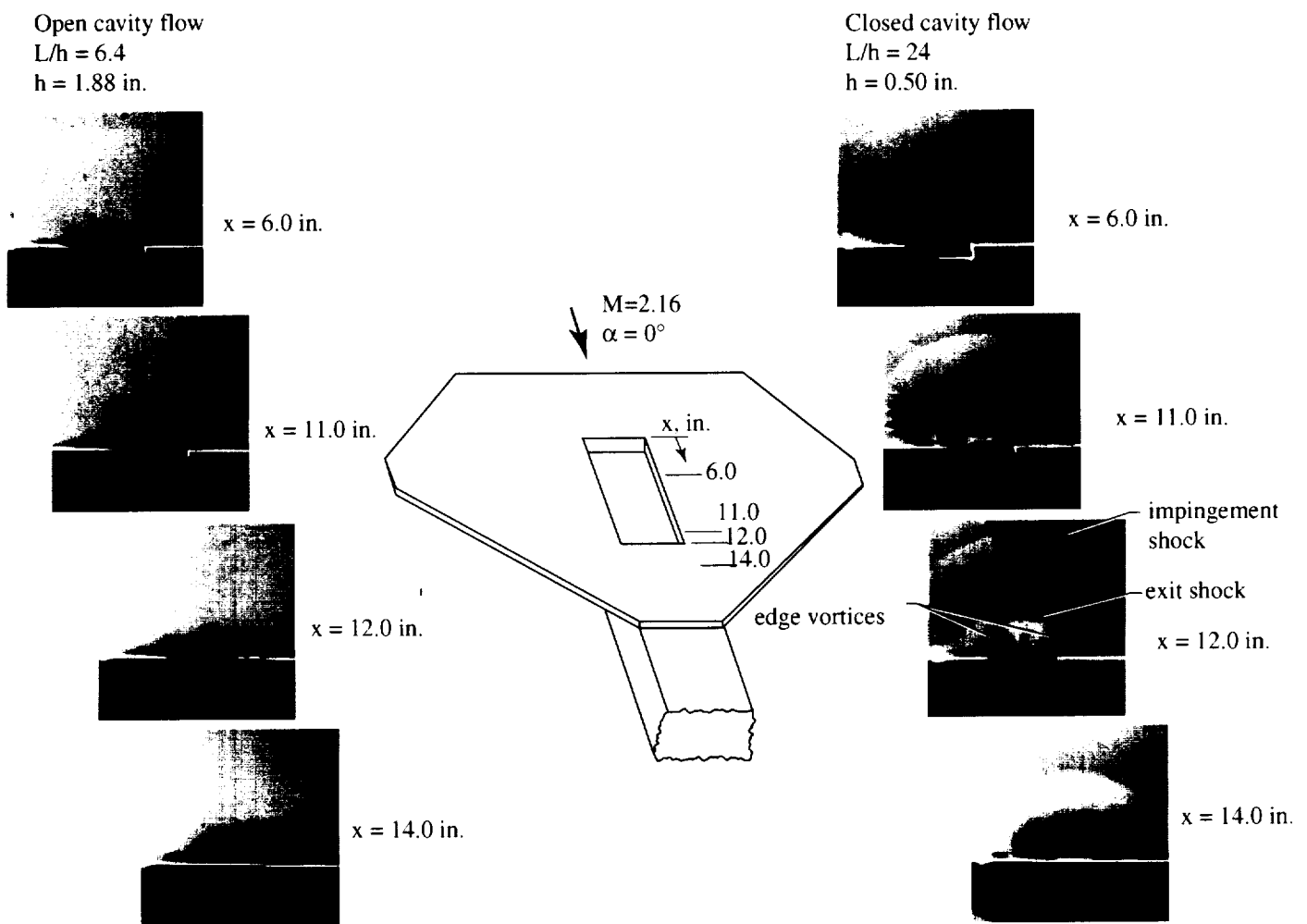


Figure 17. Vapor screen photographs of open and closed cavity flow (ref. 146).

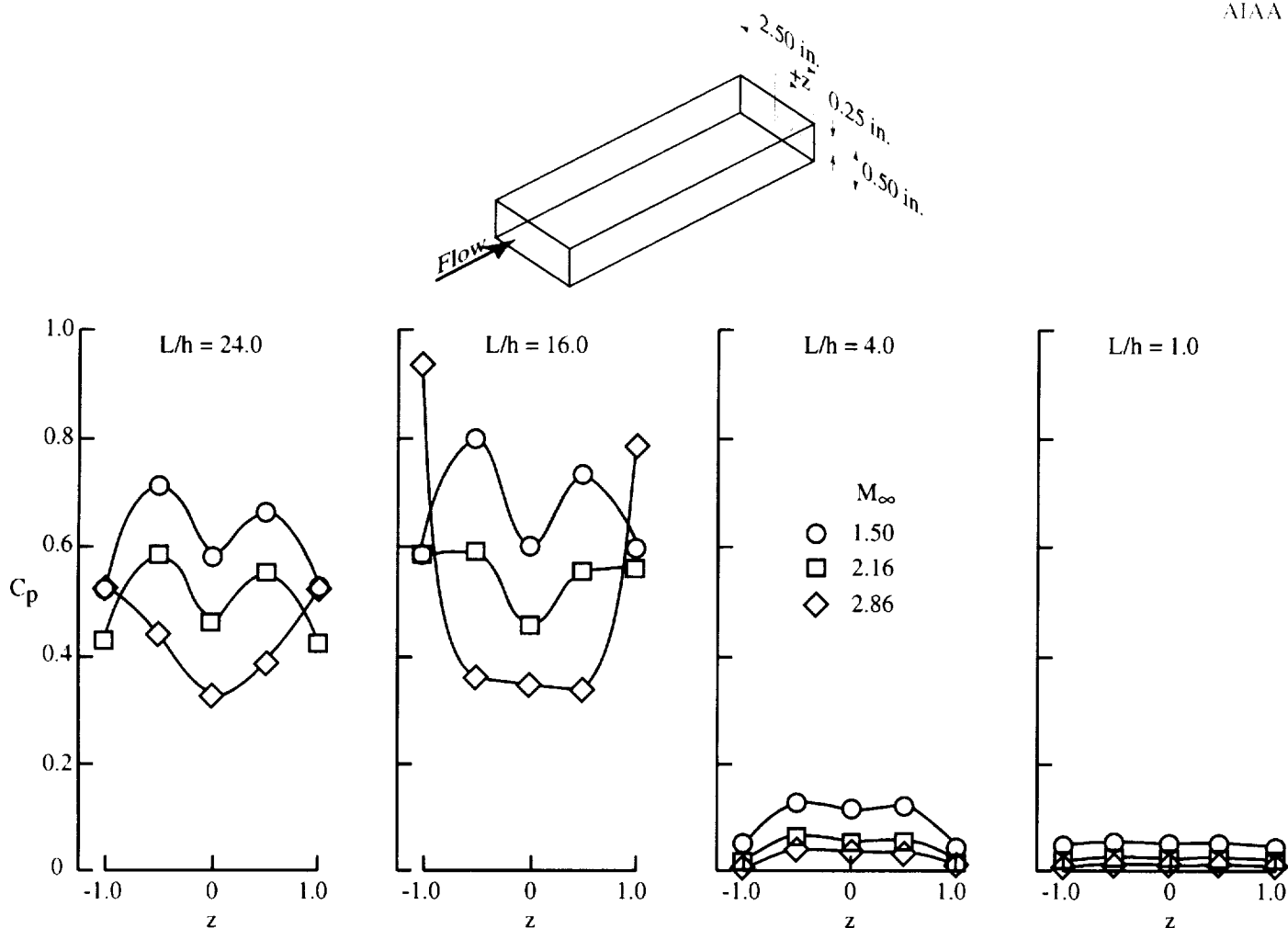


Figure 18. Lateral pressure distribution measured on cavity rear face. Cavity width = 2.5 in. (ref. 140).

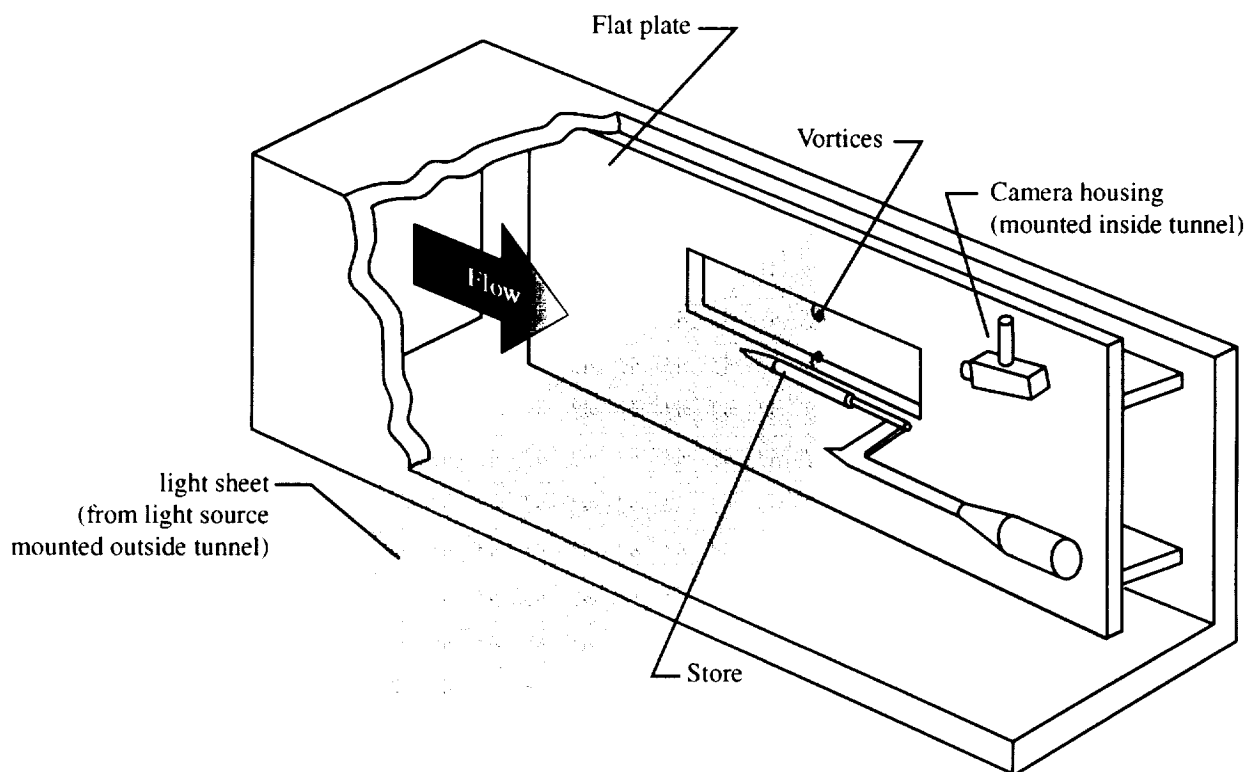


Figure 19. Vapor screen setup for store separation tests in Langley UPWT (ref. 151).

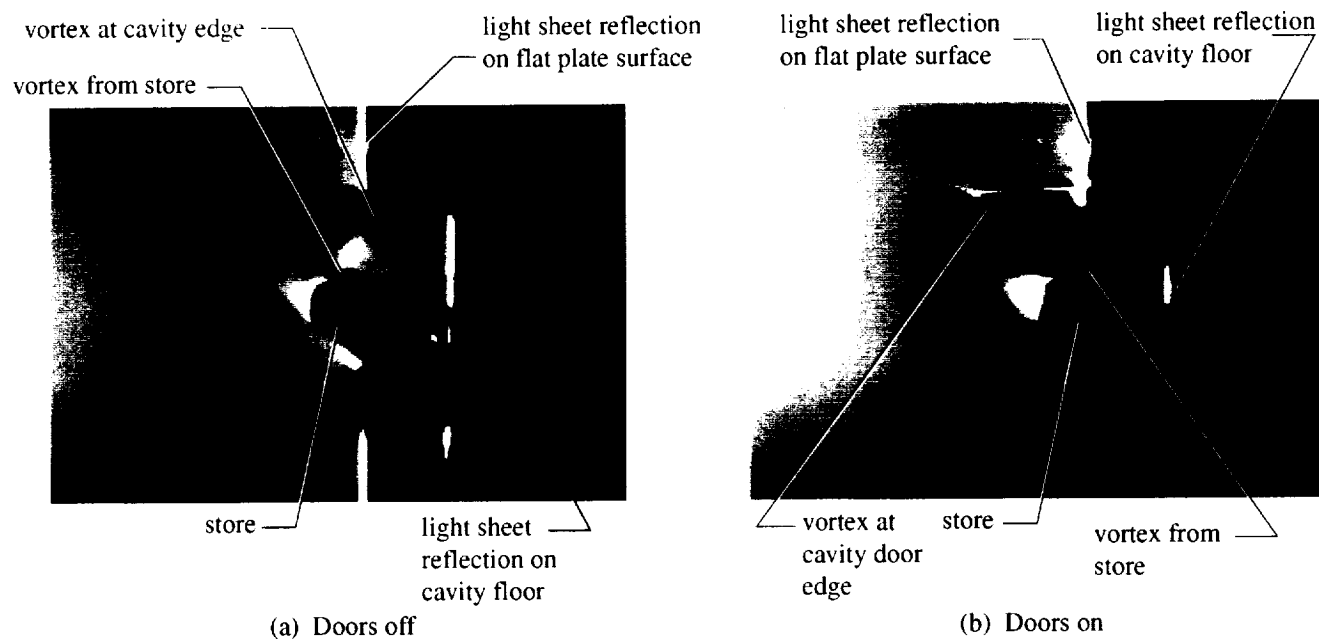


Figure 20. Vapor screen photographs of store in vicinity of cavity with and without doors at  $M=2.65$ ,  $L/h=12.07$ . (ref. 151).

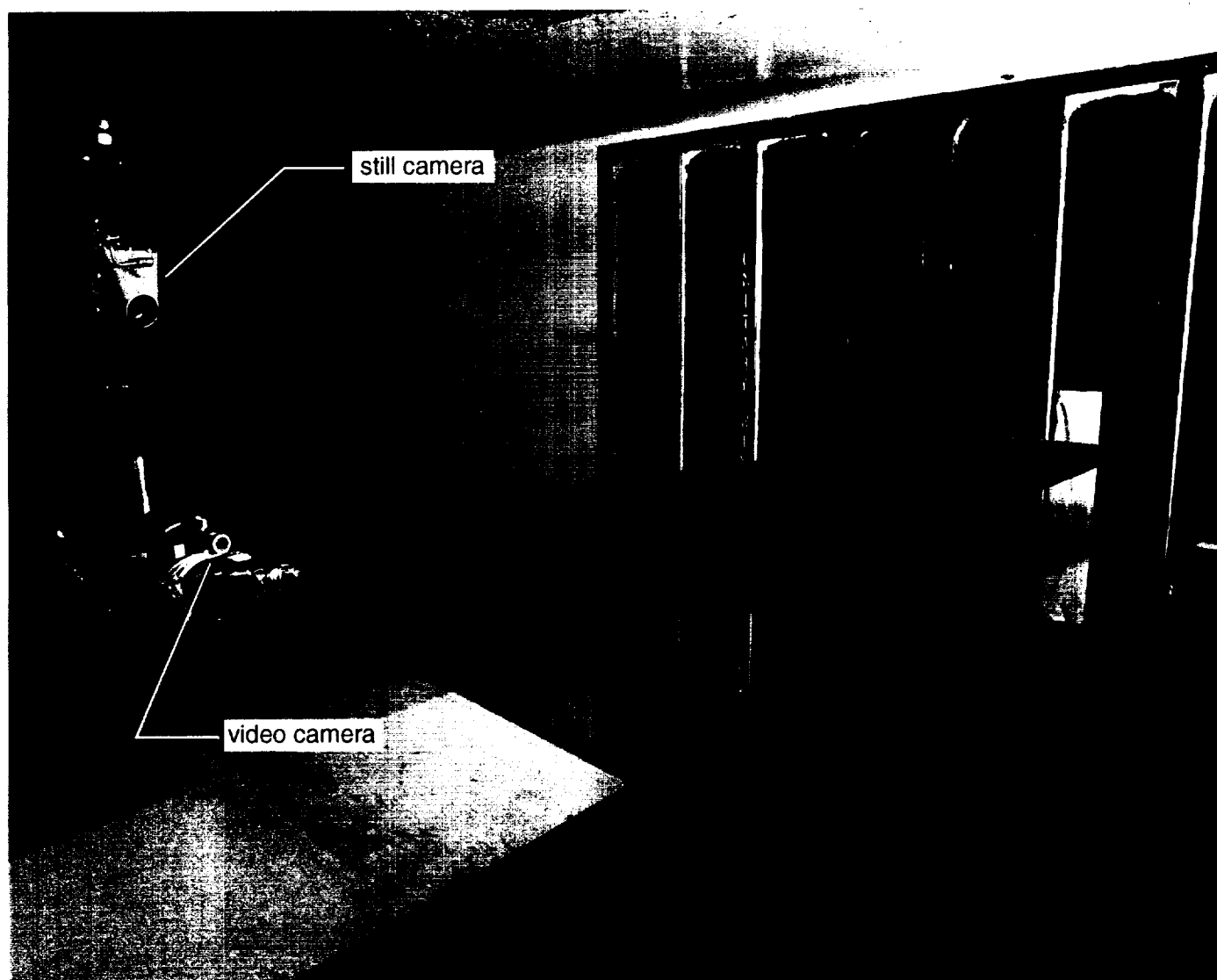


Figure 21. Photograph of wing-body missile model in the NASA LaRC UPWT (ref. 152)

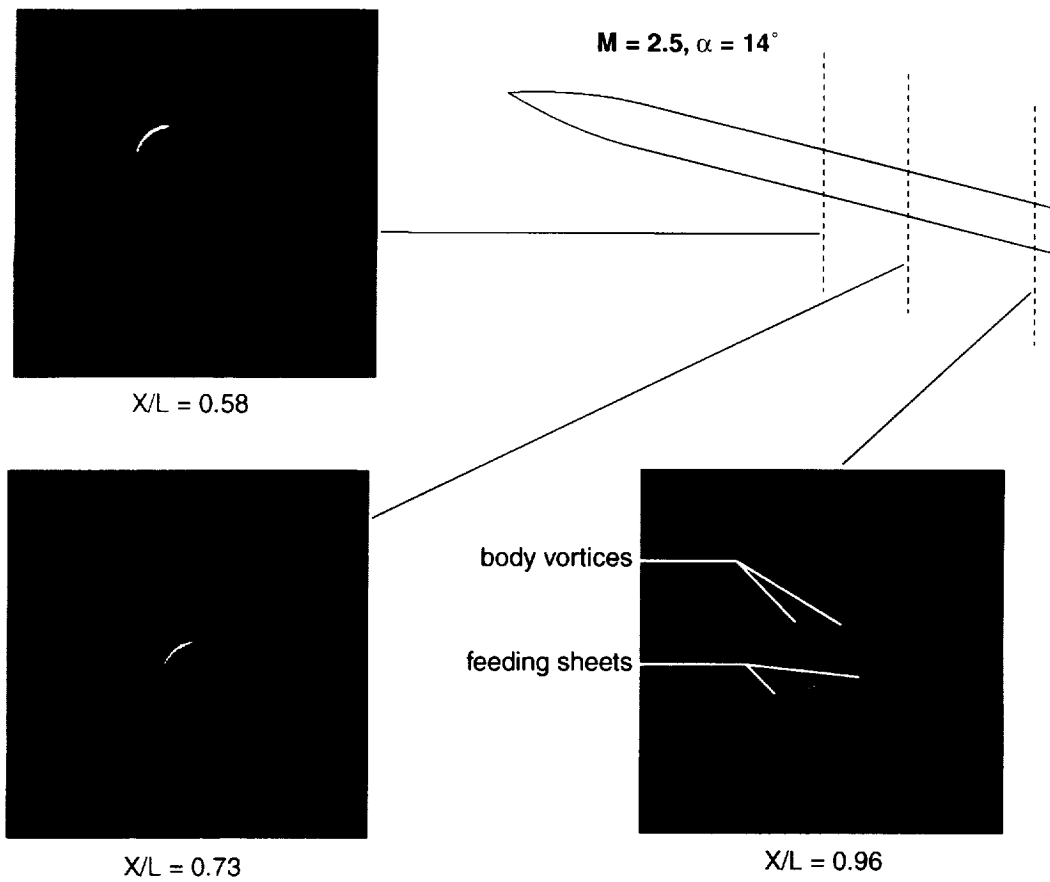


Figure 22. Vapor screen photographs showing the vortex development on body alone at  $M = 2.5$  and  $\alpha = 14^\circ$  (ref. 152)

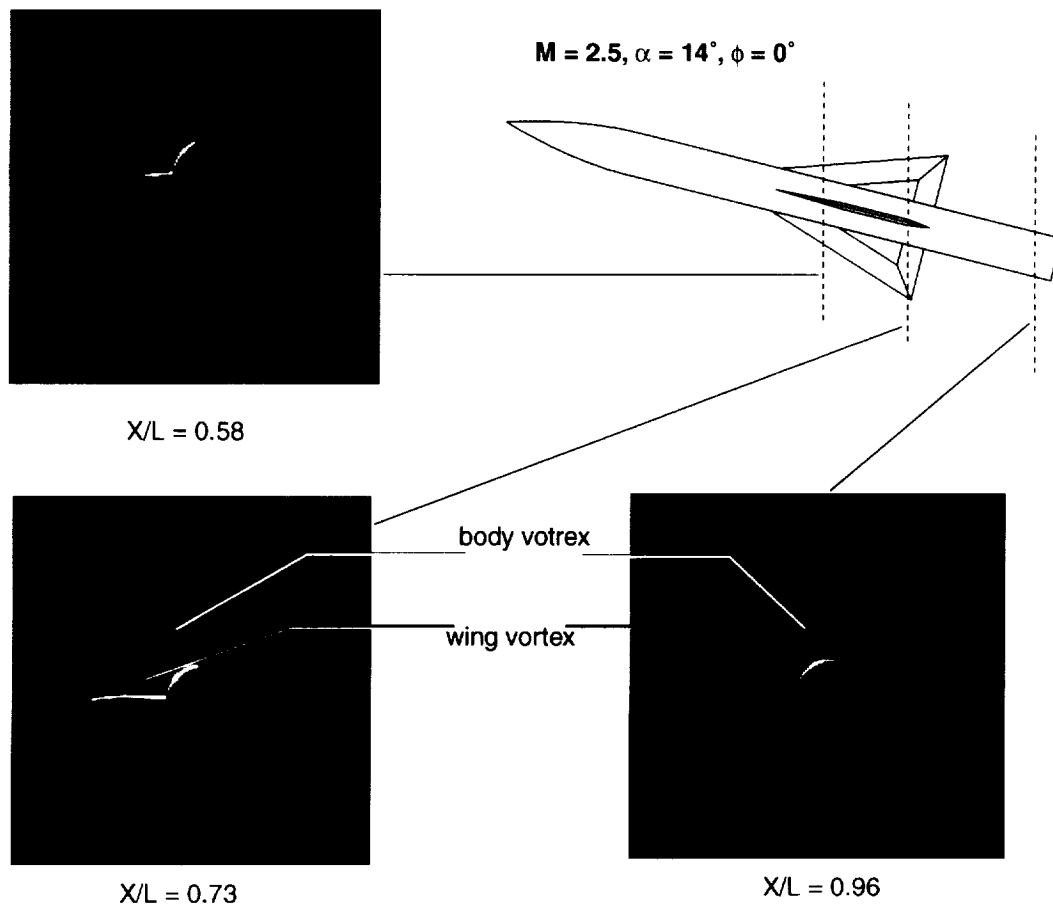


Figure 23. Vapor screen photographs showing the vortex development on body wing missile model at  $M = 2.5$  and  $\alpha = 14^\circ$  (ref. 152)

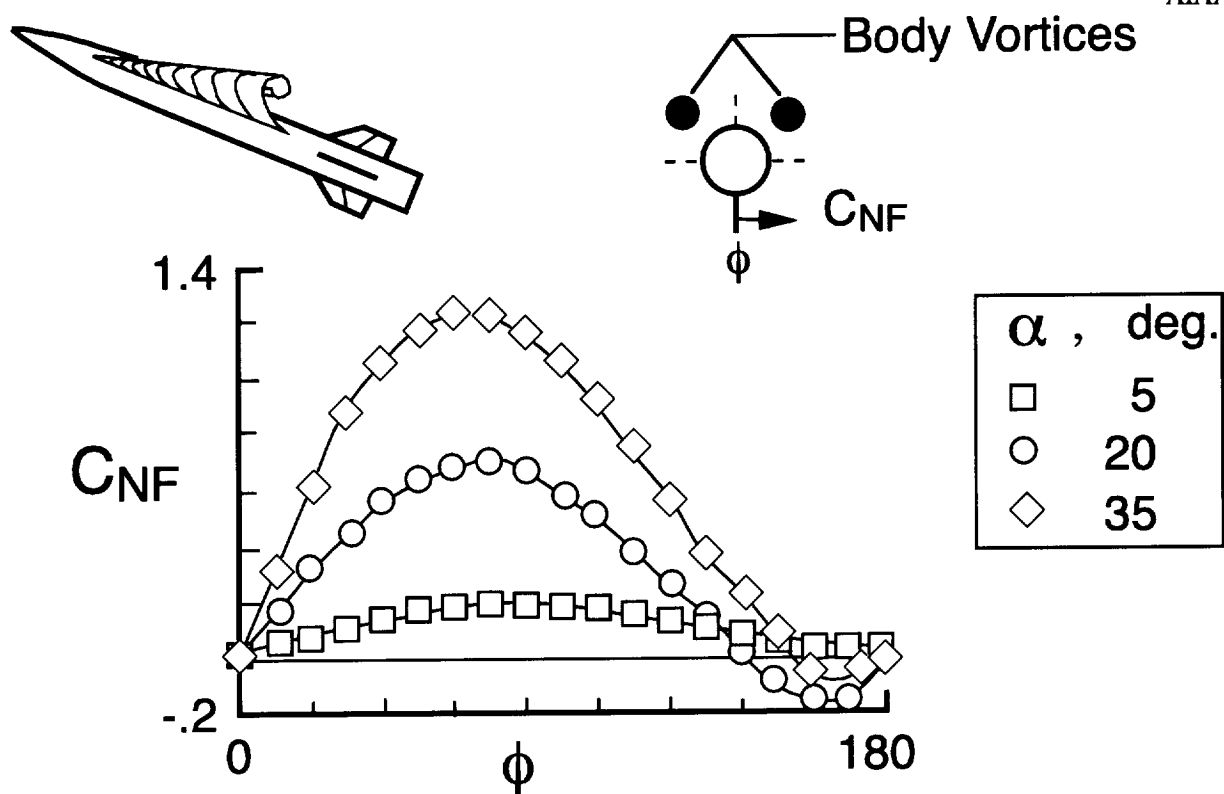


Figure 24. Plot of fin normal force coefficient as a function of fin roll position at  $M = 2.0$  (ref. 153)

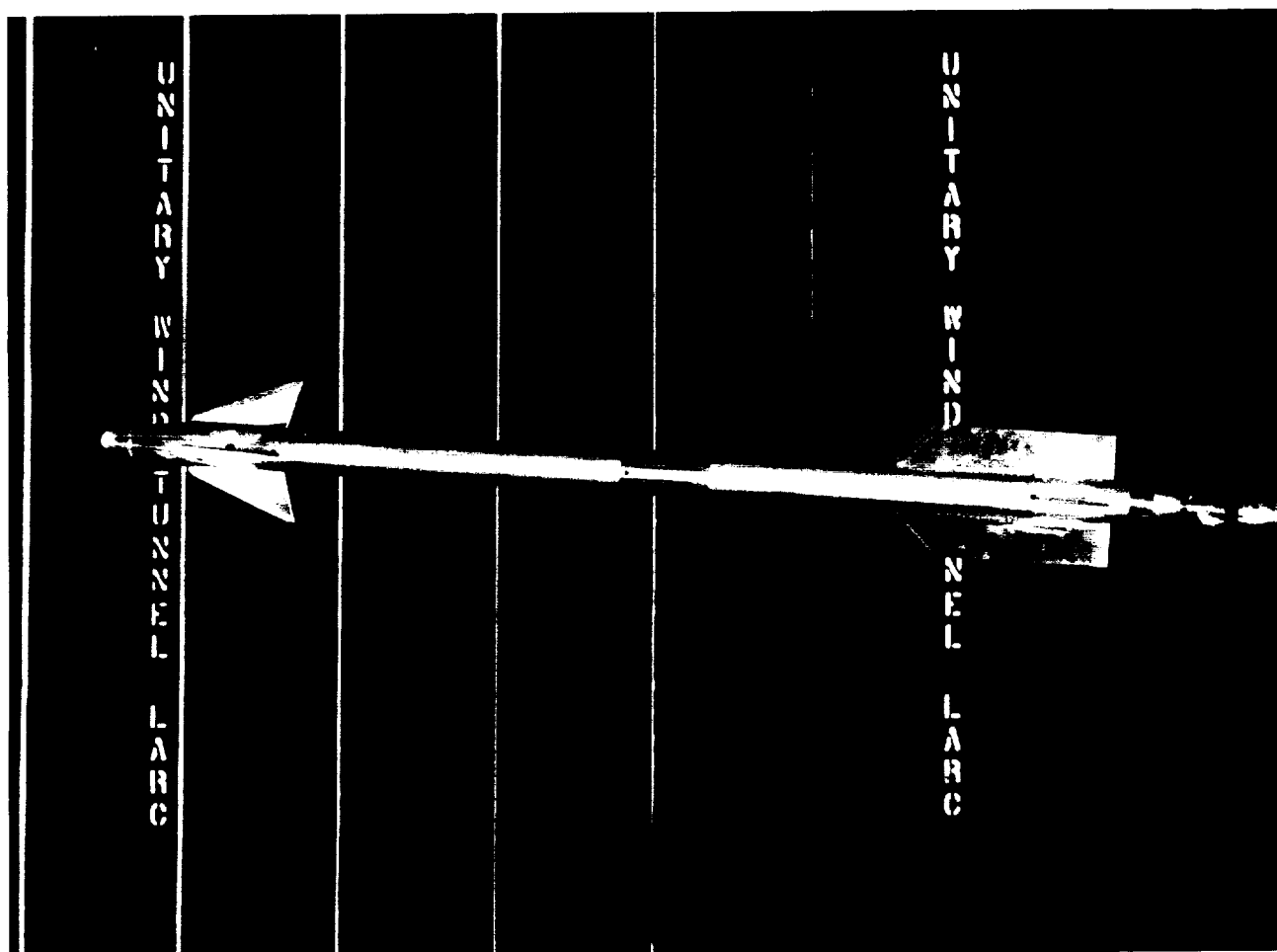


Figure 25. Photograph of a variant of Sidewinder missile model in the NASA LaRC UPWT (ref. 154)

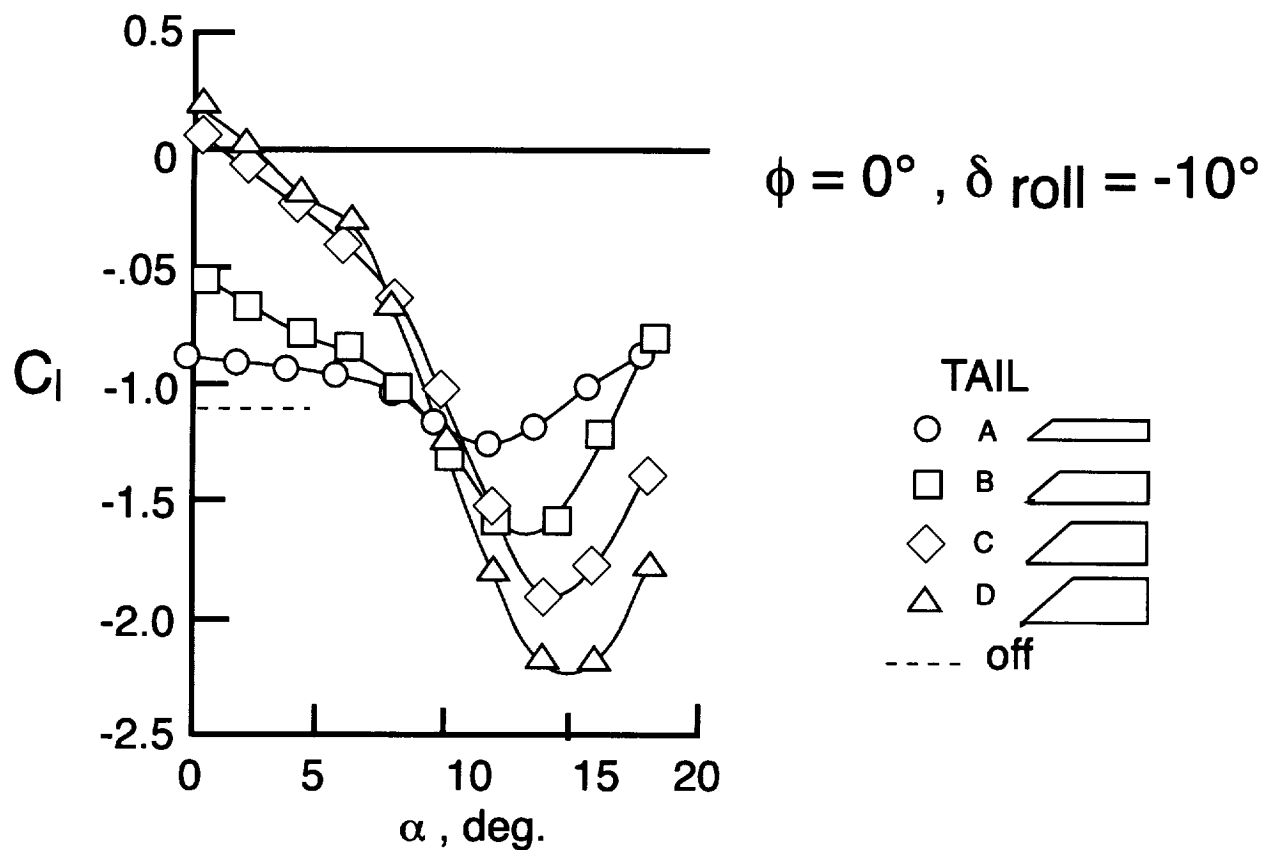


Figure 26. Effect of tail span on Sidewinder missile variant rolling moment at  $M = 2.5$  (ref. 154)

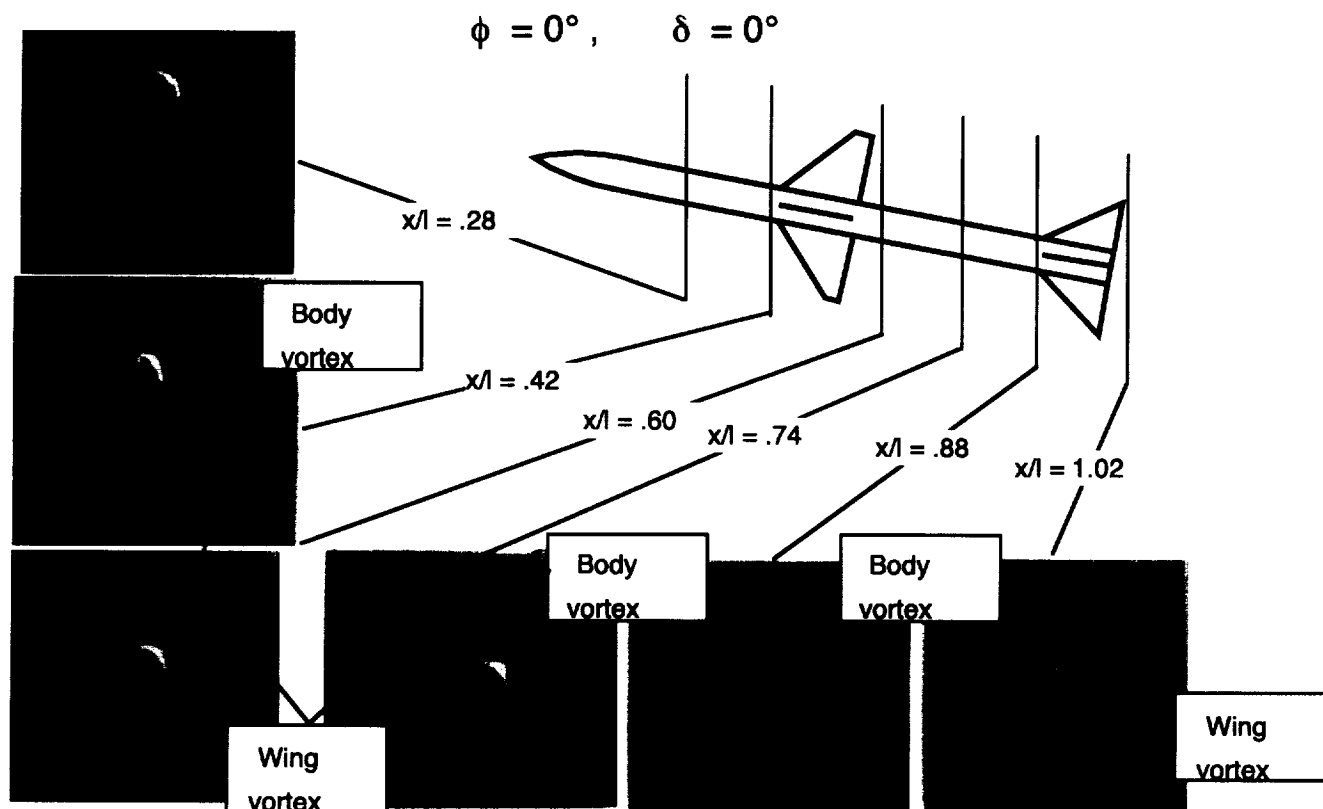


Figure 27. Vapor screen photographs showing the vortex development on a Sparrow missile at  $M = 2.36$  and  $\alpha = 11.4^\circ$  (ref. 154)

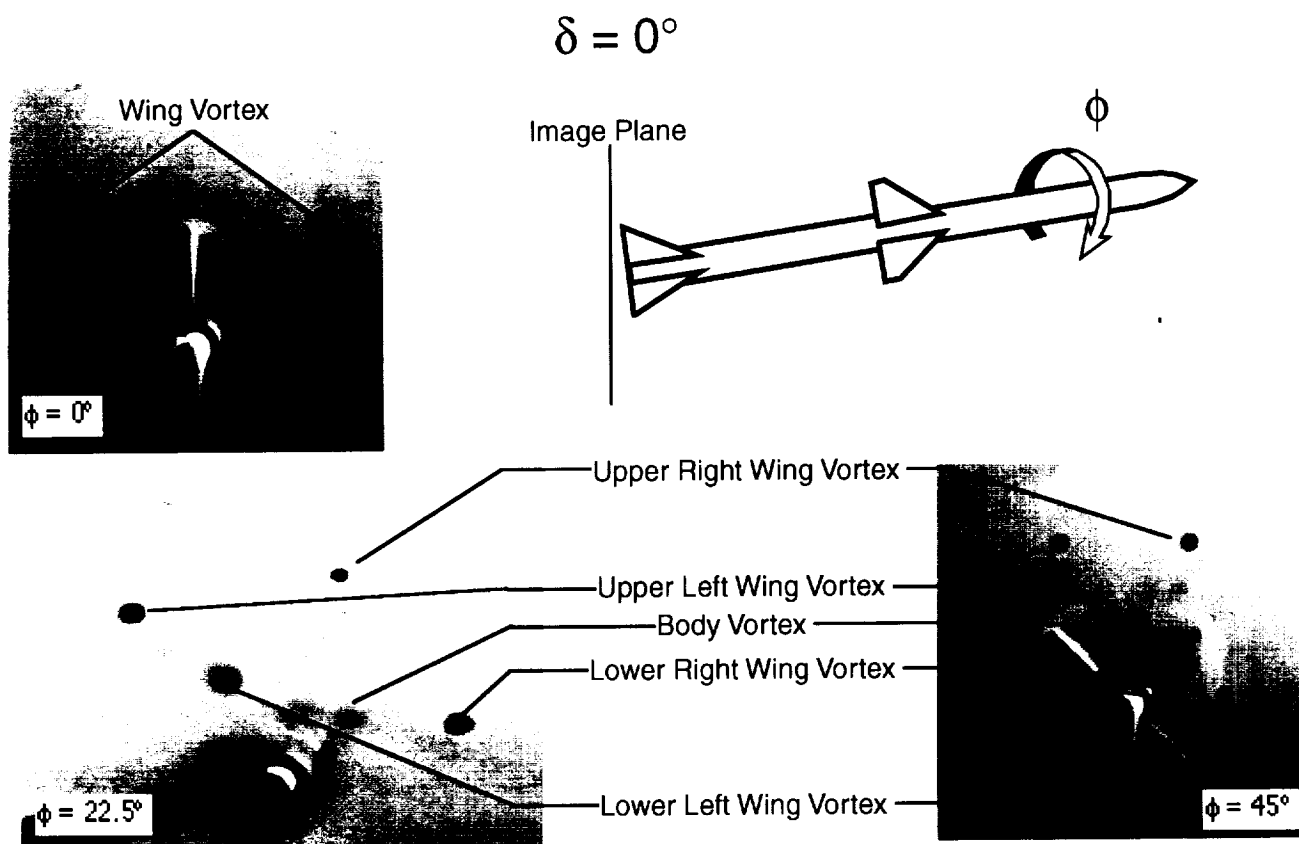


Figure 28. Vapor screen photographs showing the effect of roll angle on vortex patterns for the Sparrow missile at  $M = 2.36$  and  $\alpha = 11.4^\circ$  (ref. 116)

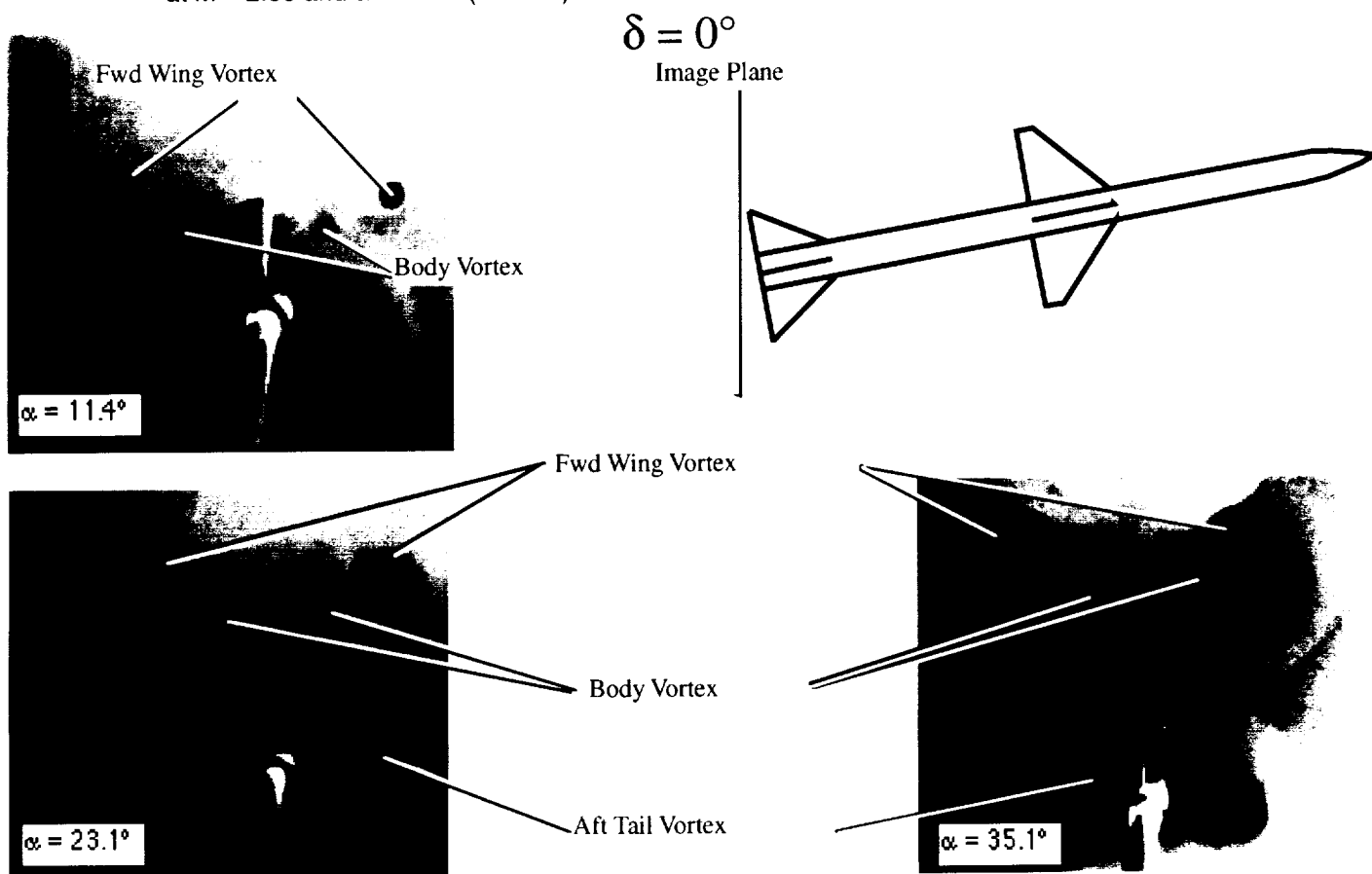


Figure 29. Vapor screen photographs showing the effect of angle of attack on Sparrow missile vortex patterns at  $M = 2.36$  and  $\phi = 0.0^\circ$  (ref. 116)

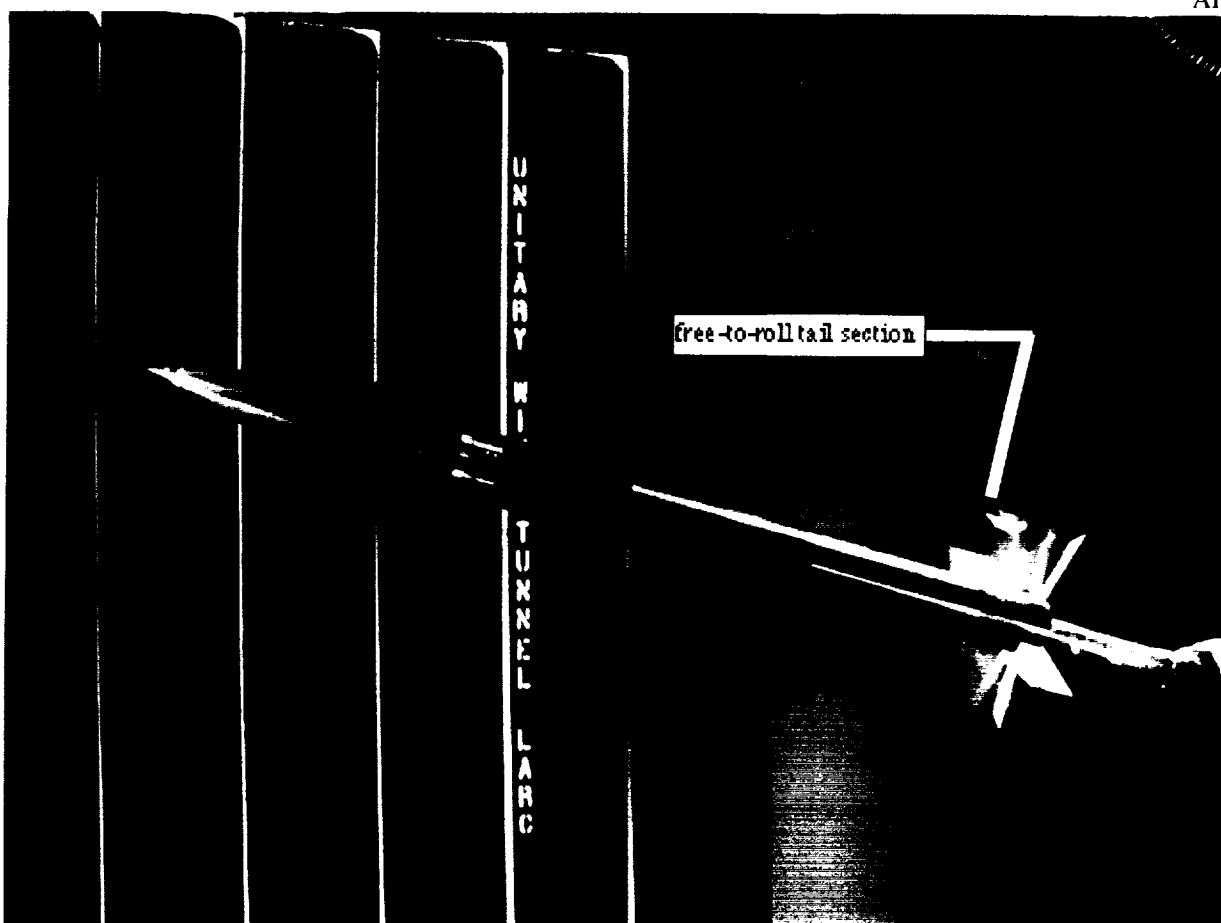


Figure 30. Photograph of the Free Rolling Tail missile model in the NASA LaRC UPWT (ref. 155).

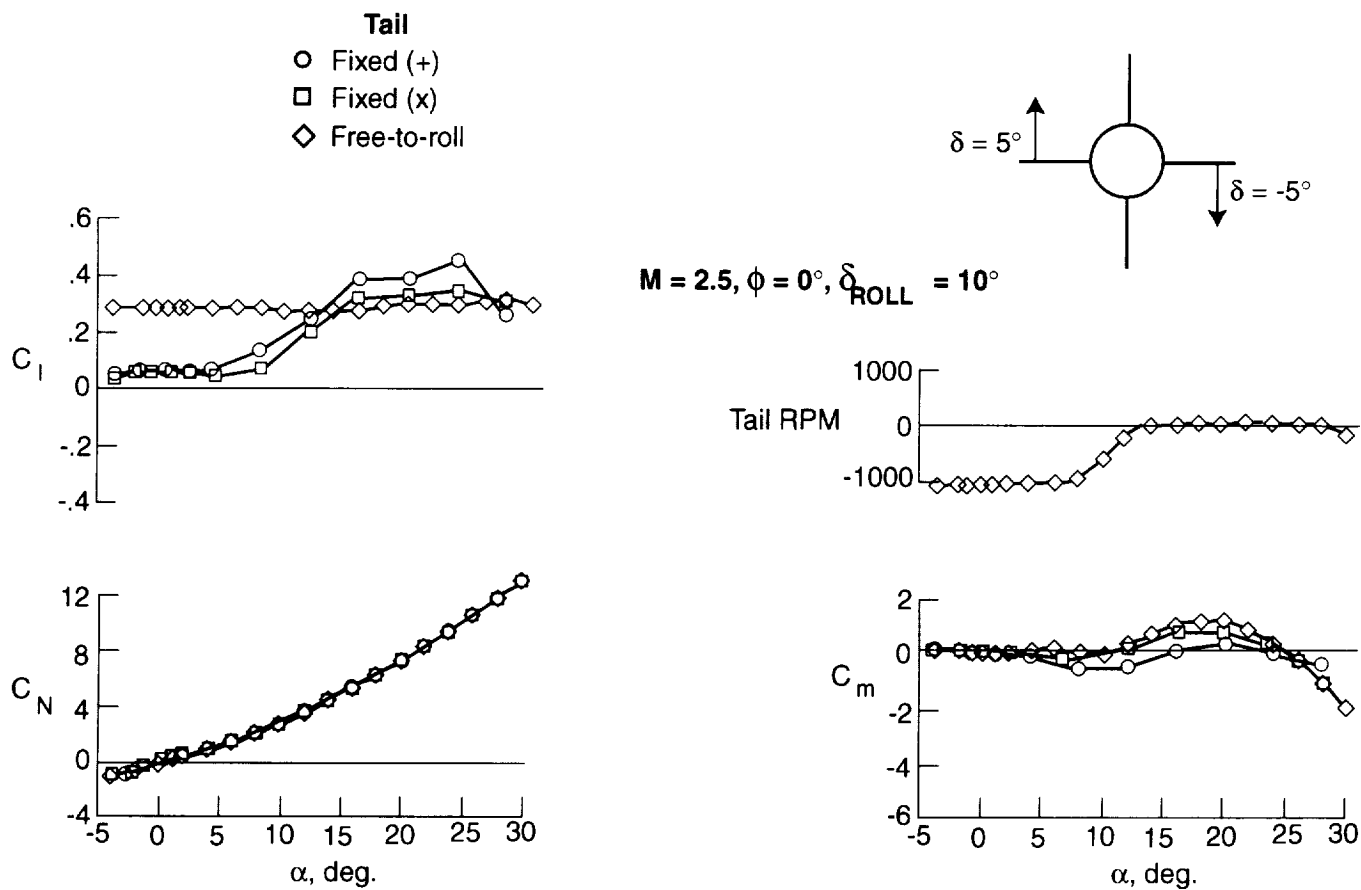


Figure 31. Effects of free rolling tail on roll control at  $M = 2.5$  (ref. 155)

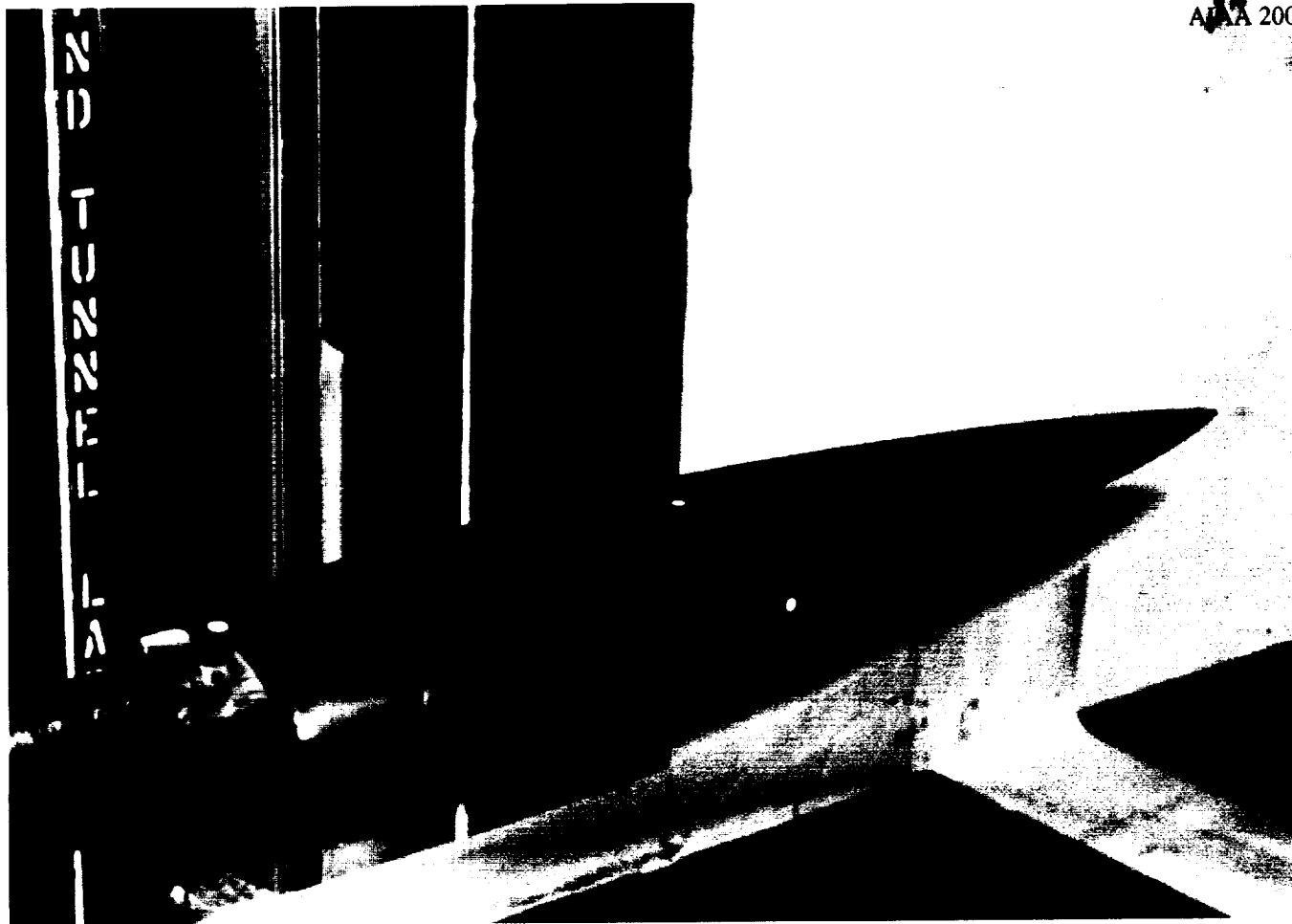


Figure 32. Photograph of sharp-nose 3-to-1 elliptical body model in the NASA LaRC UPWT (ref. 117)

$$M = 2.50, \alpha = 20^\circ$$

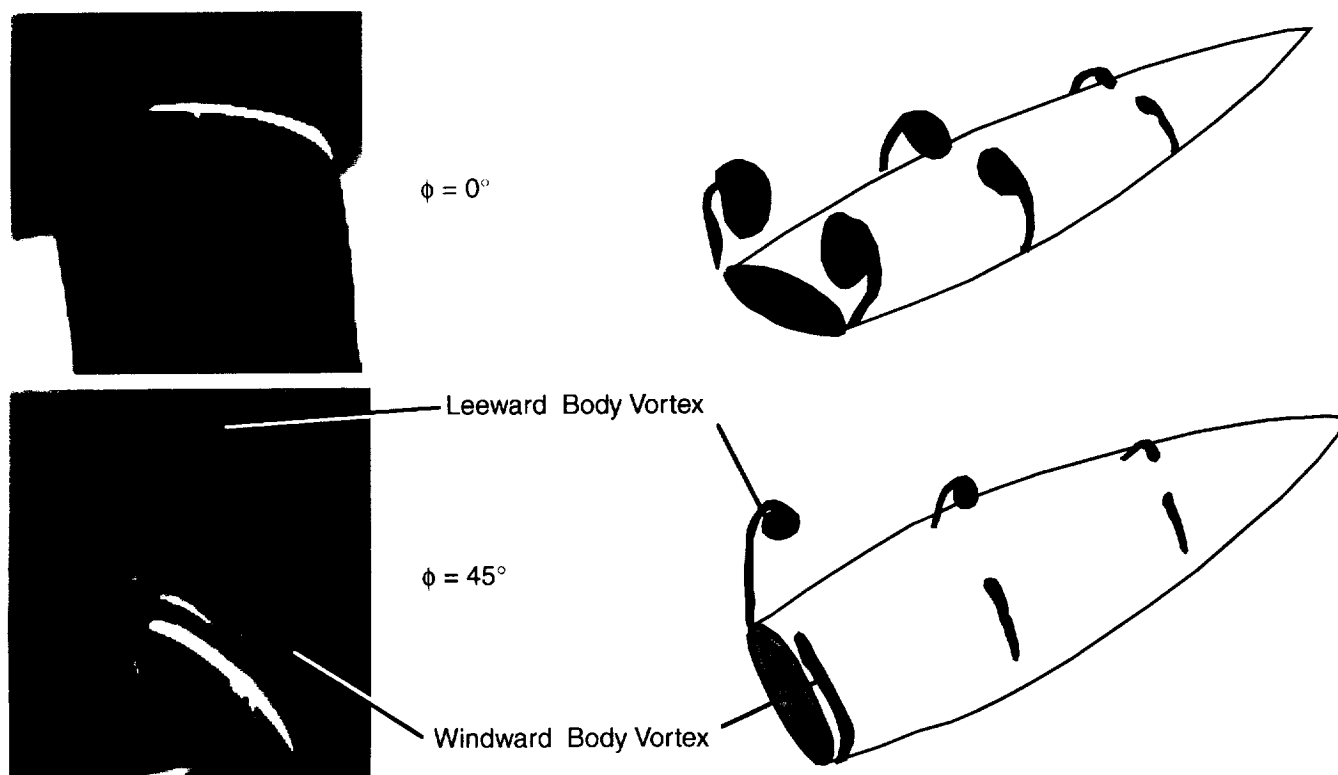


Figure 33. Vapor screen photographs showing the effect of roll angle on vortex patterns for the sharp-nose elliptical body at  $M = 2.5$  and  $\alpha = 20^\circ$  (ref. 117)

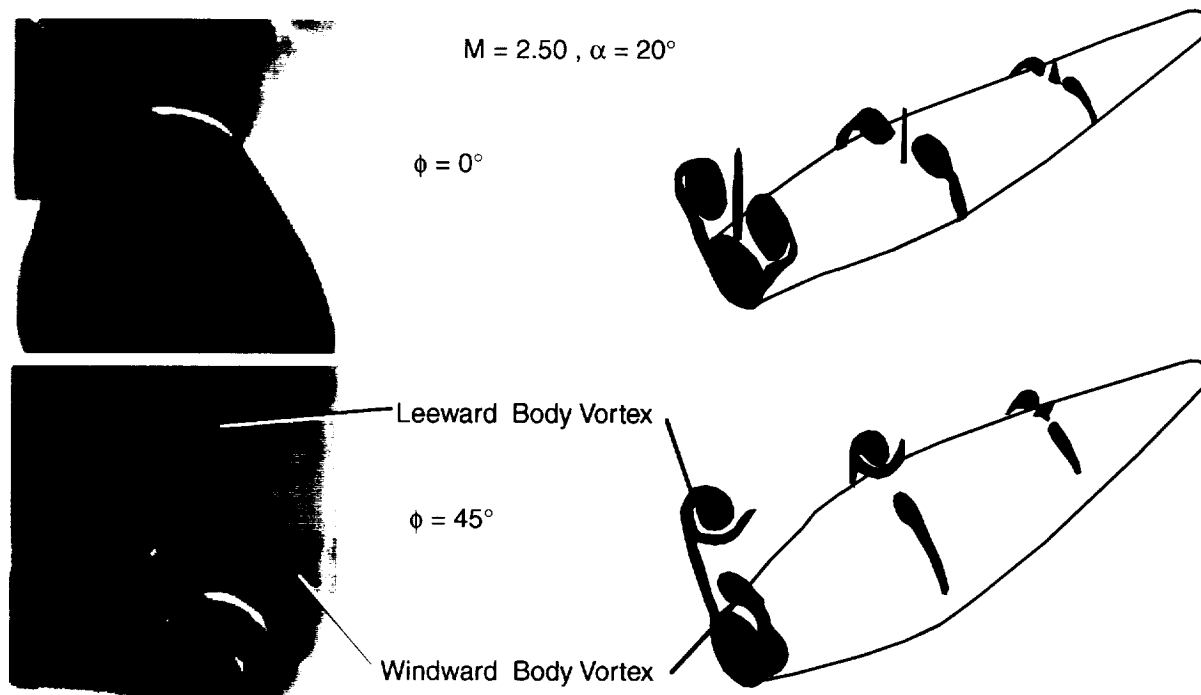


Figure 34. Vapor screen photographs showing the effect of roll angle on vortex patterns for the blunt-nose elliptical body at  $M = 2.5$  and  $\alpha = 20^\circ$  (ref. 117)

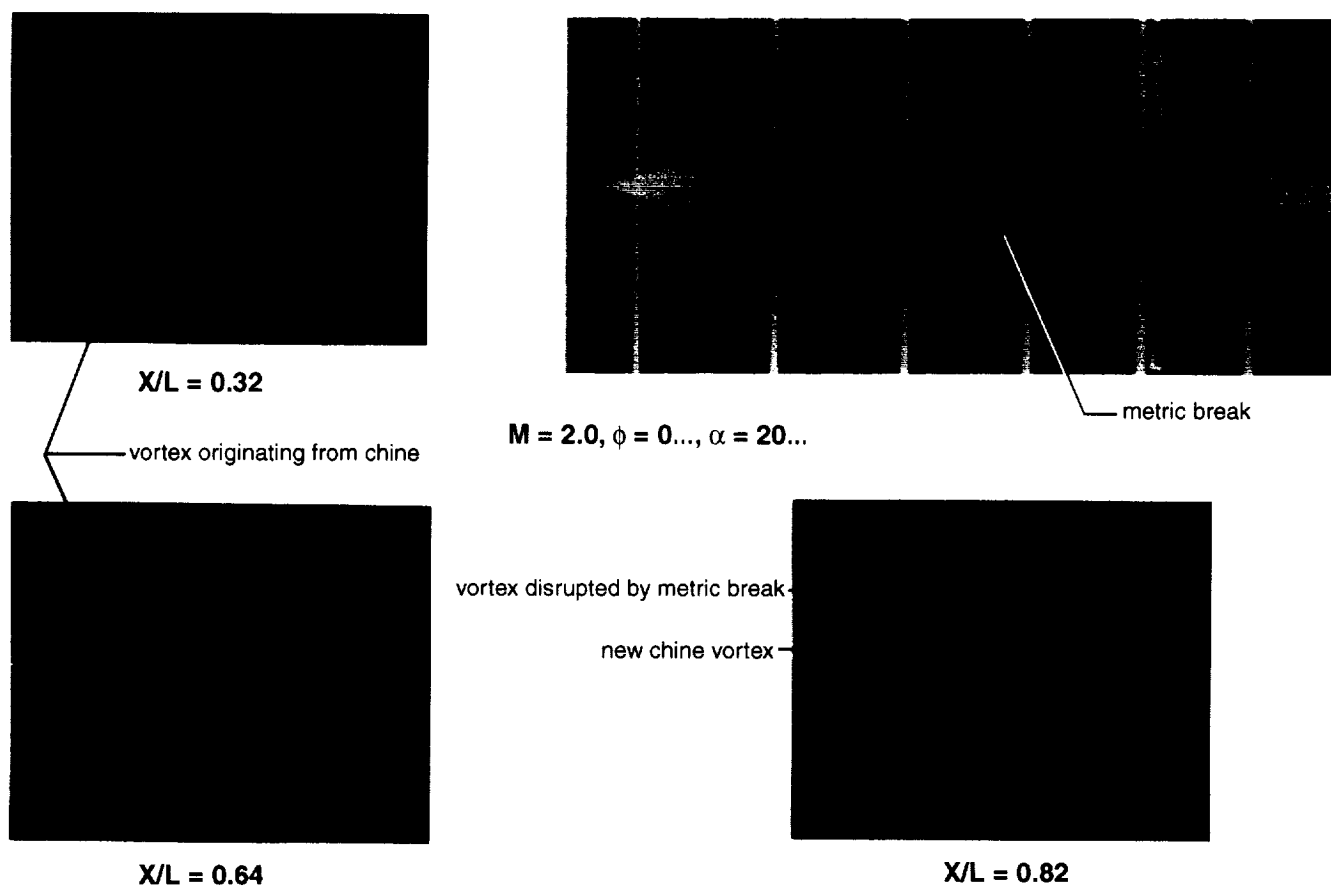


Figure 35. Vapor screen photographs showing the vortex patterns on a chined body at  $M = 2.0$  and  $\alpha = 20^\circ$  (ref. 138)

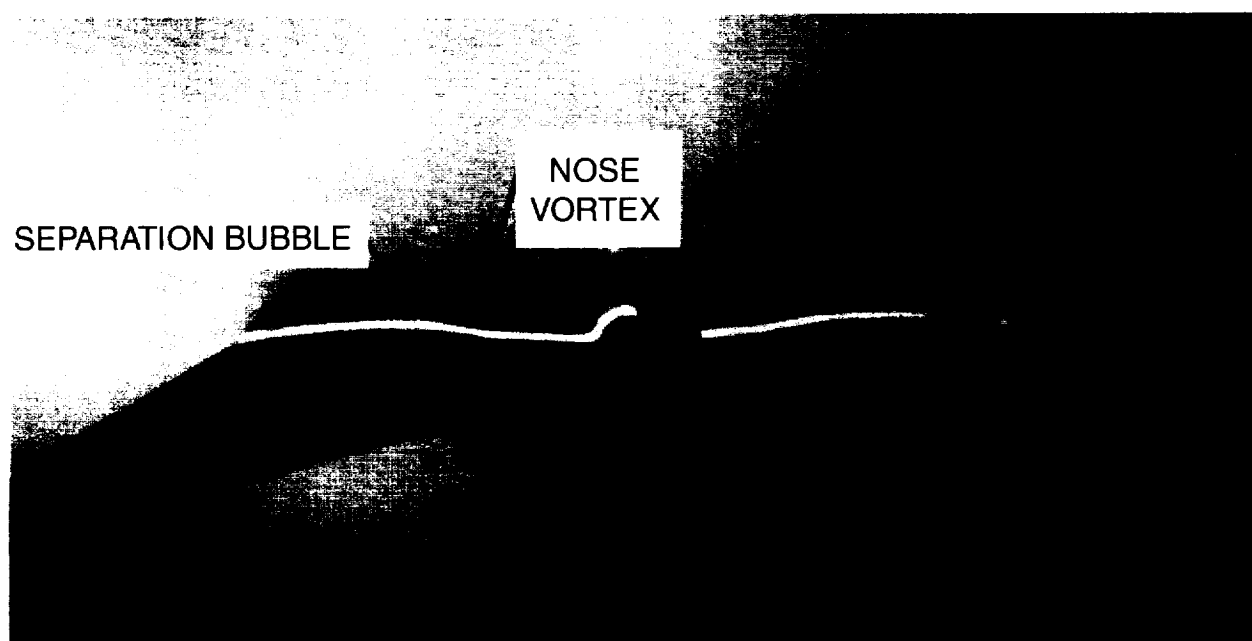

 $x/L = 0.76$ 

Figure 36. Lee-side flow characteristics for ogee planform wing at Mach 2.4 and angle-of-attack of  $5^\circ$  (ref. 158).

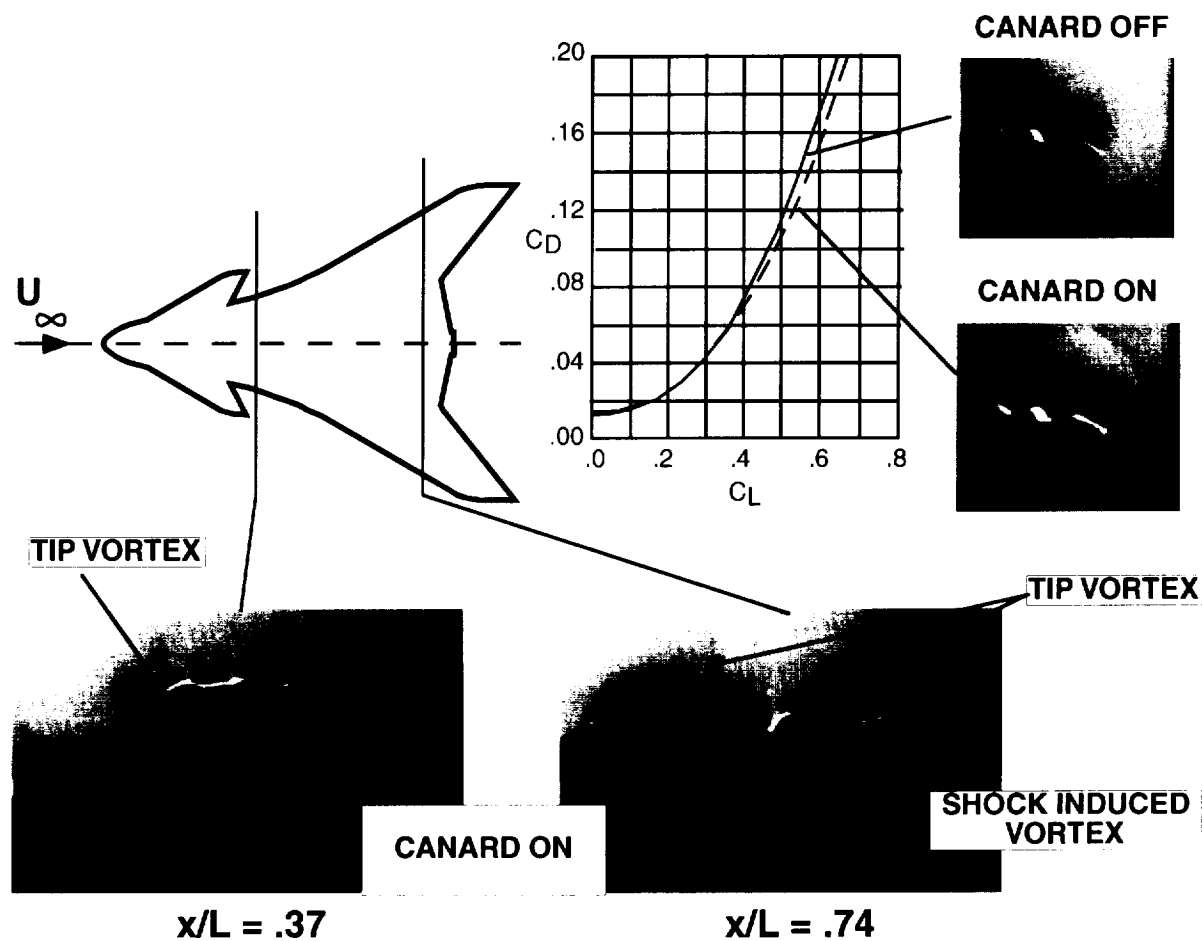


Figure 37. Lee-side flow characteristics for ogee planform wing with canard at Mach 1.8 and angle-of-attack of  $12^\circ$  (ref. 166).

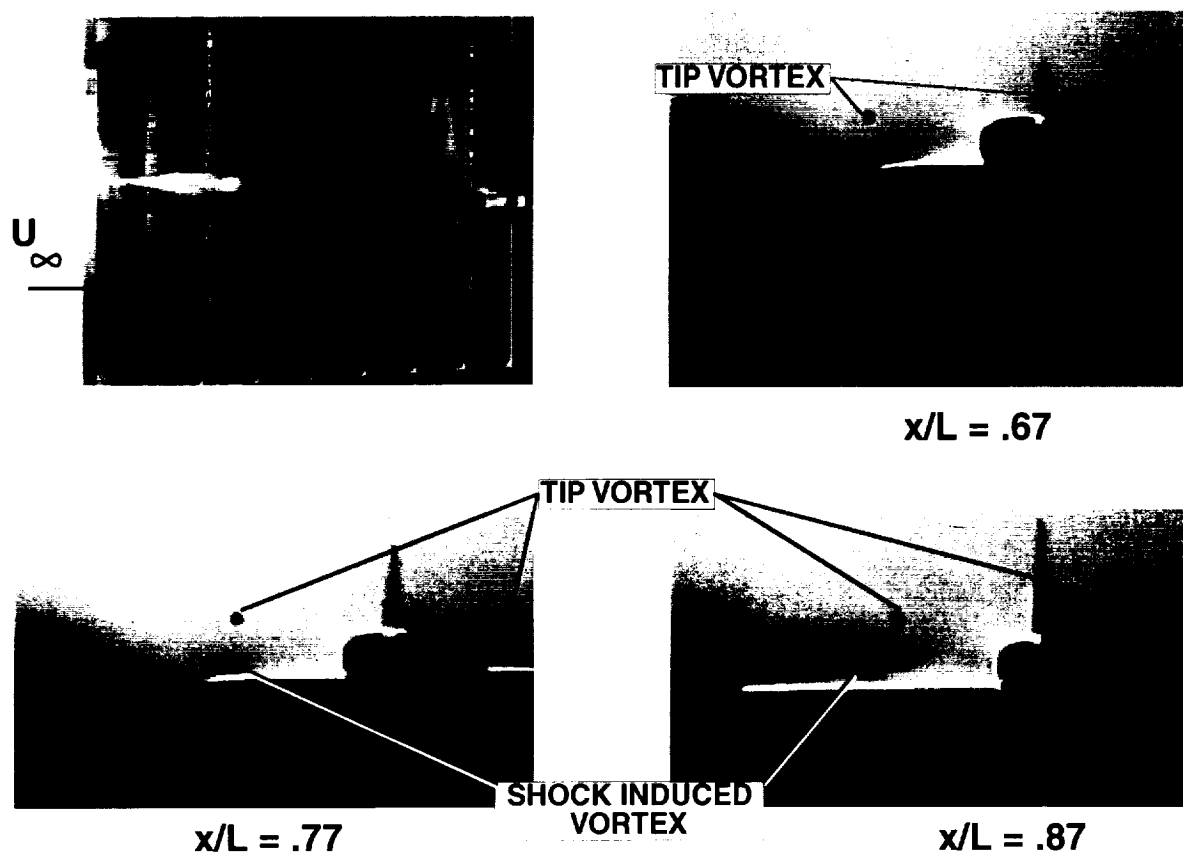


Figure 38. Lee-side flow characteristics for cranked delta planform wing with canard at Mach 1.8 and angle-of-attack of  $7^\circ$  (ref. 167).

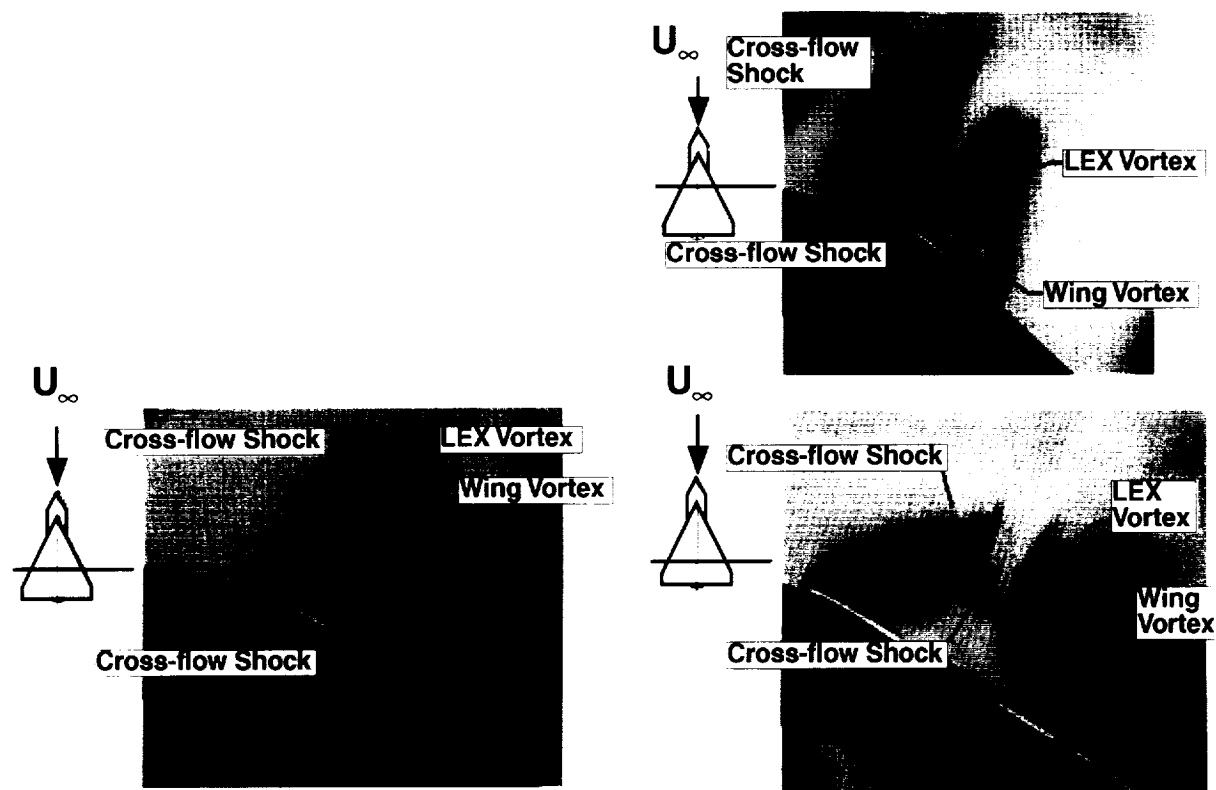


Figure 39. Lee-side flow characteristics for stake delta planform wing with strake at Mach 1.6 and angle-of-attack of  $24^\circ$  (ref. 160).

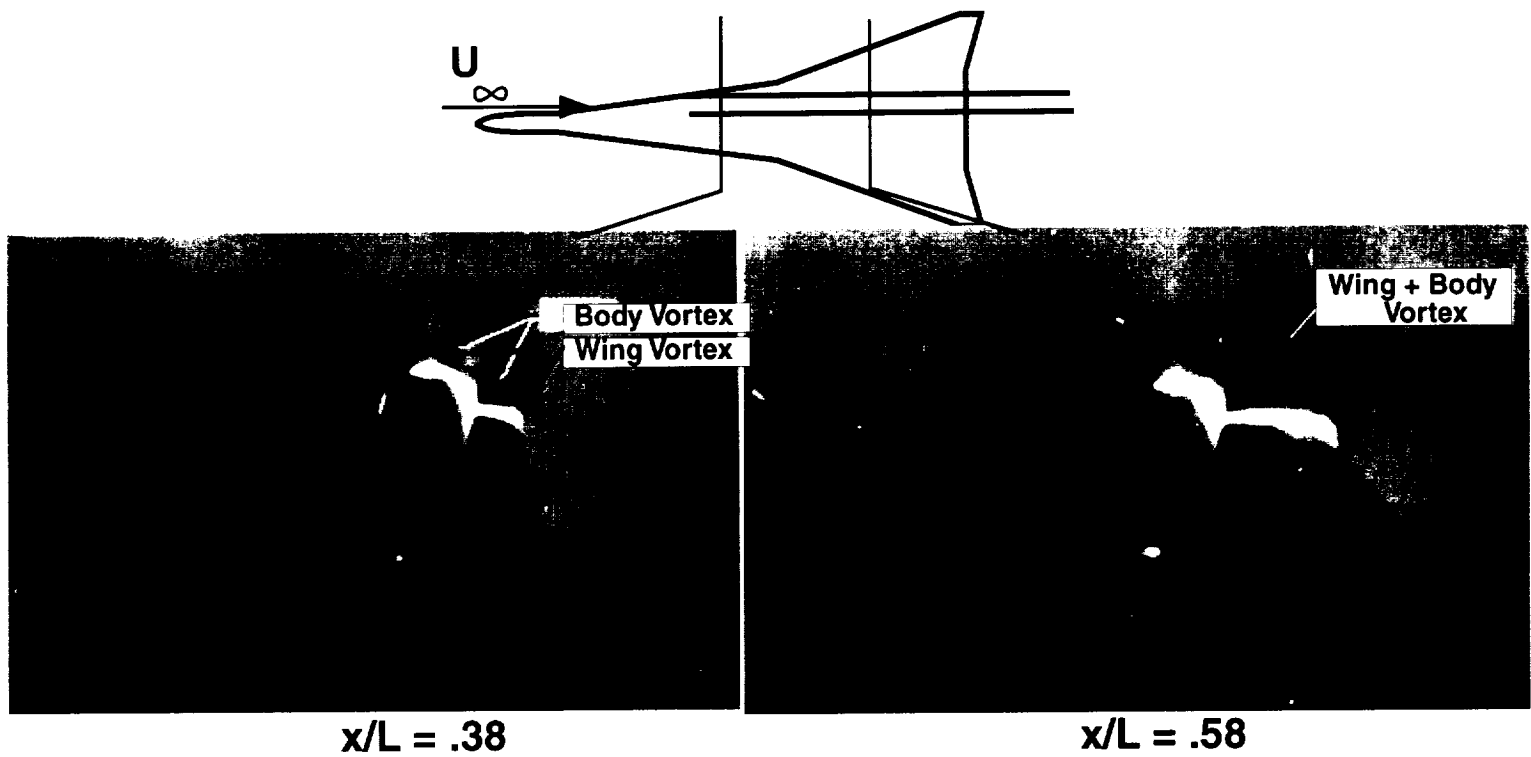


Figure 40. Lee-side flow characteristics for delta planform wing with strake and body at Mach 3.5 and angle-of-attack of  $10^\circ$  (ref. 161).

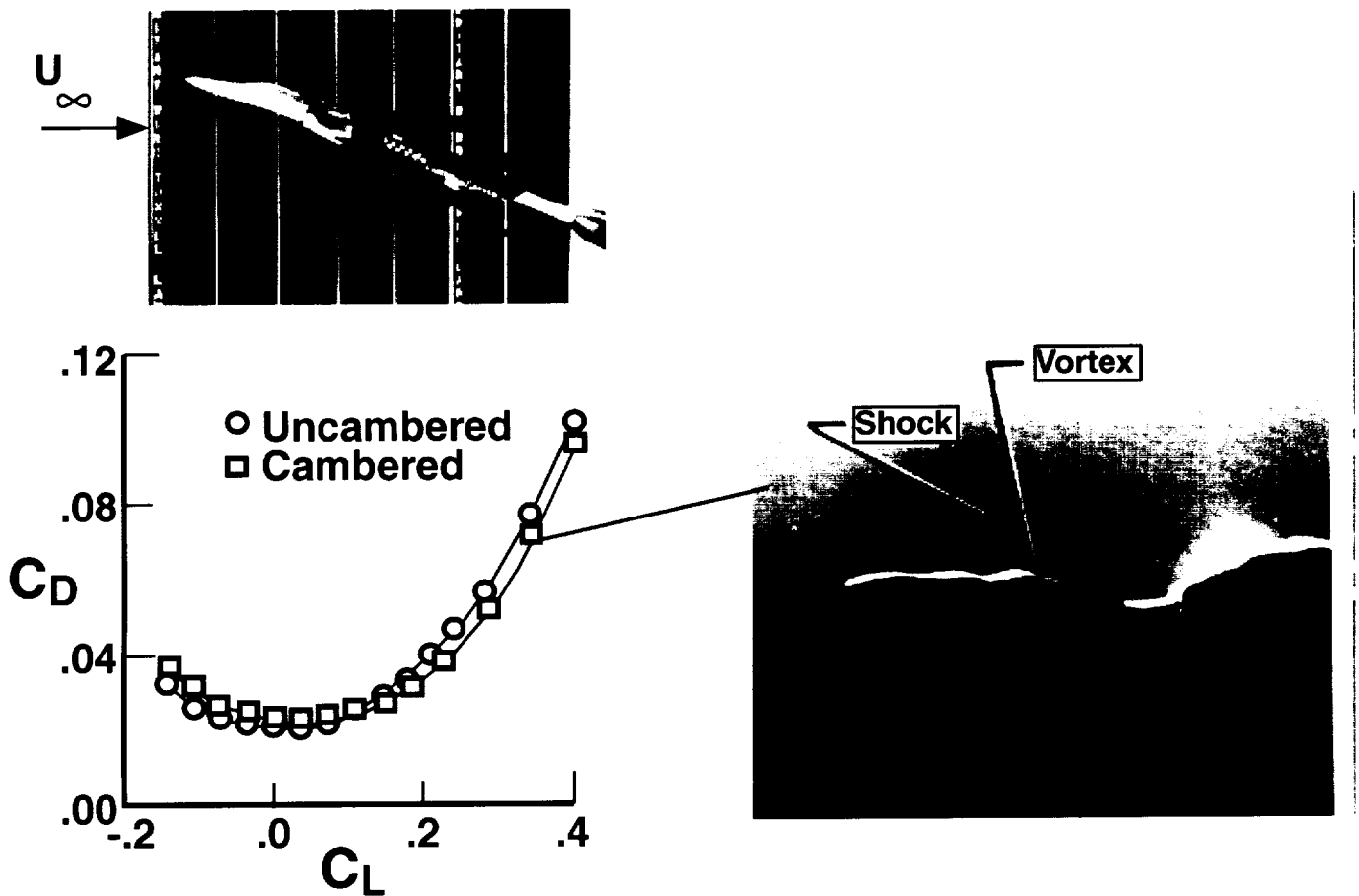


Figure 41. Lee-side flow characteristics for cranked arrow planform wing with body at Mach 1.8 and angle-of-attack of  $10^\circ$  (ref. 168).

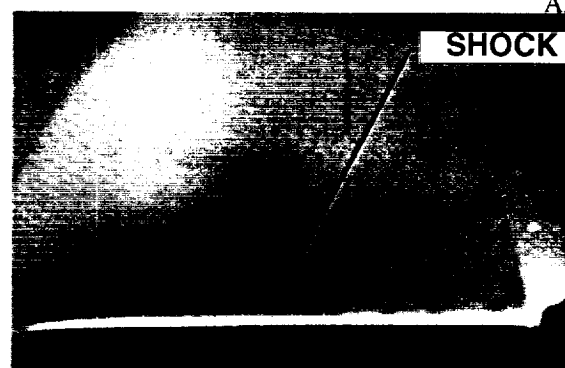
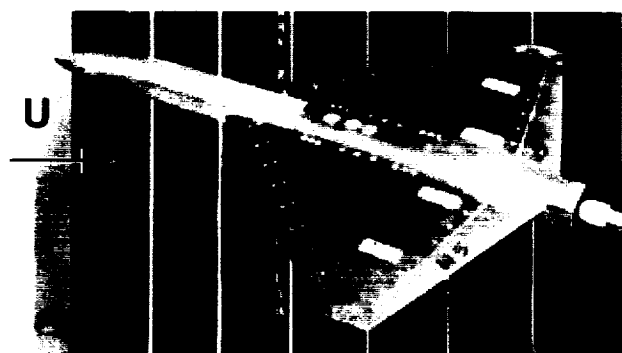
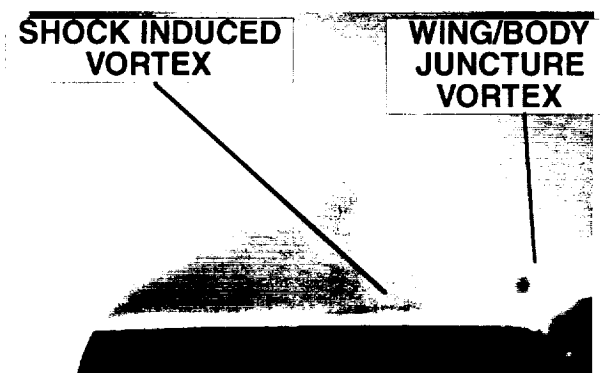
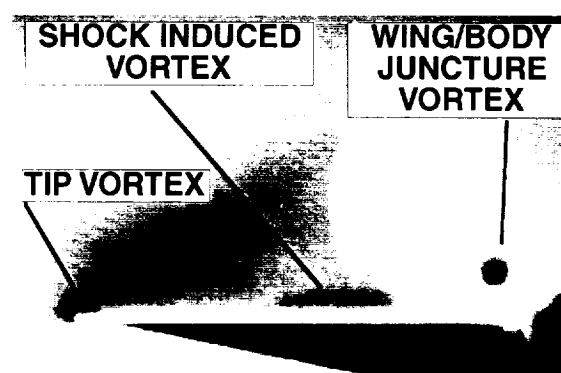
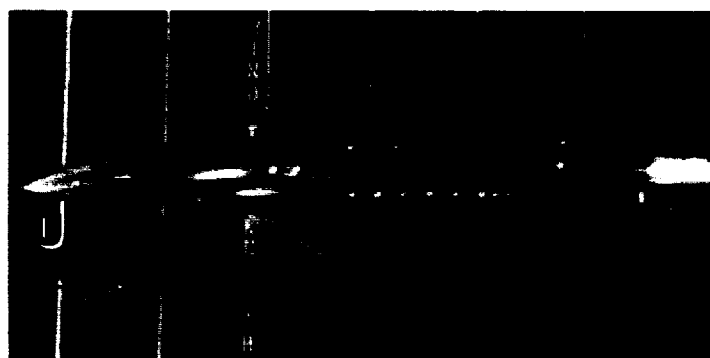

 $C_L = 0.2$ 

 $C_L = 0.3$ 

 $C_L = 0.4$ 

Figure 42. Lee-side flow characteristics for delta planform wing with body at Mach 2.16 (ref. 157).


 $x/L = .3$ 

 $x/L = .9$ 

Figure 43. Lee-side flow characteristics for delta planform wing with body at Mach 1.6 and angle-of-attack of  $12^\circ$  (ref. 162).

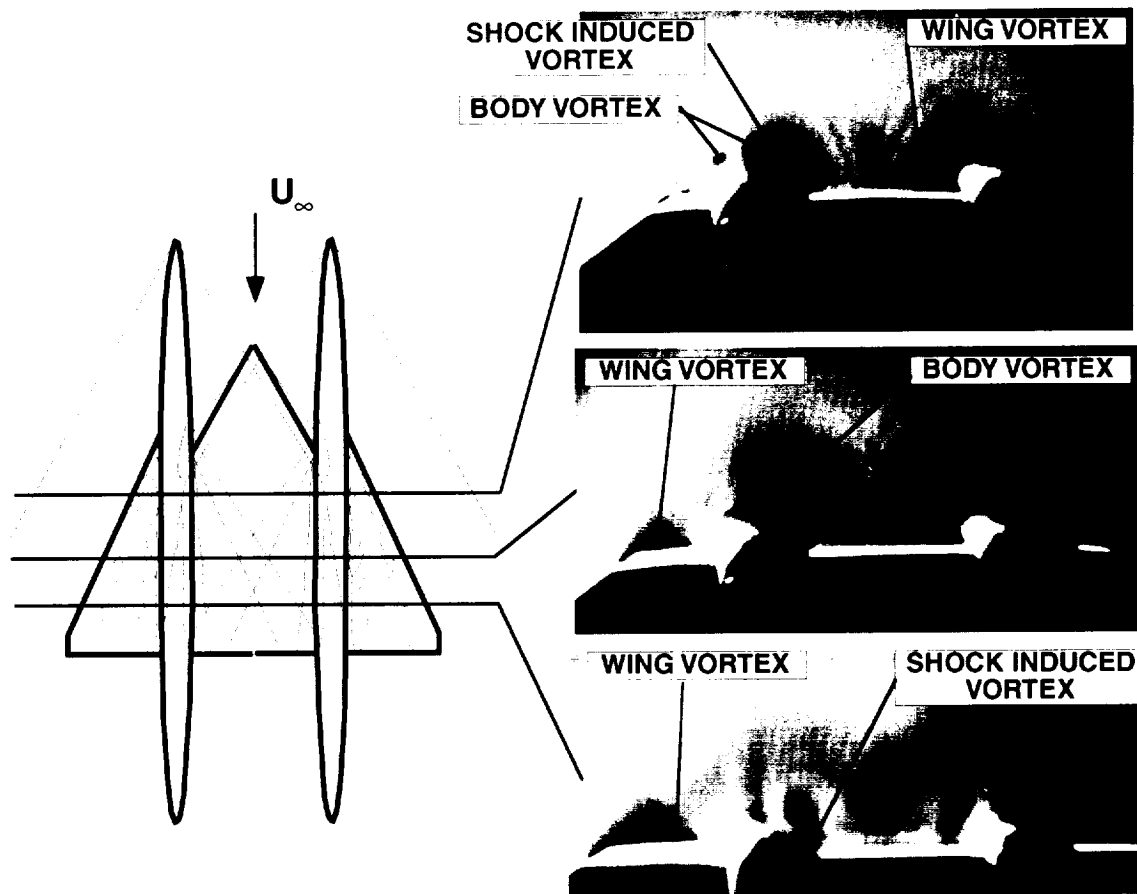


Figure 44. Lee-side flow characteristics for delta planform wing with multiple bodies at Mach 2.16 and angle-of-attack of  $16^\circ$  (ref. 163).

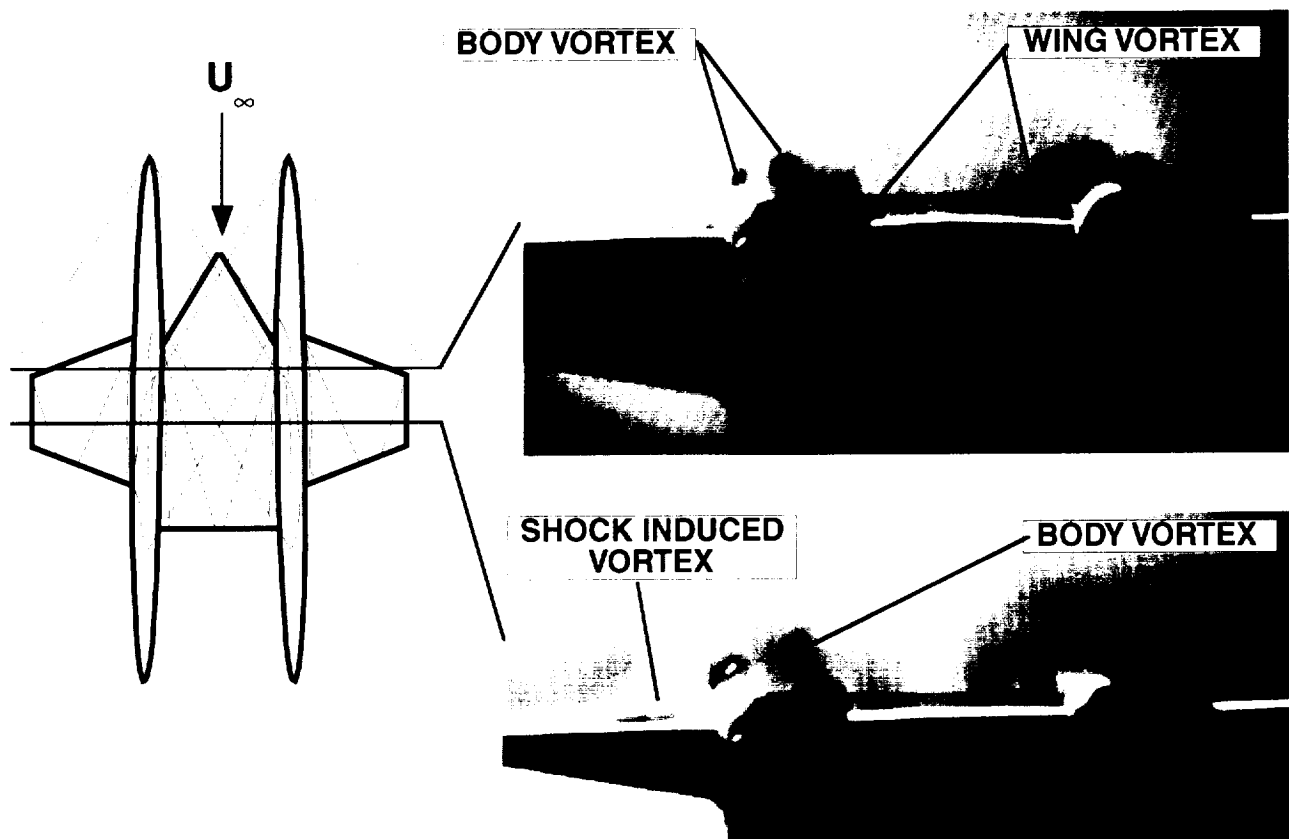
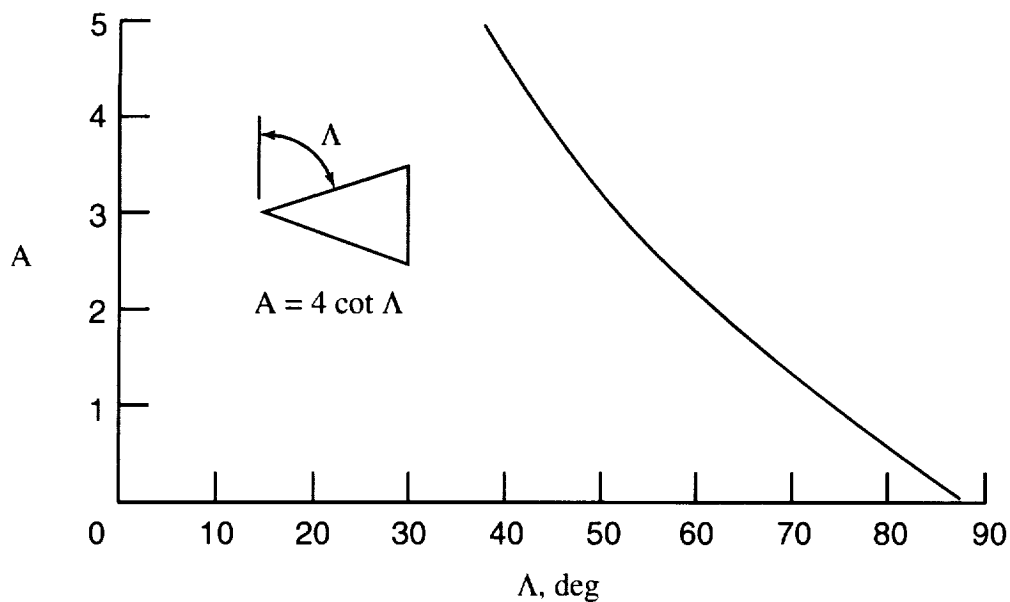


Figure 45. Lee-side flow characteristics for trapezoidal planform wing with multiple bodies at Mach 2.16 and angle-of-attack of  $16^\circ$  (ref. 163).



(a) Aspect ratio and wing leading edge sweep.

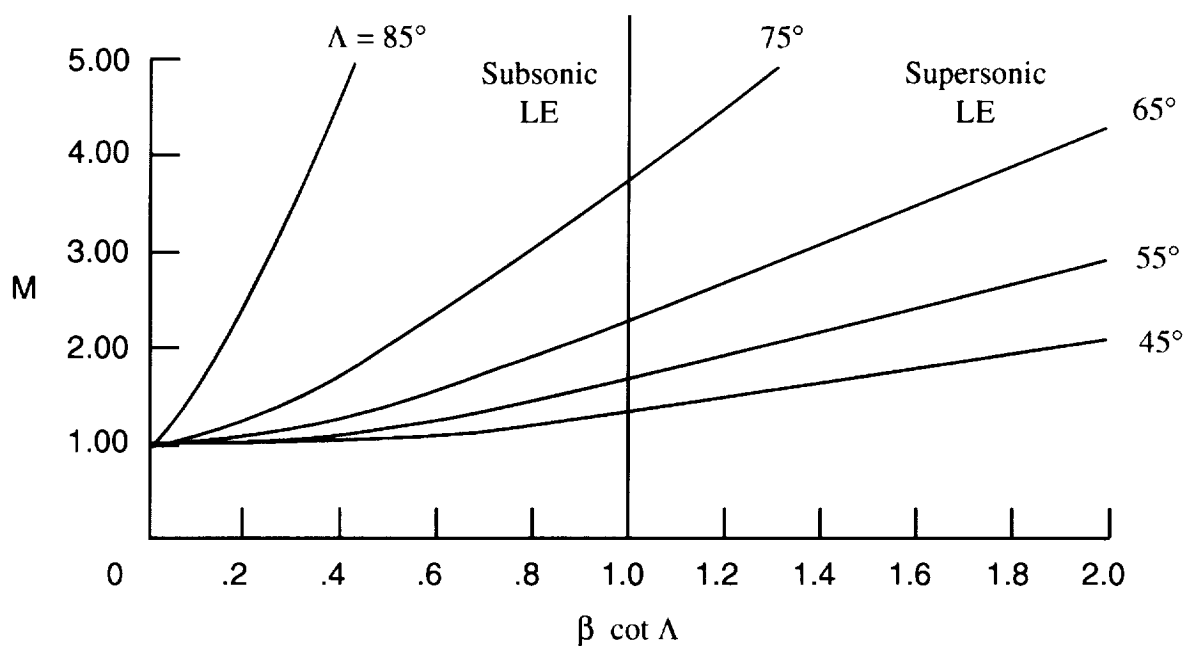
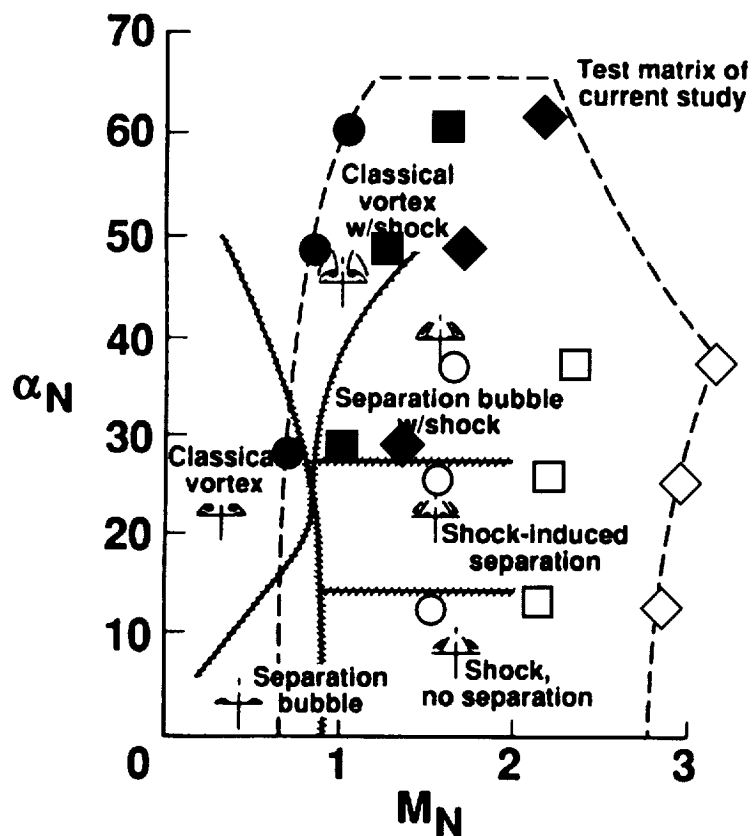
(b) Mach number and  $\beta \cot \Lambda$ .

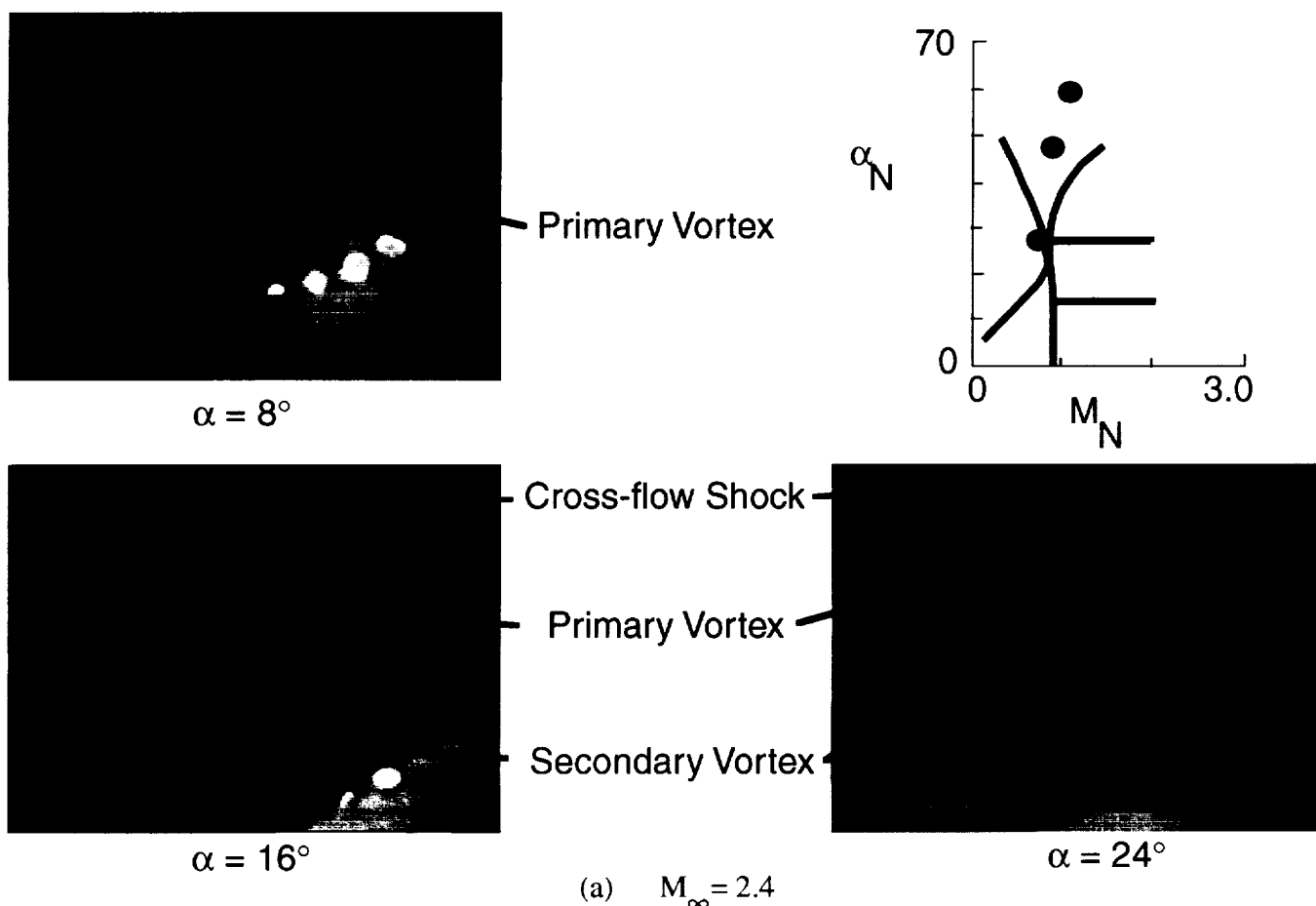
Figure 46. Correlation parameters for delta wings (ref. 182).





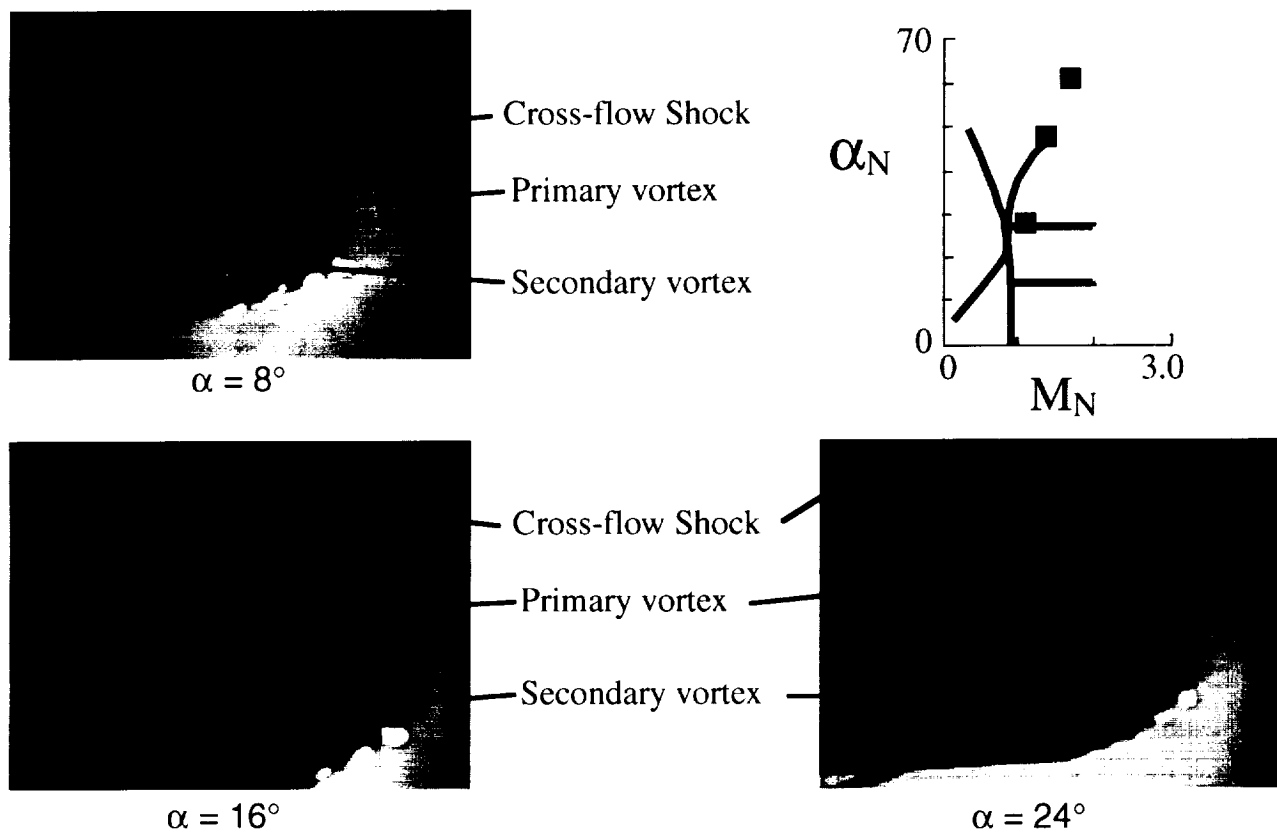
Delta Wing		Mach
75°	52.5°	
●	○	2.4
■	□	3.4
◆	◇	4.6

Figure 49. Sketch showing  $M_N$  and  $\alpha_N$  conditions of test points.

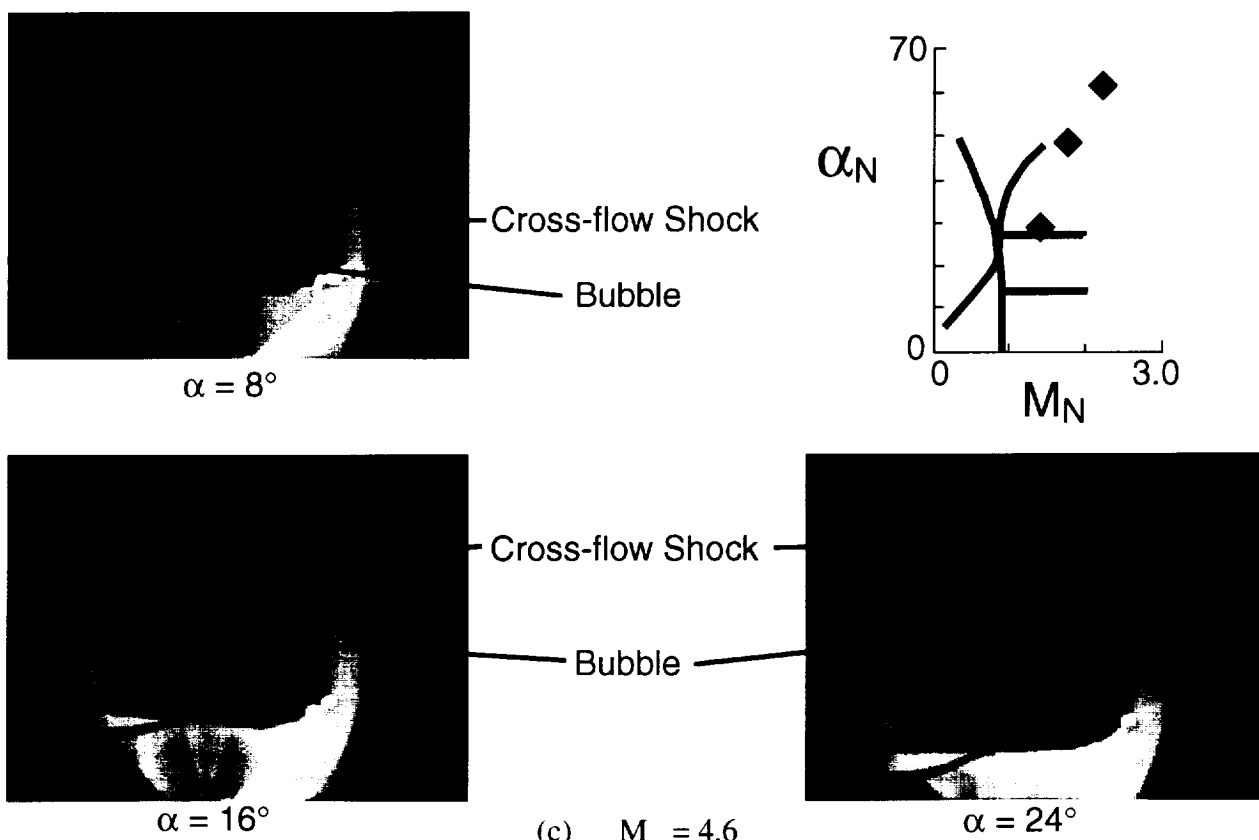


(a)  $M_\infty = 2.4$

Figure 50. Vapor screen photographs of a 75° delta wing model in the NASA LaRC UPWT at  $\alpha = 8^\circ$ ,  $16^\circ$ , and  $24^\circ$  (ref. 112).



(b)  $M_\infty = 3.4$



(c)  $M_\infty = 4.6$

Figure 50. Continued

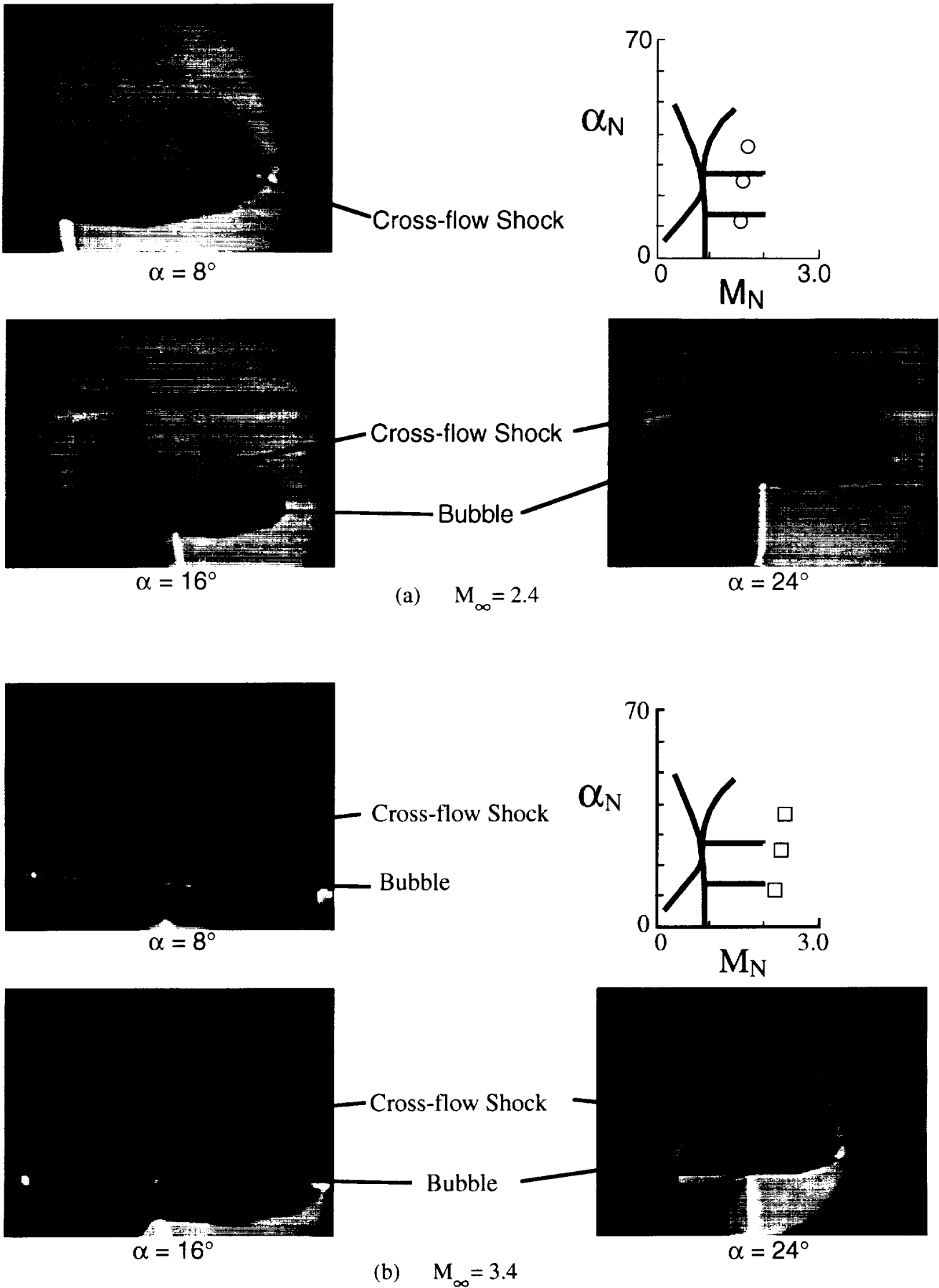


Figure 51. Vapor screen photographs of a 52.5° delta wing model in the NASA LaRC UPWT at  $\alpha = 8^\circ$ ,  $16^\circ$ , and  $24^\circ$  (ref. 112).

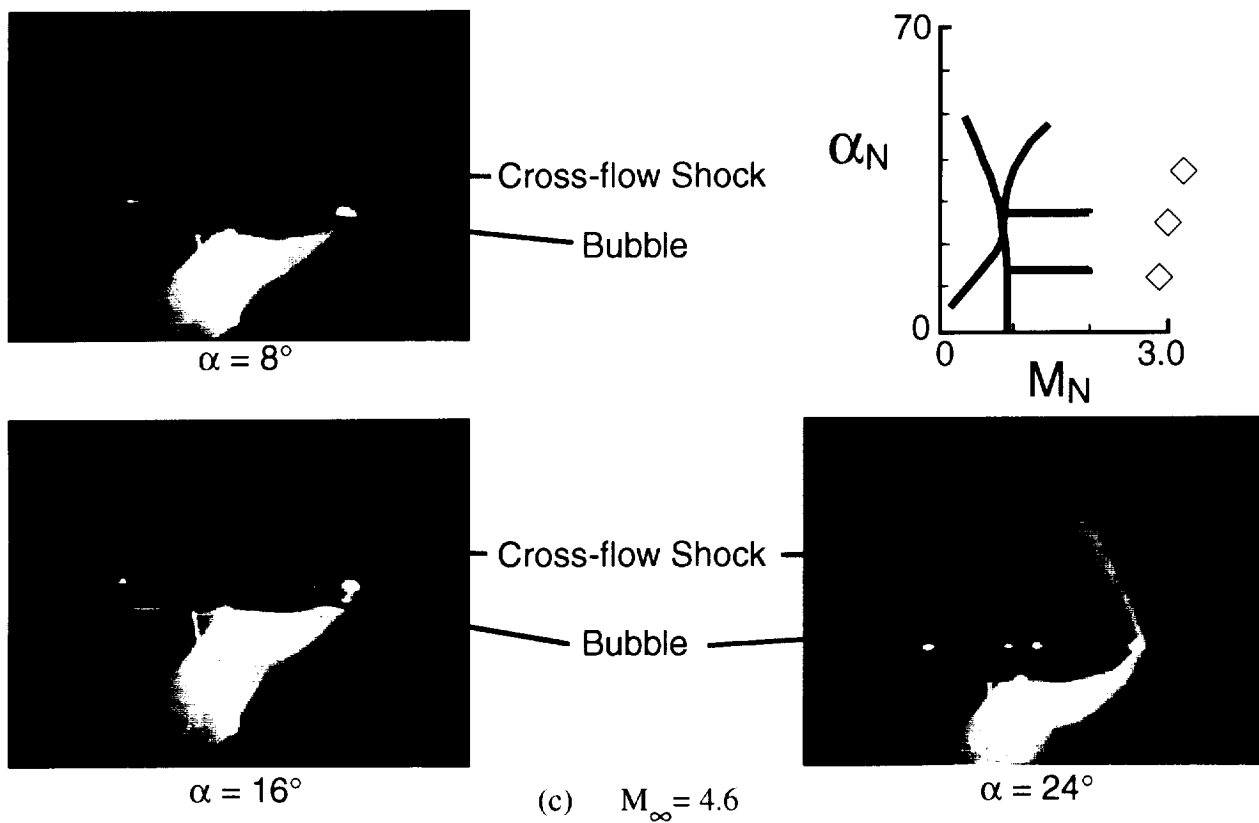


Figure 51. Continued.

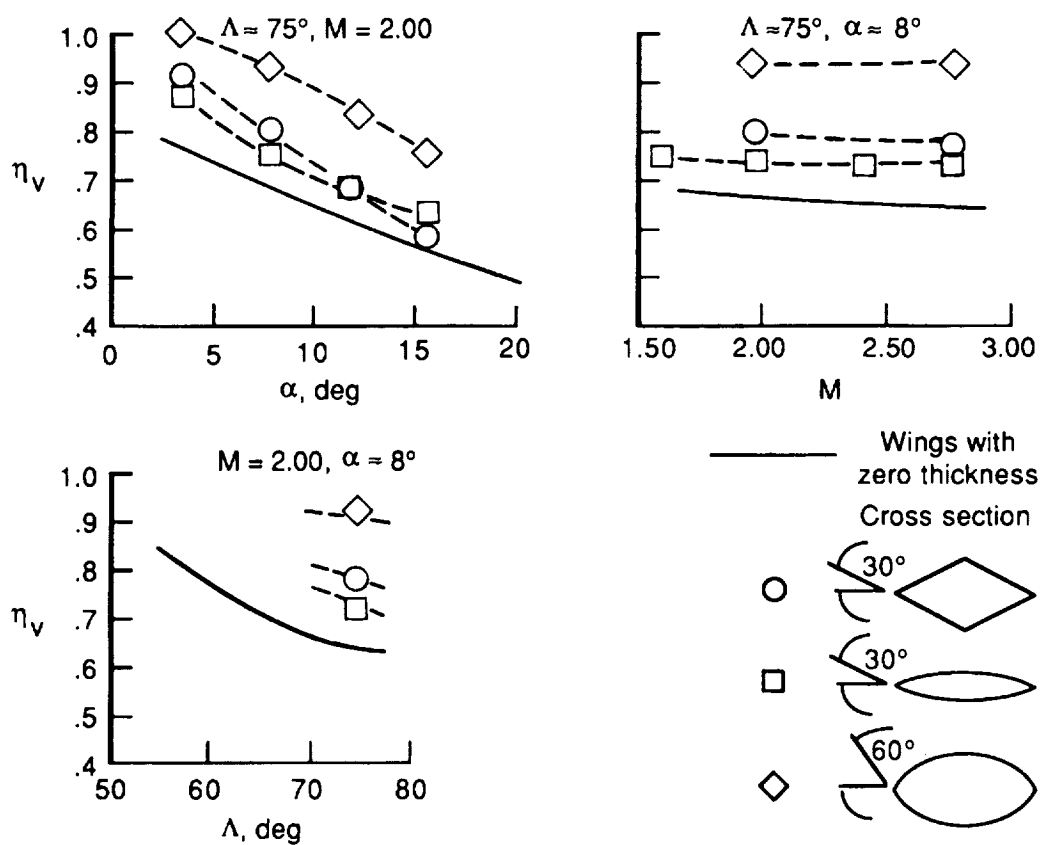


Figure 52. Location of vortex action line for thick delta wings at supersonic speeds (ref. 182).

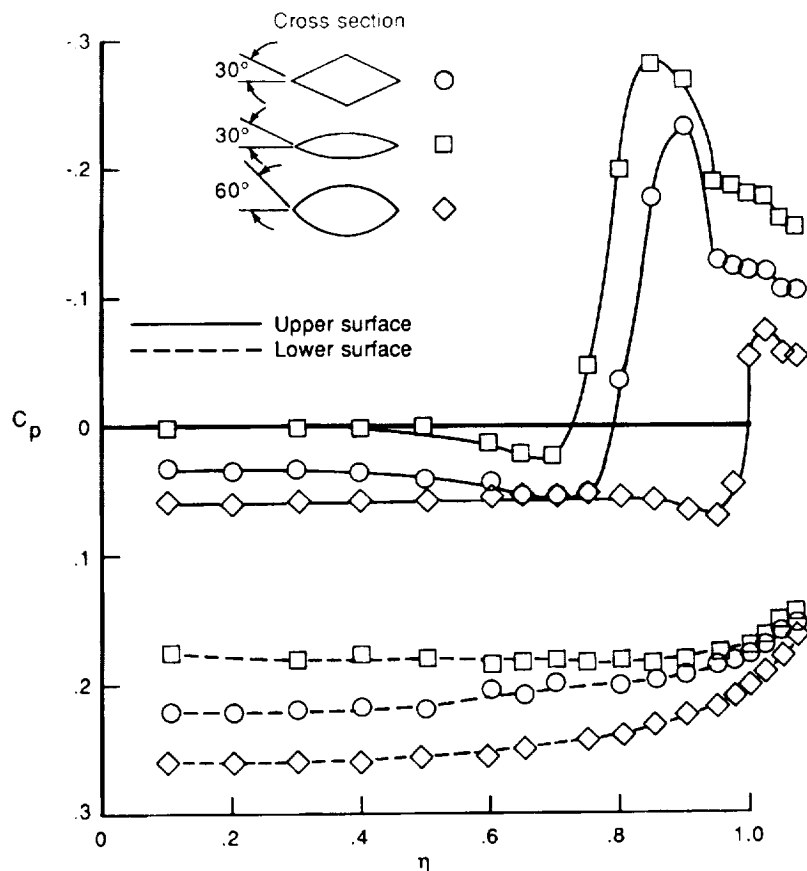


Figure 53. Effect of wing thickness on the spanwise surface pressure distributions of thick delta wings at  $M = 1.30$  and  $\alpha = 8^\circ$  (ref. 182).

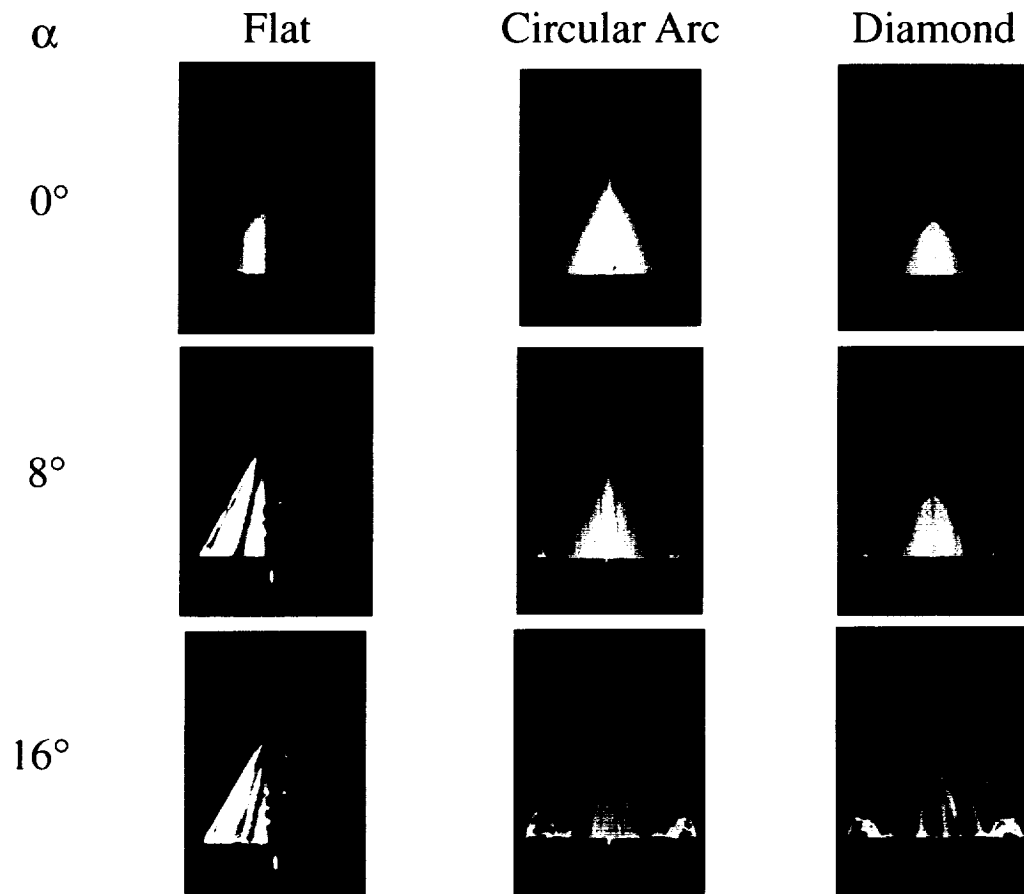


Figure 54. Effect of airfoil shape and angle of attack on the upper surface flow characteristics of thick delta wings at  $M = 1.70$  and  $L = 60^\circ$  (ref. 138).

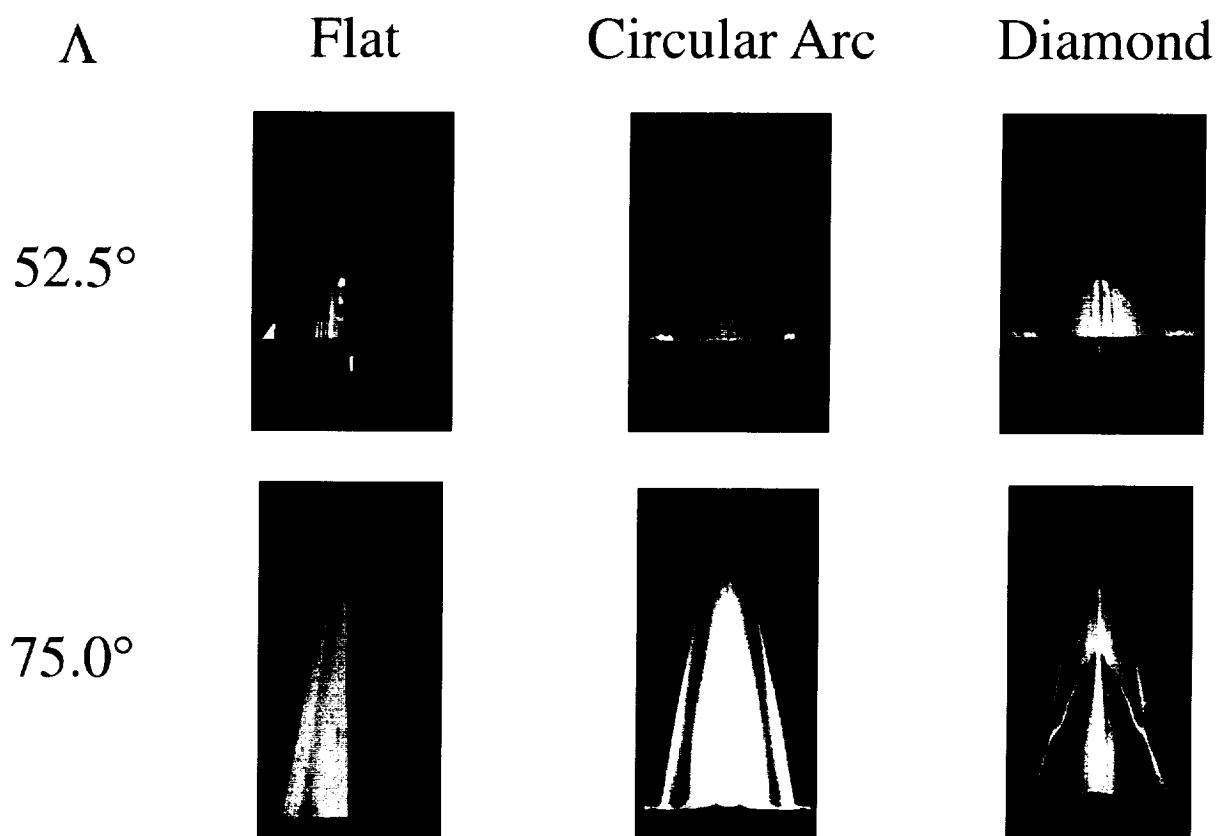
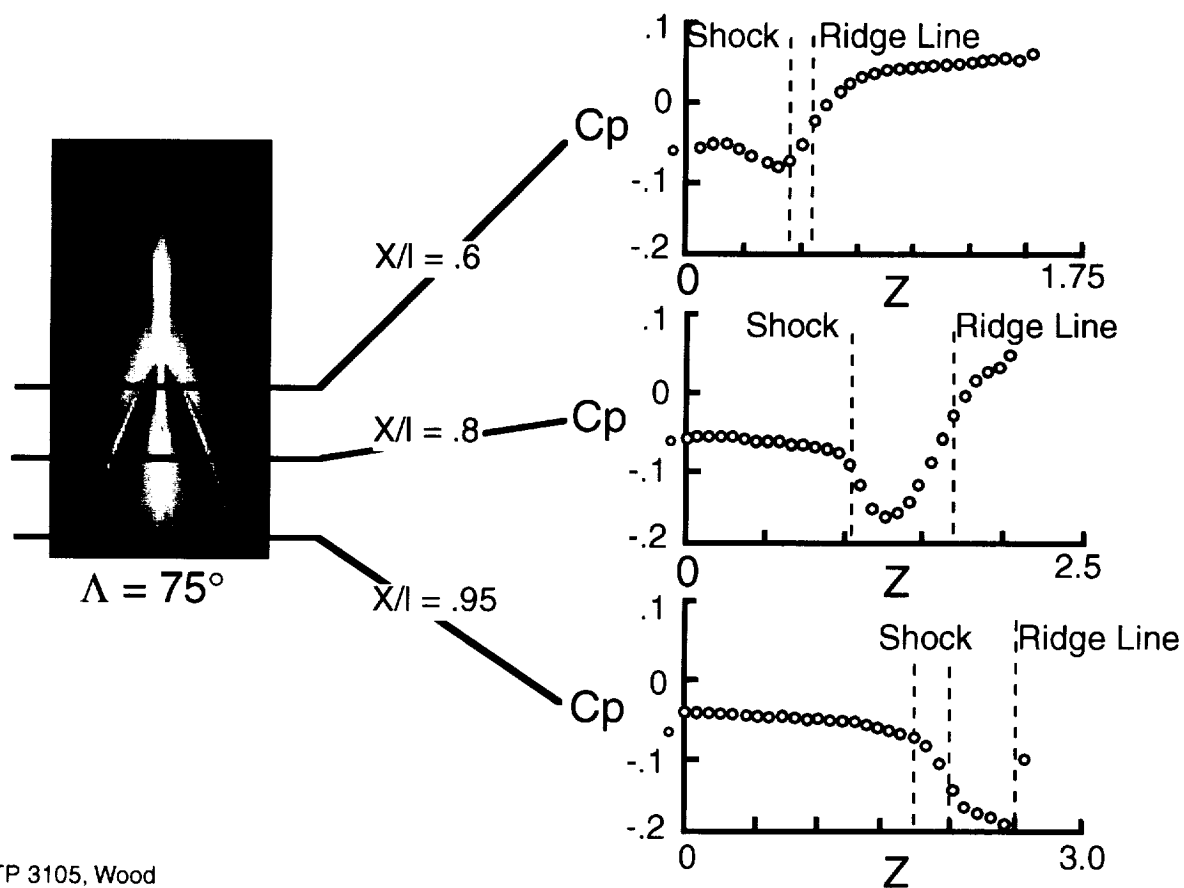


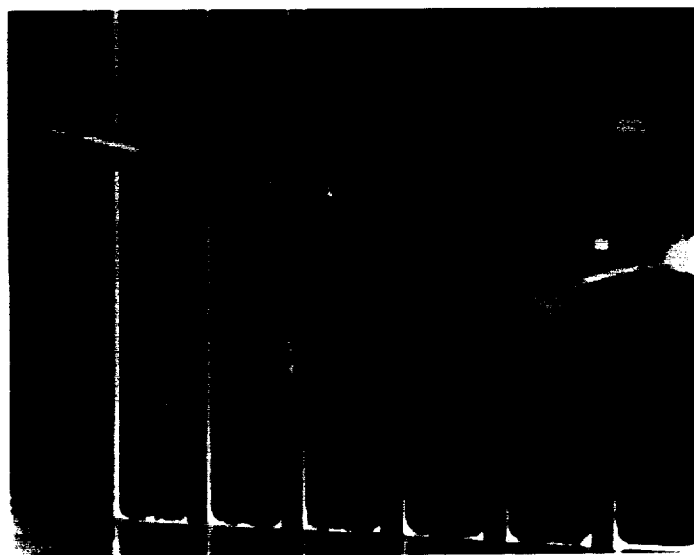
Figure 55. Effect of airfoil shape and leading edge sweep on the upper surface flow characteristics of thick delta wings at  $M = 1.70$  and  $\alpha = 8^\circ$  (ref. 138).



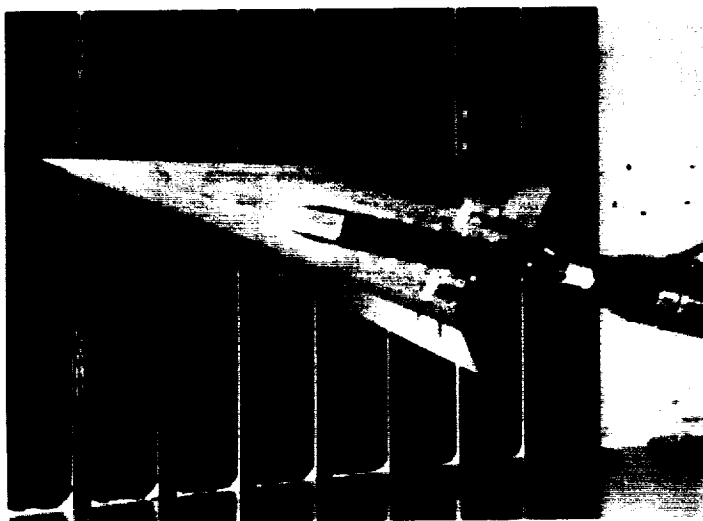
NASA TP 3105, Wood

Figure 56. Effect of airfoil shape on the upper surface flow characteristics of a  $75^\circ$  swept delta wing with diamond airfoil at  $M = 2.00$  and  $\alpha = 0^\circ$  (ref. 138).

$$\begin{aligned}
 S_{\text{Ref}} &= 302.29 \text{ in}^2 \\
 b &= 18.00 \text{ in} \\
 \tau &= 22.39 \text{ in.} \\
 \delta_F &= 0^\circ, 5^\circ, \text{ and } 15^\circ
 \end{aligned}$$



75° delta  
 $\delta_F = 0^\circ$



75° delta (lower surface)  
 $\delta_F = 10^\circ$



75° delta (upper surface)  
 $\delta_F = 10^\circ$

Figure 57. Photograph of a 75° swept delta wing with leading edge flaps installed in the NASA LaRC UPWT (ref. 110).

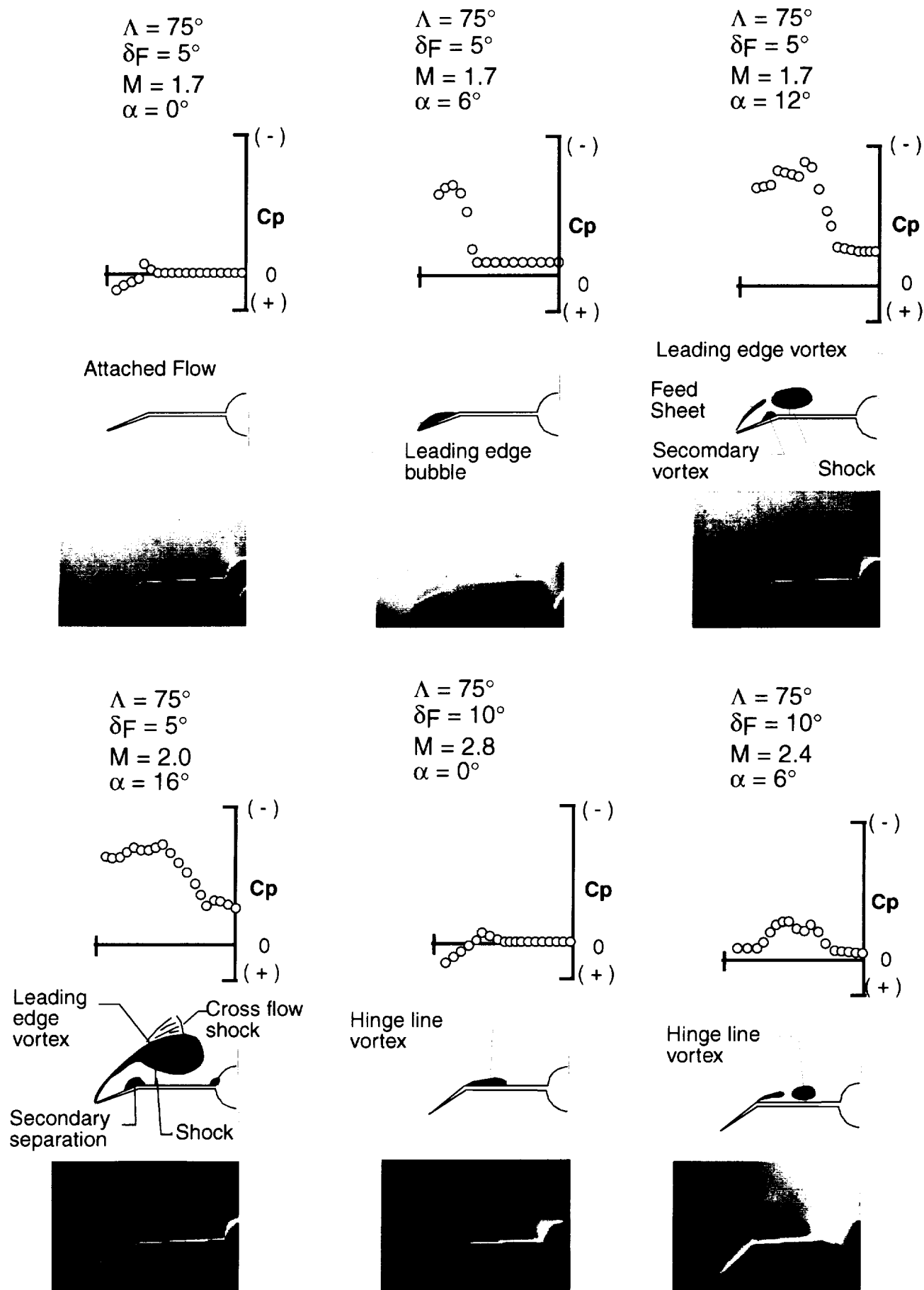


Figure 58. Wing upper surface pressure distributions and vapor screen photographs of the lee-side flow characteristics for single feature flow types observed on a  $75^\circ$  swept delta wing with leading edge flaps (ref. 110).

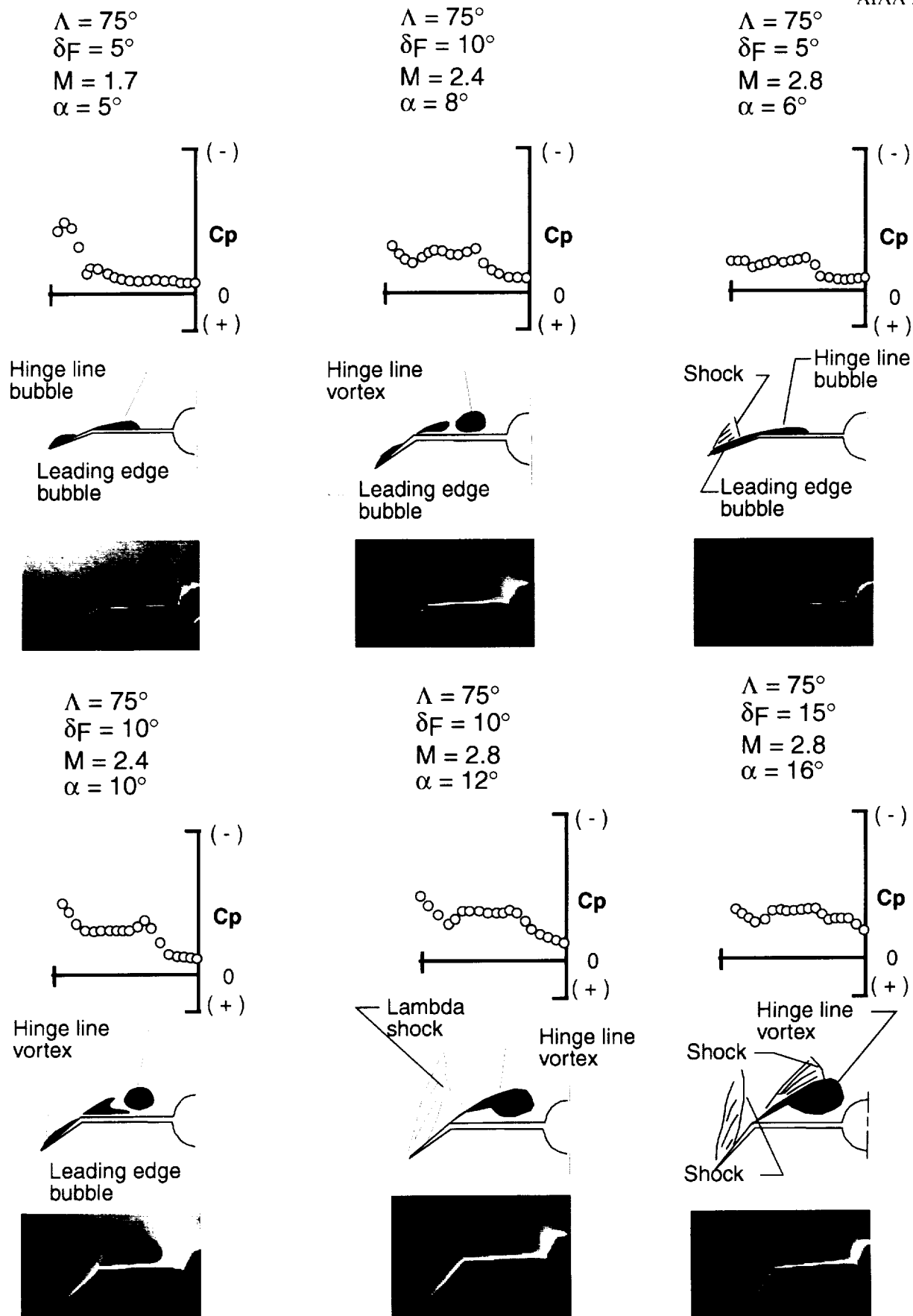


Figure 59. Wing upper surface pressure distributions and vapor screen photographs of the lee-side flow characteristics for double feature flow types observed on a  $75^\circ$  delta wing with leading edge flaps (ref. 110).

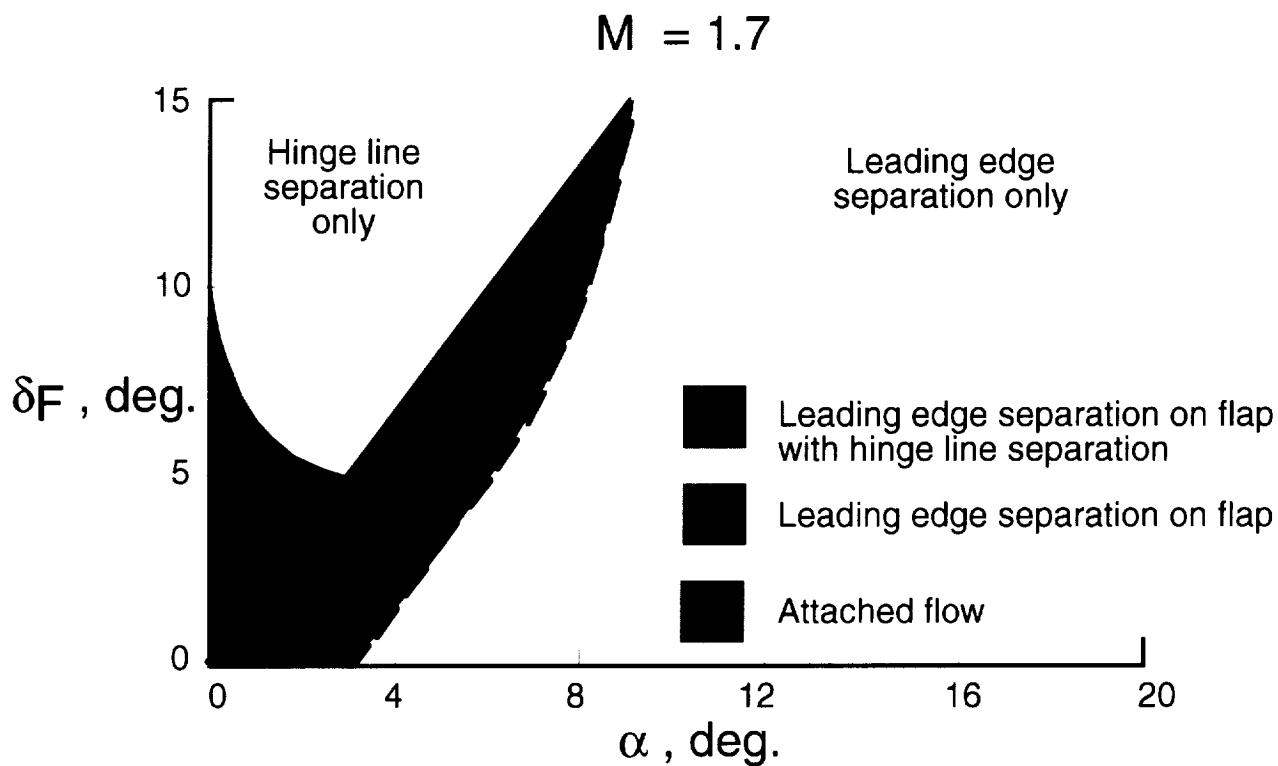


Figure 60. Assessment of vortex flap effectiveness at supersonic speeds (ref. 110).

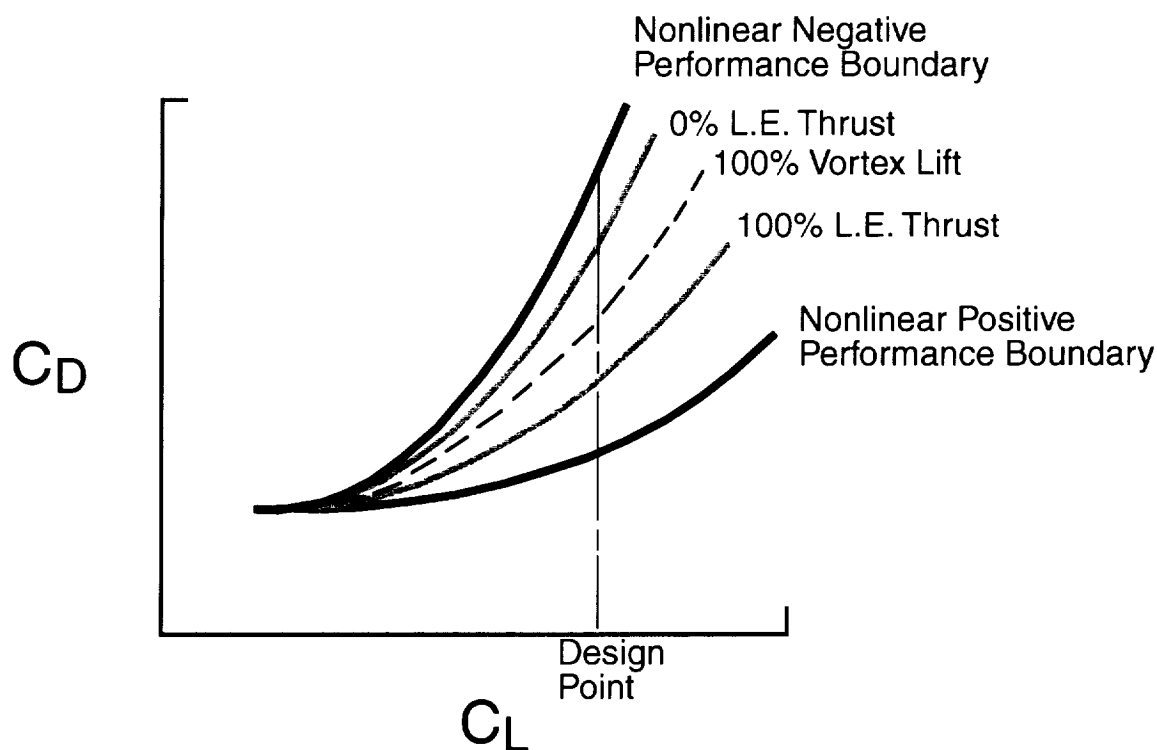


Figure 61. Sketch of linear theory and nonlinear aerodynamic performance boundary (ref. 183).

Region	Geometry	Pressure	Drag
A	Positive Slope	high	high
B	Positive Slope	low	low
C	Negative Slope	low	high
D	Negative Slope	high	low

 Expansion Region  
 Compression Region  
 Airfoil Maximum Thickness Line  
 Cross-flow Recompression Line

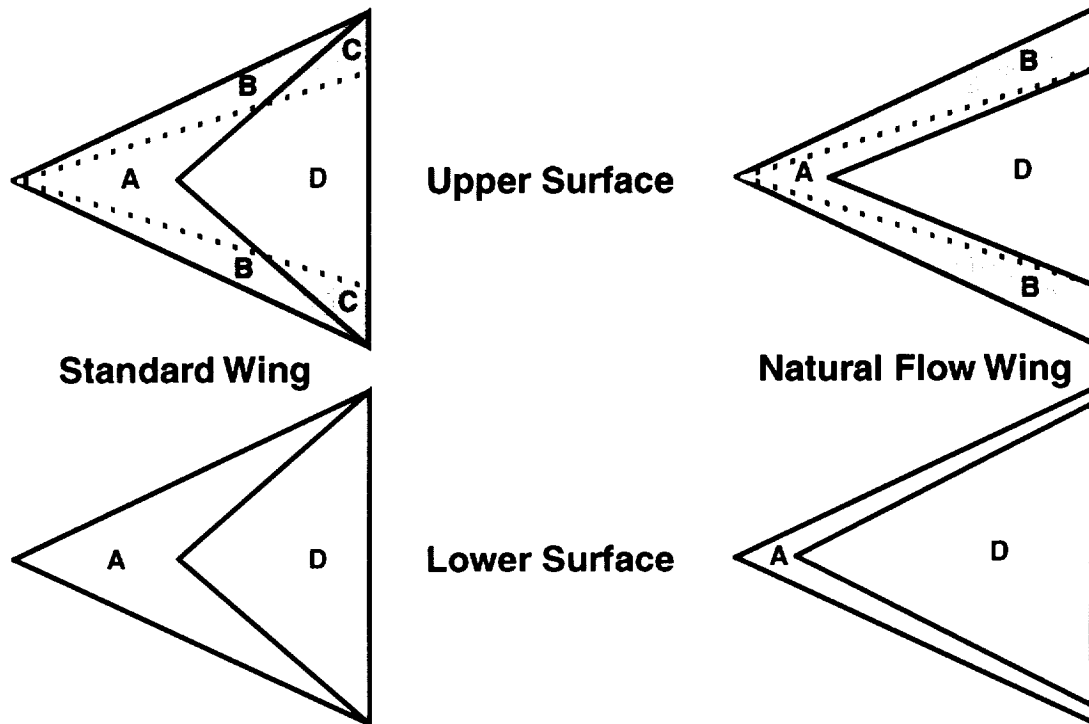


Figure 62. Schematic of the natural flow wing design approach (ref. 183).

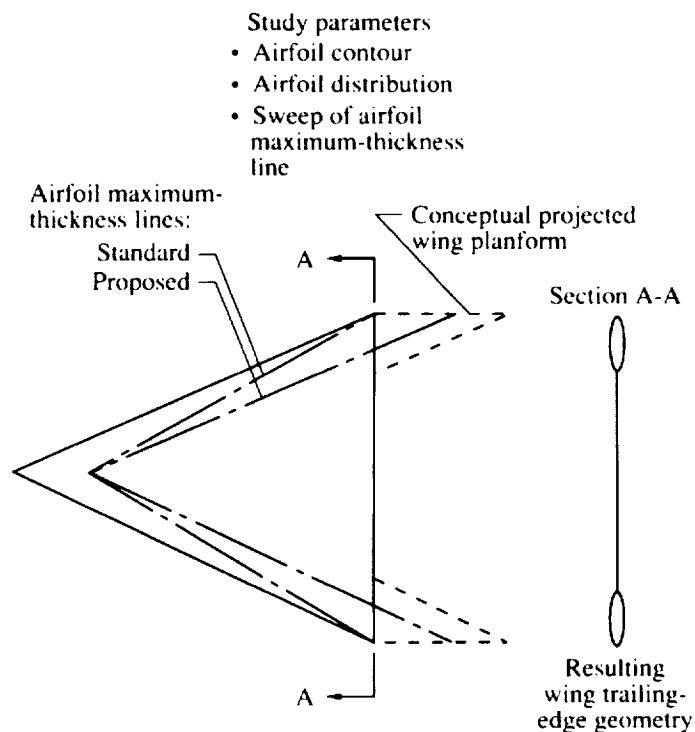
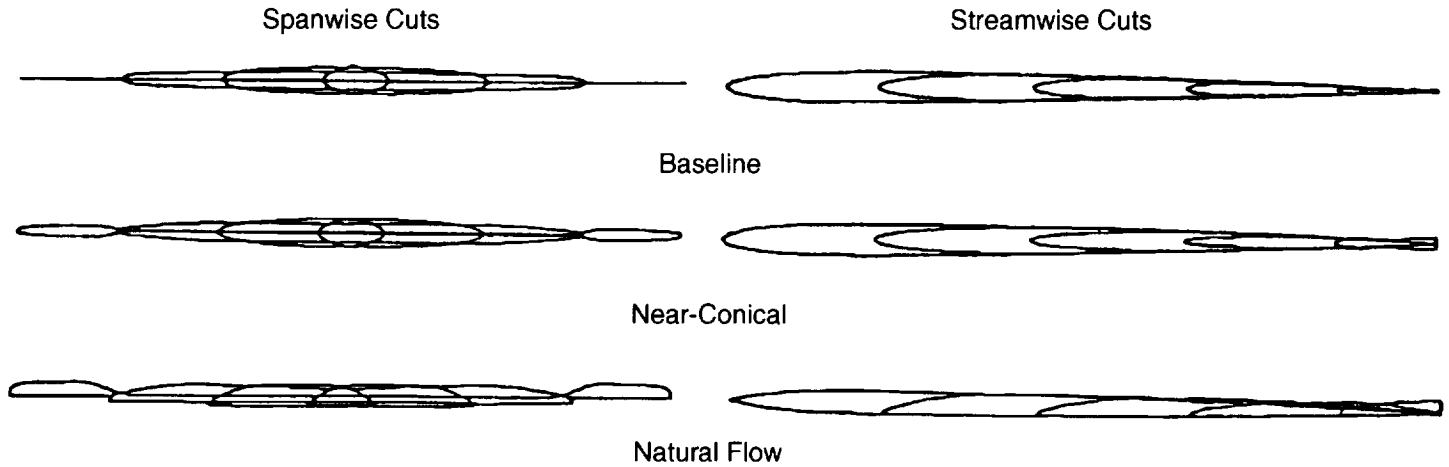
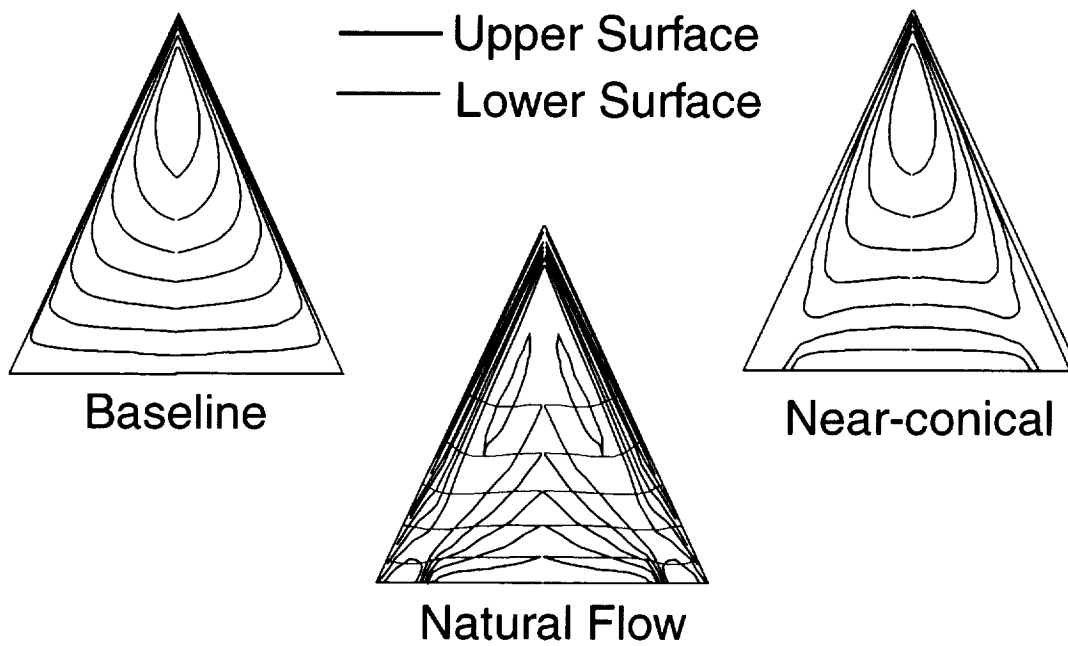


Figure 63. Near-conical maximum thickness location and resulting geometry for the natural flow design approach (ref. 183).



(a) Spanwise and Streamwise Cuts



(b) Elevation Cuts

Figure 64. Geometric details of baseline, near-conical, and natural flow  $65^\circ$  delta wing models (ref. 183).

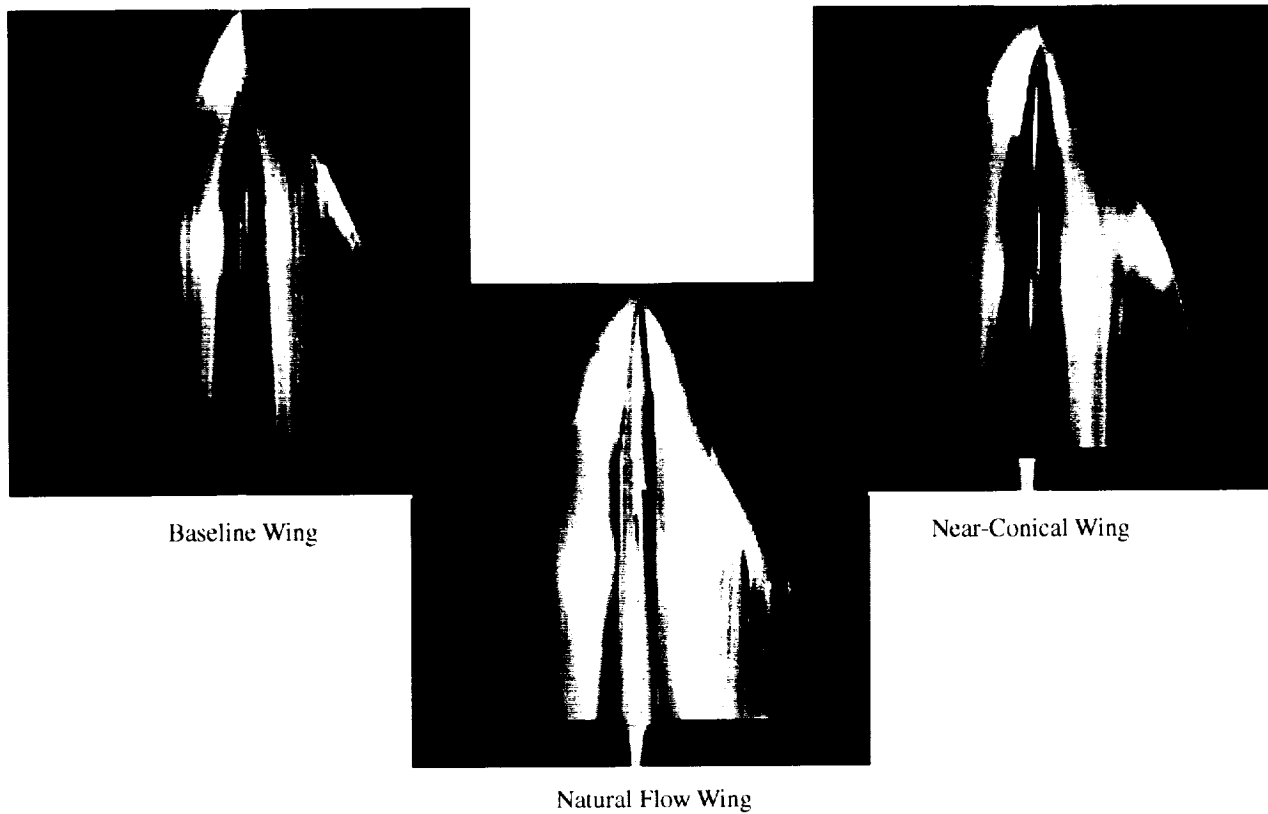


Figure 65. Oil flow photograph of the lee-side flow characteristics for the baseline, near-conical, and natural flow 65° delta wing models at  $M = 1.62$  and  $\alpha = 8^\circ$  (ref. 183).

Computation	Experiment	Model
—	○	Baseline Wing
- - -	□	Near-Conical Wing
- · - ·	△	Natural Flow Wing

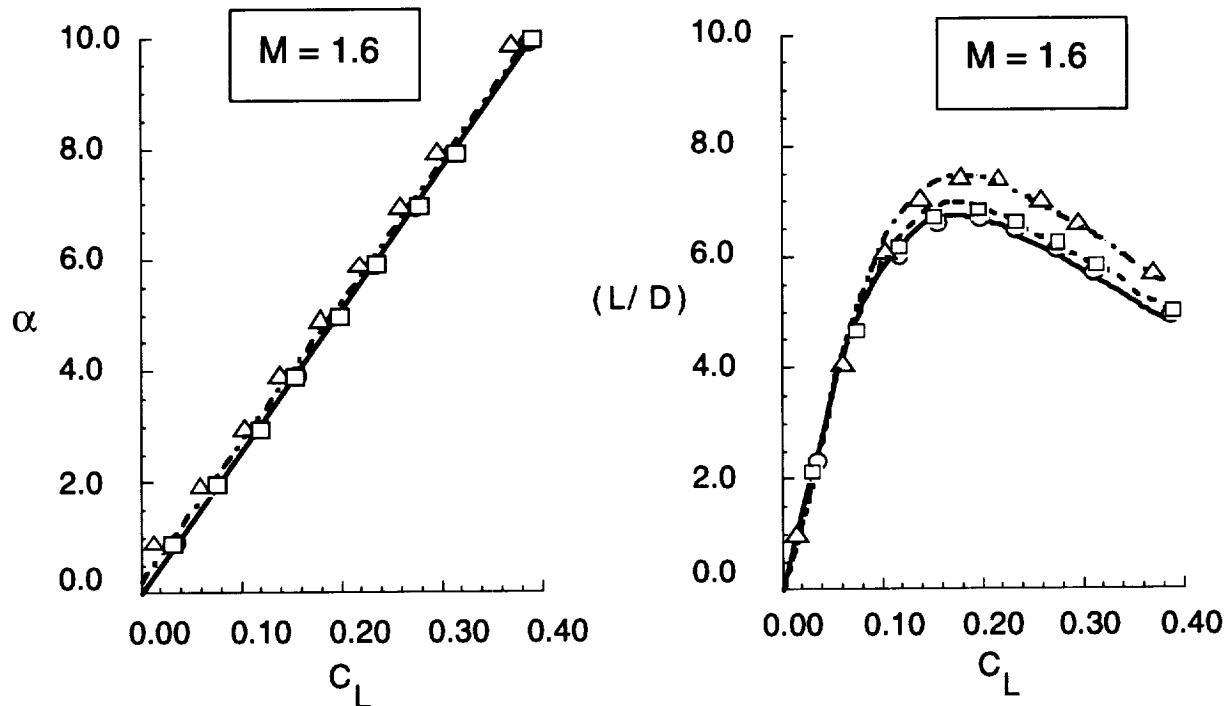


Figure 66. Plot of the lift and lift-to-drag ratio characteristics for the baseline, near-conical, and natural flow 65° delta wing models at  $M = 1.6$  (ref. 183).



